MAGNETOPLASMA INTERACTIONS WITH ICY BODIES

A Dissertation
Presented to
The Academic Faculty

By

John P. M. Hale

In Partial Fulfillment
of the Requirements for the Degree
Doctor of Philosophy in the
School of Earth and Atmospheric Sciences

Georgia Institute of Technology

December 2017

MAGNETOPLASMA INTERACTIONS WITH ICY BODIES

Approved by:

Dr. Carol Paty, Advisor
School of Earth and Atmospheric Sciences
Georgia Institute of Technology

Dr. James Wray
School of Earth and Atmospheric Sciences
Georgia Institute of Technology

Dr. Josef Dufek
School of Earth and Atmospheric Sciences
Georgia Institute of Technology

Dr. Morris Cohen
School of Electrical and Computer Engineering
Georgia Institute of Technology

Dr. Jérémy Riousset
Department of Physics and Space Sciences
Florida Institute of Technology

Date Approved: July 27, 2017

Pusilla res mundus est, nisi in illo quod quaerat omnis mundus habeat.

Our universe is a sorry little affair unless it has in it something for every age to investigate.

Seneca the Younger

To my mother, who would support me beyond the ends of the Earth,

and to my friends, who keep me grounded.

ACKNOWLEDGEMENTS

While there are many people that have played a part in the successful completion of my doctoral research, I would first like to thank Professor Carol Paty, my advisor. Anyone whom I have ever talked to about her knows that I could not have asked for a better doctoral advisor. Not only has she been an excellent sounding board and valuable source of information related to my research, but she has also been unfailingly supportive of my efforts to broaden my knowledge of other areas such as public policy. Most importantly however, she saw potential in me and took the time to foster it. I would not be here without her.

I would also like to thank the other members of my defense committee: Professors James Wray, Jérémy Riousset, Joe Dufek, and Morris Cohen. In addition to cheerfully serving on on my committee, James taught me remote sensing and supported my exploration of creative ways to use data from the Mars Reconnaissance Orbiter. Jérémy mentored me as an undergraduate researcher while he was working with Carol, happily providing me with a thorough grounding in large scale simulation development. Joe took me to volcanic Aegean islands, so that I could get some experience with honest field work. Morris provided me with insight into the world of science policy. I have been fortunate to have such a helpful and supportive committee.

Current and former members of Carol's research group have been helpful in so many different ways that it would be difficult to list, so I will simply say thank you Ashok Rajendar, Xin Cao, Alexia Payan, Reka Winslow, and Ayanna Jones. Each of you has been a great help, whether by providing a fresh set of eyes on a challenge in modifying the model or by reading over my writing, and I am grateful.

There are several other members of faculty that I would like to express my gratitude to. Sven Simon has provided manifold recommendations and given his perspective on how to properly engage in scientific research. Britney Schmidt has helped me in many different areas, but I have perhaps benefited most significantly from her knowledge of science policy. James Sowell convinced me to move into physics from engineering through his brilliant courses and valuable advice. Finally, I would like to thank Mariel Borowitz and Eliza Markley, who both are skilled teachers of policy, and who both went out of their way to support my interest in policy outside of their courses.

The other graduate students in the department have unquestionably been supportive as well. Gabe Eggers and Heather Chilton were there many times to talk over an issue in planetary science and Sven's students Zachary Meeks and Lucas Liuzzo have been accessible sources of perspective on different ways to accomplish research tasks similar to my own.

Erika Harnett and Peter Delamere both generously gave me their time to discuss details of their work on modeling the Pluto system. Peter Kollmann provided me with insight into the PEPSSI instrument on the New Horizons mission to Pluto and Steve Joy made NASA's Planetary Data System seem accessible. I would also like to thank any other members of the planetary science community who have helped me in some way – of which there are many.

I will always be grateful to the Georgia Space Grant Consortium for awarding me a fellowship; anyone in academia knows that stable funding makes everything easier.

I would like to thank all of my friends who have been an unbeatable support network while I have been working on my doctorate. And, finally, I want to thank my family. Blanche has been a great help in the last few years, always ready to talk if I needed to. I

know that Andrew is there when I need him, and I have done my best to reciprocate. Last of all, I want to thank my mother. She would do anything for me that she could and she believes that I can accomplish whatever I choose to.

TABLE OF CONTENTS

LIST OF TABLES

LIST OF FIGURES

LIST OF SYMBOLS

$\vec{B}$	Magnetic Field Vector
$\vec{B}_{\mathrm{IMF}}$	Interplanetary Magnetic Field Vector
B_{surf}	Magnetic Field Strength at Surface of Planet
Da	Dalton (Unified Atomic Mass Unit)
e	Negative Elementary Charge
$\vec{E}$	Electric Field Vector
G	Universal Gravitational Constant
$\vec{J}$	Current Density
L_α	Loss Rate for Species α
Mb	Megabarn (10^{-18}cm^2)
$\mathrm{M_C}$	Mass of Charon
$\mathrm{M_E}$	Mass of Europa
M_o	Mass of Body
$\mathrm{M_P}$	Mass of Pluto
m_α	Mass of Species α
n_{e}	Electron Number Density
n_n	Neutral Number Density
n_α	Number Density of Species α

P_{e}	Electron Pressure
P_{α}	Plasma Pressure of Species α
q	Positive Elementary Charge
q_{α}	Charge of Species α
R_o	Radius of Body
$\mathrm{R_C}$	Radius of Charon
R_{CF}	Chapman-Ferraro Distance
$\mathrm{R_E}$	Radius of Europa
$\mathrm{R_J}$	Radius of Jupiter
$\mathrm{R_P}$	Radius of Pluto
r	Distance from Center of Body
$\hat{r}$	Unit Vector Towards Center of Body
$\mathrm{r_E}$	Orbital Distance of Europa
r_{g}	Gyroradius
S_{α}	Source Rate for Species α
T_{e}	Electron Temperature
v	Speed
$\vec{v}$	Velocity
$\vec{v}_{\mathrm{corot}}$	Corotational Velocity
$\vec{v}_{\mathrm{e}}$	Electron Velocity
$\vec{v}_n$	Neutral Velocity
$\vec{v}_{\mathrm{SW}}$	Velocity of Solar Wind

$\vec{v}_\alpha$	Velocity of Species α
α_{inc}	Incident Plasma Species
β	Plasma Beta
γ	Ratio of Specific Heats
η	Resistivity
θ	Azimuth
μ_0	Permeability of Free Space
ρ_α	Mass Density of Species α
σ_{ce}	Ion-Neutral Charge Exchange Cross Section
σ_{e}	Electron Impact Ionization Cross Section
σ_{ph}	Photoionization Cross Section
Φ_{ph}	Photon Flux
ϕ	Latitude

LIST OF ABBREVIATIONS

AU	Astronomical Unit
BATSRUS	Block-Adaptive-Tree-Solarwind-Roe-Upwind-Scheme
EC	Europa Clipper Spacecraft
EphiO	Europa Centered Coordinate System
EST	Elapsed Simulation Time
EUVAC	Extreme Ultraviolet Flux Model for Aeronomic Calculations
HST	Hubble Space Telescope
ICEMAG	Interior Characterization of Europa Using Magnetometry
IMF	Interplanetary Magnetic Field
JMP	Jovian Magnetospheric Plasma
KBO	Kuiper Belt Object
KSI	Kilometer-Scale Impactor
MFL	Magnetic Field Latitude
MHD	Magnetohydrodynamics
NH	New Horizons Spacecraft
PEPSSI	Pluto Energetic Particle Spectrometer Science Investigation
PIMS	Plasma Instrument for Magnetic Sounding
SVHM	Scalar/Vector Helium Magnetometer

SW	Solar Wind
SWAP	Solar Wind Around Pluto Instrument
TFGM	Triaxial Fluxgate Magnetometer
TOF	Time of Flight
UT	Universal Time

SUMMARY

Both the interaction between the Pluto-Charon system and the solar wind and Europa and the Jovian magnetosphere vary with system configuration. We use a global, three-dimensional, multifluid magnetohydrodynamic model (the Icy Bodies Model) to investigate Pluto's interaction with the solar wind, what role Pluto's companion Charon plays in this interaction, and mass loss from the system. We also use the Icy Bodies Model to explore how Europa's interaction with Jupiter's magnetosphere changes depending on its location within the magnetosphere and what contribution Europa's ionosphere makes to this interaction. In order to perform these simulations, we have modified the model to accommodate an arbitrary number of bodies within the system, to include dynamic, volumetric plasma source and loss terms based on realistic neutral atmospheric profiles, and to incorporate induced planetary magnetic dipoles. The three plasma sources implemented with the model are electron impact ionization, photoionization, and ion-neutral charge exchange. This last mechanism also acts as a loss term within the system because it involves ions recombining by stripping electrons from the neutral population. Simulations of the Pluto-Charon system have included three ion species (solar wind protons, Pluto-sourced heavy ions, and Charon-sourced heavy ions), while those of Europa have included two (Jovian magnetospheric plasma and Europan ionospheric singly ionized molecular oxygen). In addition to their utility in investigating system behavior, our simulations of the Pluto-Charon system provide context for flyby data returned by the New Horizons mission. Results are validated against previous modeling efforts, as well as this New Horizons data. Results of our exploratory Europa work are compared with other modeling studies.

CHAPTER 1

INTRODUCTION

1.1 Primer on Magnetospheres

The behavior of magnetized plasma – or magnetoplasma – can be difficult to understand, as it combines compressible fluid dynamics with electromagnetism. Nevertheless, it is a topic that is well worth studying. This is because magnetoplasmas play a crucial role in many physical systems, from the formation of solar systems, to the operation of planned fusion reactors, to the conditions present within the upper atmosphere and near space environment of our planet. This last area is closely related to the investigations described within this document and can serve as an introduction to certain aspects of magnetoplasmas that will prove useful for understanding some subjects discussed within this document.

First, the Lorentz force (described by the equation: $\vec{F} = q(\vec{E} + \vec{v} \times \vec{B})$ in which $\vec{F}$ is the force, q is the charge of the particle, $\vec{E}$ is the electric field vector, $\vec{v}$ is the particle velocity, and $\vec{B}$ is the magnetic field vector) diverts particles with opposite charges, such as protons and electrons, in opposite directions when they encounter a magnetic field. This means that when particles in the solar wind, mostly protons and electrons, reach Earth's magnetic field, they are forced to divert in different directions as shown in Figure 1.1. As electrical currents are the result of positive and negative charge carriers moving in separate directions, the Lorentz force acting on solar wind particles entering the Earth's (or any other magnetized body's) magnetic field creates an electrical current known as the Chapman-Ferraro current. This current serve to divide the solar wind, which carries the Interplanetary Mag-

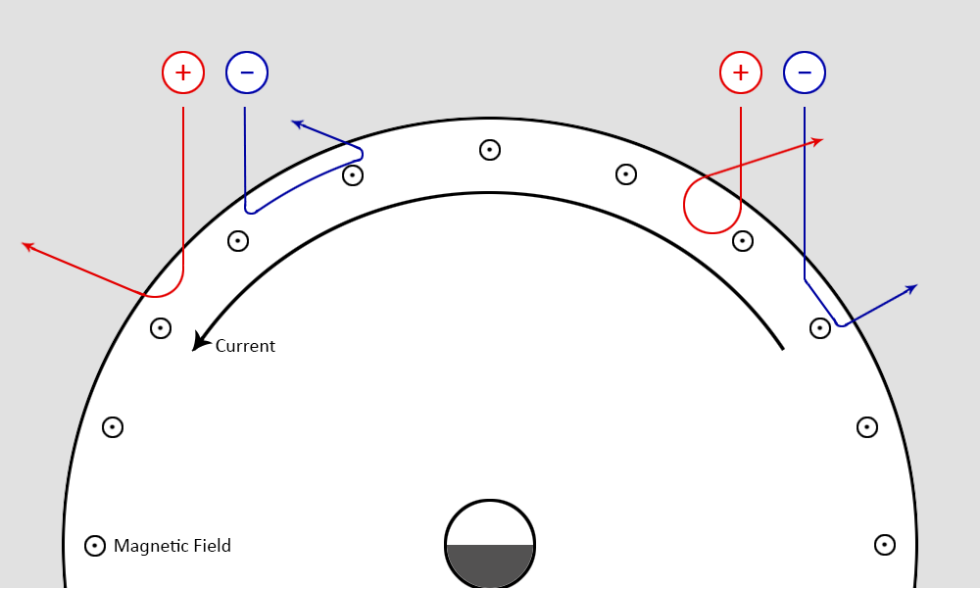

Figure 1.1: Generation of a Chapman-Ferraro current along the magnetopause due to differential motion of incident ions and electrons caused by the Lorentz force.

netic Field (IMF), from the region around the Earth known as its magnetosphere. Within the magnetosphere of a planet, plasma flows and magnetic fields are largely isolated from the conditions outside.

$$\mathrm{R_{CF}} = \mathrm{R}_o \left(\frac{B_{\mathrm{surf}}^2}{\mu_0 \rho v_{\mathrm{SW}}} \right)^{1/6} \tag{1.1}$$

The boundary formed by the Chapman-Ferraro current is known as the magnetopause, and can be seen in Figure 1.2. The distance at which this boundary forms is where the combined dynamic and magnetic pressures of the solar wind balance with the magnetic pressure of the planet's magnetic field and is given by Equation 1.1 (Blanc et al., 2005), where $\mathrm{R_{CF}}$ is the standoff distance, R_o is the radius of the body, B_{surf} is the magnetic field strength at the body's surface, μ_0 is the permeability of free space, ρ is the plasma density, and v_{SW} is the speed of the upstream plasma. Also visible in this figure are other features that

are typical of magnetospheres. A particularly important feature for the purposes of this document is the bow shock, which forms outside of the magnetopause. This structure is created through a similar process to how a sonic boom is created by an aircraft moving through the atmosphere at supersonic speeds. When an object is moving supersonically, it is traveling faster than information can be transmitted through the atmosphere (the speed of sound). Similarly, the bow shock is a result of the fact that plasma within the solar wind travels faster than magnetohydrodynamic information can propagate interplanetary plasma through the system. While the velocity of sound within the atmosphere is known as the Mach velocity, the velocity at which magnetohydrodynamic information can move through a plasma is known as the Alfvén velocity. The Alfvén velocity within the solar wind near the Earth is typically $\sim$49 km/s, while the velocity of slow solar wind is $\sim$400 km/s, so the solar wind moves highly super-Alfvénically.

Once the solar wind plasma reaches the bow shock, it is slowed down rapidly until it is moving at less than the local Alfvén velocity, and in the process increases in temperature and density. Because the IMF is carried along with the solar wind plasma (due to what is known as the "frozen-in" condition), the magnetic flux density also increases, as the density of the plasma increases. This region of relatively hot and dense plasma, coupled with increased magnetic field strength, is known as the magnetosheath. As can be seen in Figure 1.2, the magnetosheath extends until the magnetopause is reached. The magnetotail is also visible in the figure. This structure is a result of the solar wind outside of the magnetosphere distorting the planet's dipolar magnetic field on the side of the planet facing away from the solar wind, forcing it to elongate and compress. This process results in oppositely directed magnetic field lines downstream of the planet being forced close together. Due

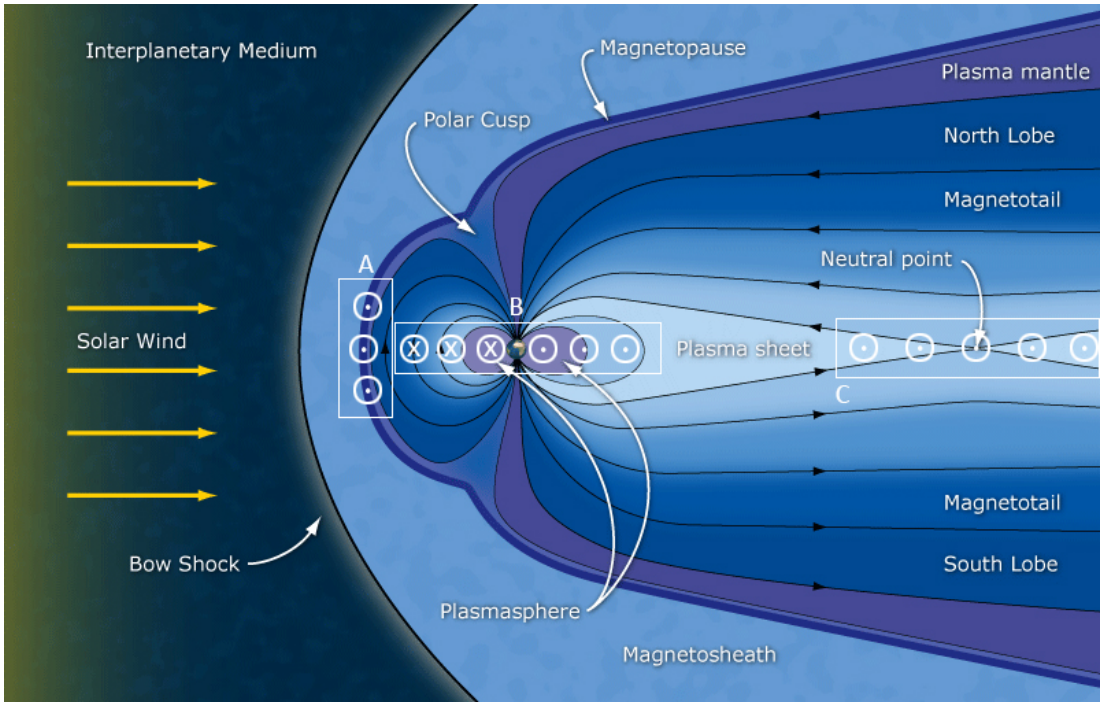

Figure 1.2: Diagram of Earth's magnetosphere with regions and currents labeled. A represents the Chapman-Ferraro current, B represents the ring current, and C represents the cross-tail current. Modified from original image by NASA.

to Ampère's Law ($\nabla \times \vec{B} = \mu_0 \vec{J}$) this sudden change in magnetic field direction across a small distance results in the generation of a current called the cross-tail current. Because is current closes around the outside of the magnetotail, it serves to stabilize the structure. At this point where oppositely pointing magnetic field lines are in close contact, the frozen-in condition can momentarily breakdown, due to the trace resistivity within a plasma being great enough that the level of current required by Ampère's Law cannot be maintained. When this happens, magnetic field lines rearrange, and move away from the reconnection location, which is the neutral point labeled in the figure. Reconnection can also occur at the subsolar boundary of a magnetosphere, often when the IMF is aligned anti-parallel to the planet's magnetic dipole and there is high plasma β (the ratio of plasma pressure and magnetic pressure). This process carries plasma along with the rearranging magnetic field

lines, allowing for material from outside of the magnetosphere enter the magnetosphere. Closer to the planet, within the magnetosphere, the dipolar field structure remains largely intact and rotates with the planet, carrying plasma along with it. This results in plasma moving around the Earth at super-Keplerian speeds (faster than the speed of orbital motion around the parent body would be at a given distance) and is known as corotation. This corotating population is also experiencing differential motion between the positively and negatively charged particles. This is due to the fact that the magnetic field lines of a dipolar field have significant curvature close to the planet and also because the strength of the magnetic field varies significantly with distance from the planet. The result of this ∇B drift effect is the creation the ring current, which goes around the planet (from east to west in the case of the Earth). While the cross-tail current reinforces the magnetotail, the ring current creates a magnetic field which decreases the strength of the planet's dipolar field in its vicinity. In addition, plasma that is corotating around the planet is also engaged in bounce motion, in which it travels up and down magnetic field lines. If the particles are too energetic, they can penetrate into the planet's atmosphere and collide with neutral particles, generating an aurora. This is why aurorae are more pronounced when the Sun is unusually active, more high energy particles are being introduced to the magnetosphere through reconnection and then colliding with the atmosphere as a result of bounce motion.

1.2 Induced Magnetospheres

In contrast to planetary bodies that possess their own magnetic field, which is known as an intrinsic magnetic field, some bodies possess what is called an induced magnetosphere. In an induced magnetosphere, the obstacle to the solar wind is created by the atmosphere and

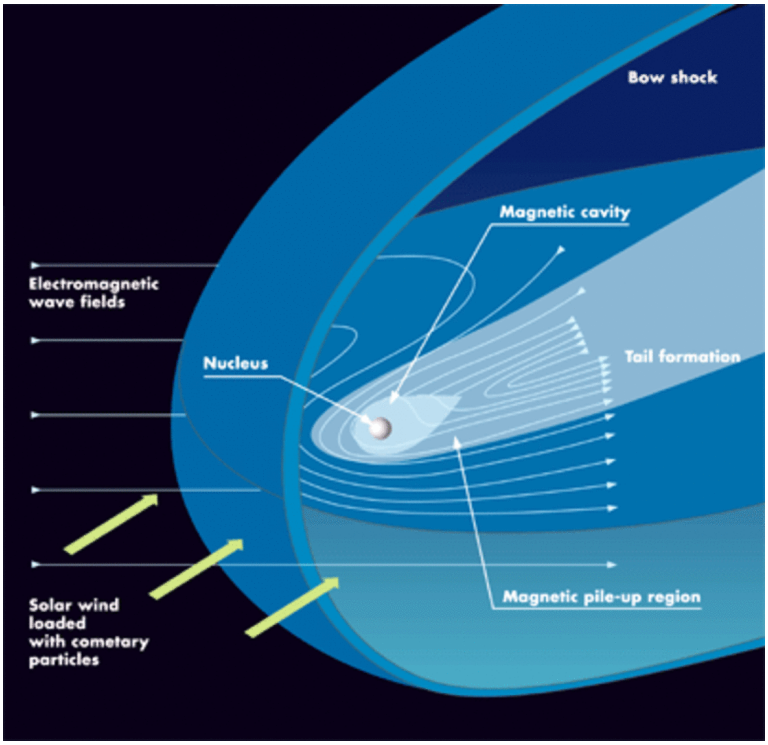

Figure 1.3: Diagram of interaction between solar wind and a comet. Regions and field configurations are shown. Modified from original image by ESA.

ionosphere of the body, or by the conducting core of the object.

In the case of an ionosphere, which is a highly conductive object, the passage of magnetic flux carried with the solar wind is effectively obstructed, causing magnetic flux tubes to drape around the obstacle, rather than to pass directly through it. This results in the formation of a bow shock, much like that which is generated around a body with an intrinsic magnetic field. Within the ionosphere of the object, a diamagnetic cavity is formed in which magnetic field strength is very low compared to in the pile up region and the upstream plasma. Figure 1.3 demonstrates an induced magnetosphere in the case of a comet. An example of what is believed to be an induced magnetosphere is the region that surrounds the dwarf planet Pluto. If the object is without an atmosphere and ionosphere, the incident plasma simply impacts with the object's surface, creating a small wake behind the object.

Pluto's companion Charon appears to be an example of an object that has this type of interaction. If the magnetic field conditions upstream of the object are varying, an induced magnetic dipole can be formed within the object that is proportional in strength to the variations in the upstream magnetic field strength. In this case, the induced magnetosphere can be quite similar to an intrinsic magnetosphere. Europa is a body which does not have an intrinsic magnetic field, but does have an induced dipolar field resulting from the periodic variations that it experiences due to the axial tilt of the Jovian magnetic dipole, as well as the the eccentricity of Europa's orbit around Jupiter.

1.3 Organization of the Dissertation

1.3.1 Main Topics

This dissertation reports on investigations of interactions between magnetoplasma and several small icy bodies ranging in size from 1200 to 3100 km in diameter performed using a significantly modified version of the multifluid magnetohydrodynamics model originally developed by R. M. Winglee (1998). Notable enhancements to the model include the ability to simulate systems containing an arbitrary number of planetary bodies as well as the inclusion of neutral particle interactions to create volumetric sources and sinks of plasma within the simulated region. These enhancements have been used to pursue the following main lines of investigation:

1) What role, if any, Charon plays in the interaction between the Pluto-Charon system and the solar wind.

2) With the inclusion of volumetric ion source and loss terms, how did anomalous solar

wind parameters during the the New Horizons flyby impact the observed system.

3) How does the presence of an ionosphere around Europa alter the moon's induced dipole signal.

1.3.2 Chapter Descriptions

The work presented here was undertaken using an enhanced version of the multifluid MHD model used to study the Ganymede system (C. Paty and R. Winglee, 2004; C. Paty and R. Winglee, 2006; C. Paty et al., 2008). The first modification that was carried out was the extension of the model structure to permit an arbitrary number of planetary bodies to be placed freely within the simulation domain. The next major addition was the implementation of neutral interactions with plasma in the system. This consisted of mass, momentum, and heat exchange between the plasma population and the neutral population through electron impact ionization, ion-neutral charge exchange, and photoionization. This was supported by the addition of support for neutral atmospheric distributions within the model, based on observational data.

Chapter 2 gives background on the Pluto-Charon system, including a brief history of the evolution of knowledge about the dwarf planet and its companion. Mechanisms by which Charon could transiently possess an ionosphere are explained as well as constraints on the body's current atmospheric density. An overview of the New Horizons mission, including relevant dates and of the encounter geometry and trajectory is given. We provide information about instruments on board the spacecraft that have provided data pertinent to the research described in this document. Data and analysis from the encounter is also provided in order to highlight how pre-encounter expectations diverged from what was observed.

Chapter 3 goes over information on the Europan plasma environment. This includes an introduction to the Jovian magnetosphere in order to provide context for the investigation. Jupiter's magnetic dipole and how its tilt from the rotation axis causes periodic variations in the background magnetic field at Jupiter is discussed. We relate key information about the Jovian plasma sheet such as temperature, density, and velocity as well as the same values for plasma outside of the plasma sheet. We also characterize the Europan exosphere. This includes how it is generated, how it is understood to be distributed over the surface of Europa, and what it is composed of. Finally, the detection, cause, and variability of Europa's induced magnetic dipole is communicated. Published spacecraft instrument data is provided where it is necessary for the discussion of each of these topics.

Chapter 4 contains descriptions of past modeling efforts at Pluto and Europa in order to provide a frame of reference for the present work. It also has breakdowns of all cases simulated for each investigation. Further, all notable parameters used in each case are given, along with the source or reasoning behind their use. With this established, the basic framework of the model is described, as well as the governing equations used. Having described the initial state of the model, we go on to discuss additions that have been made the model. These consist of the addition of photoionization, electron impact ionization, and ion-neutral charge exchange. This involves the treatment of mass loss and addition, momentum loss and addition, and heat exchange between the neutral and plasma populations. Cross sections for each process and for the chemical species at each body are provided, either in the form of plots, or equations. We then explain how we incorporated multiple bodies into the model, as well as how we have implemented Europa's induced dipole within the model. Interior boundaries and upstream conditions are then described.

Within Chapter 5 we discuss results of our investigation into the solar wind interaction with the Pluto system and Charon's effect on it. Analysis of the initial cases is organized based on different aspects of the system's behavior. Firstly, an overview of the system characteristics without Charon's presence is given in order to provide a baseline to compare against. Next, we discuss structural effects that Charon has on the system. Following this, heavy pickup ions and associated asymmetries within the system are described. Different aspects of the Plutonian plasma wake are then discussed, including mass loss from the system, the plasma sheet, and material deposition on Charon. The follow up study using the modified version of the model with ion neutral interactions to explore the impact of upstream plasma conditions on the system is then detailed. Last of all, results from the model are compared against data and other models in order to assess their validity.

Chapter 6 concerns the results of our investigation into the Europan plasma environment. First, the effects of Europa's location with the Jovian magnetosphere are discussed, then the rate of material loss from Europa's ionosphere to the greater magnetosphere. We next delve into the impact that Europa's ionosphere has on the system, such as changes to the induced field structure, the formation of Alfvén wings around the body within the sub-Alfvénic plasma environment, and the development of currents around Europa. Validation against other modeling results and spacecraft data is then performed.

Chapter 7 encompasses conclusions to the Pluto investigations and the Europa investigations. Additionally, it covers topics of future work that either could be or is being undertaken with the Icy Bodies Model. The first topic that we plan to pursue is to use dynamically varying upstream plasma conditions in the model so that we can delineate the effects of rapid or transient changes to system conditions. Improvements to analysis techniques are

then described, particularly creating synthetic spectrograms for comparison against spacecraft data as well as injecting tracker particles into the system in order to look into the generation of aurora around bodies. We then talk about further enhancements to the model that could be made to increase its fidelity. Finally, we provide a non-exhaustive list of potential objects that could be usefully studied with the Icy Bodies Model.

CHAPTER 2

THE PLUTO-CHARON PLASMA ENVIRONMENT

Pluto's discovery in 1930 was followed several decades later by that of its companion, Charon, in 1978. Here we will be exploring the role that Charon plays in the system's interaction with the solar wind as a result of the unique properties of the Pluto-Charon system, including those of Pluto's atmosphere. Therefore, we will first discuss what was known at the time that this investigation was begun, followed by what is known now.

2.1 Pre-Encounter Knowledge

2.1.1 Pluto and Charon

Following the confirmation of its existence through stellar occultation in 1989, Pluto's atmosphere has undergone notable and unexpected change. This consists of a large and sustained increase in estimated surface pressure, from $\sim$5 μbar in 1988 (Elliot et al., 1989; Sicardy et al., 2003) to between 6.5 and 24 μbar in 2008 (Lellouch et al., 2009). This result was unexpected, as Pluto passed perihelion in 1989 and its atmosphere was therefore expected to be decreasing in surface pressure. Possible explanations for this include a change in albedo due to orbital orientation or changes in surface composition, as well as thermal inertia (Elliot et al., 2003). It had long been suspected that Pluto's atmosphere freezes out completely as it approaches aphelion. However, recent simulations done by Olkin et al. (2015) suggest that this is not the case. Pluto's primary atmospheric constituent is N_2 but it also contains 0.25% CH_4 and trace amounts of higher hydrocarbons (Stern et al.,

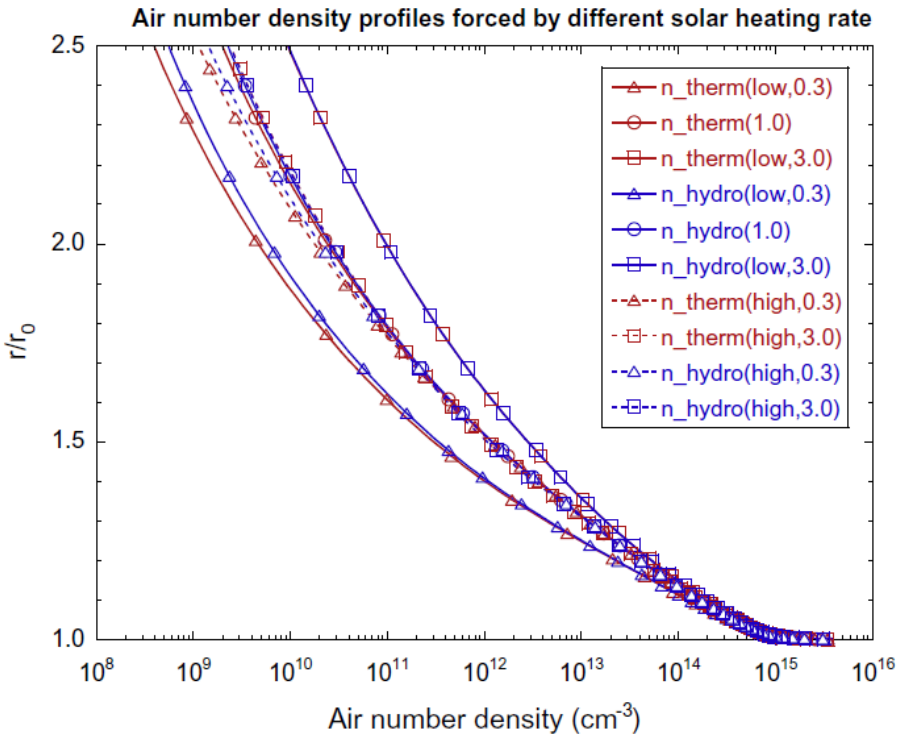

Figure 2.1: Plot of modeled atmospheric density profiles under different conditions performed before the NH encounter (Zhu et al., 2014).

2015b; Leslie A. Young et al., 1997). A thermal inversion was known to be present through much of Pluto's lower atmosphere, the surface temperature being ∼40 K and the peak atmospheric temperature approaching 100 K (Lellouch et al., 2009). Chemical modeling of Pluto's atmosphere indicated that ionospheric constituents consist of several distinct groups, centered at 28, 40, and 53 Da/q (Dalton/elementary charge), the most abundant of which being 28 Da/q, composed of $HCNH^+$ and $C_2H_5{}^+$ (Krasnopolsky and D. Cruikshank, 1999), with an aggregate surface number density of ∼750 cm^{-3} and a predicted peak ion temperature of ∼130 K (Sicardy et al., 2003). Figure 2.1 shows a plot of what modeling, based on measurements from stellar occultations, predicted the atmospheric structure to be. Note the expansive nature of the modeled atmosphere, resulting from expectations of high atmospheric loss rates.

Charon, had been measured to be over half of Pluto's radius (1 $R_P \approx 1187$ km and 1 $R_C \approx$ 606 km (Stern et al., 2015b)), orbits 16.5 R_P from Pluto with a period of 6.4 days (M. W. Buie et al., 2006), and has a surface that is compositionally distinct from Pluto (almost exclusively H_2O in contrast to widespread N_2 and trace methane ices present on Pluto , which are more volatile (Stern et al., 2015b)). Like Pluto, Charon was not expected to have an intrinsic magnetic field (Cravens and D. Strobel, 2015). This mixture of features results in a unique situation in which a moon might have a large impact on the solar wind interaction of its companion on a continuous basis.

2.1.2 Ambient Conditions

Before the New Horizons system encounter, the only sources of information on the likely magnetoplasma conditions in the vicinity of Pluto were data collect by the Voyager spacecraft when they were at similar radial distances from the Sun and modeling of propagation of the solar wind into the outer solar system based upon measurements made in the inner solar system. The Voyager spacecraft were equipped with several instruments for studying the magnetoplasma environment in interplanetary space: the MAG magnetometer, the PLS plasma spectrometer, the LECP charged particle detector, and the PWS plasma wave sensor (details of which can be seen in Section A.2 in Figures A.12, A.13, A.14, and A.15). Some issues with this are immediately apparent. The Voyager instruments were designed in the early 1970's, meaning that the fidelity of measurements were poor compared to more modern investigations. Voyager 1 was well outside of the ecliptic plane of the solar system by the time it reached a distance from the Sun equivalent to Pluto's at the time of the New Horizons encounter ($\sim$33 AU), and therefore was not measuring typical plasma parame-

ters that would be present in the ecliptic at that distance. Furthermore, Voyager 2, which stayed within the ecliptic until it was at the relevant distance – in order to perform a flyby of Neptune and its large moon, Triton – last took measurements of the region $\sim$26 years prior to the New Horizons encounter with Pluto. As the solar cycle is $\sim$11 years in length, this means that Voyager 2's data was from a period that was near the other extreme of solar activity, decreasing its utility for predicting conditions at the time of the New Horizons encounter.

Modeling of the propagation of the solar wind can be challenging, as population distributions can change significantly with radial distance. Nevertheless, Richardson and C. W. Smith (2003) have modeled the radial temperature profile of solar wind ions into the outer solar system (an ion temperature of $\sim$9000 K was predicted at Pluto's location) and Chashei and Fahr (2014) have studied electron heating effects in the outer solar system. Using Voyager measurements, such as those published by Ness et al. (1989), and modeling, predictions of the solar wind conditions that were likely during the encounter were made. Bagenal et al. (2015b) concluded that solar wind velocity would be approximately 380 km/s and (Bagenal et al., 1997) predicted a number density of $\sim$0.01 H^+ cm^{-3} and magnetic field strength of 0.2 nT.

2.1.3 How Charon Could Possess an Atmosphere

There are several possible mechanisms that have been proposed through which Charon could at times possess a trace atmosphere and therefore ionosphere. These include a water group atmosphere sourced from cryovolcanism (Cook et al., 2007), a parasitic N_2 atmosphere derived from material escaping from Pluto (Tucker et al., 2015), and a transient,

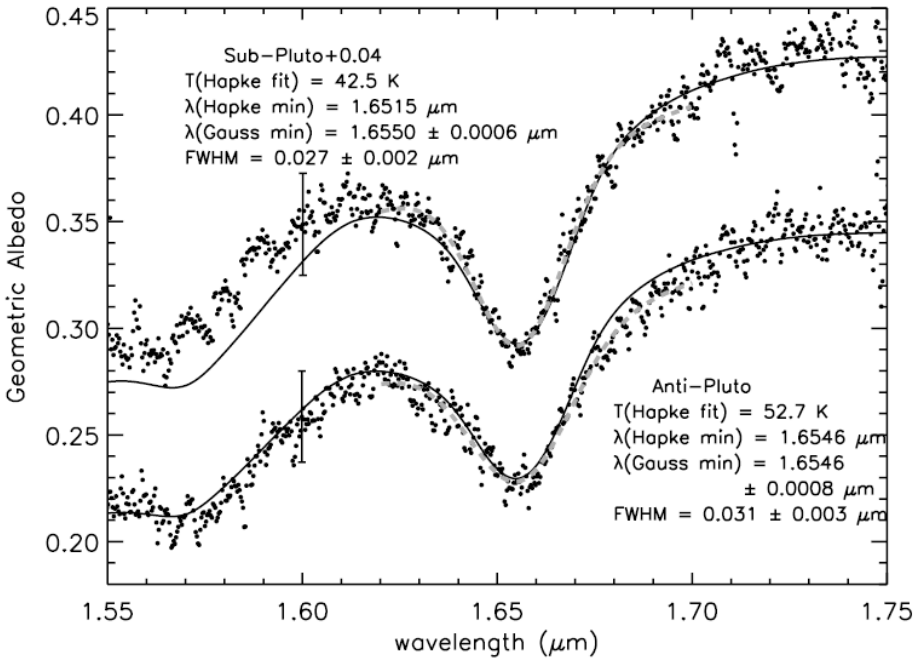

Figure 2.2: Spectra of Charon's hemispheres which show a crystalline water ice signature. Solid lines are fits for a modeled crystalline water ice signature and dashed lines are fits of the measured feature (Cook et al., 2007).

impact-sourced atmosphere (Stern et al., 2015a).

Cook et al. (2007) used ground based NIR observations to obtain spectra of Charon's surface in order to gain insight into the the composition of the body. As is shown in Figure 2.2, they observed a feature centered at 1.65 μm which, in combination with spectral models, they interpreted as a signature of crystalline water ice. This was surprising, as it was believed at the time that crystalline water ice would be transformed into amorphous water ice by UV radiation over a relatively short period of time (tens of thousands of years). Because it was believed that this feature must be young, the authors proposed that there had been recent resurfacing of the surface of Charon and suggested that cryovolcanism was the most likely mechanism by which this could be achieved. If this had been the case, then it would be likely that a trace atmosphere would be generated around Charon as well, at least for a

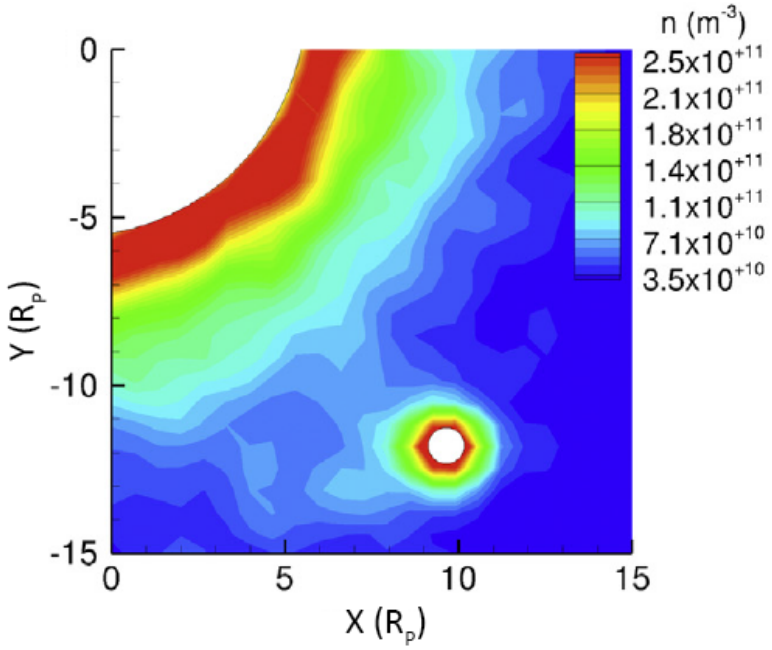

Figure 2.3: Density of outflowing and captured gas around Charon from Tucker et al. (2015). White region around Pluto (top left) is below the assumed exobase.

certain period of time after eruptions.

Another mechanism by which it seemed possible that Charon could possess an atmosphere was put forward by Tucker et al. (2015), in which Charon would capture material escaping from Pluto's atmosphere. They used a Monte Carlo technique in order to track the movements of particles escaping from Pluto's exobase to determine that Charon would capture enough of them to form an atmosphere. This included material that was gravitationally captured as well as material that impacted the Charonian surface, only to be reemitted. Charon would therefore have a parasitic atmosphere, dependent upon the retention time of the acquired material, as well as the rate of atmospheric loss from Pluto. Figure 2.3 shows results from their effort with estimated peak number densities for the modeled atmosphere of 2.5×10^{11} N_2 cm^{-3}. This work was based on the expectation before the New Horizons encounter that Pluto's atmosphere would be highly extended and rapidly escaping.

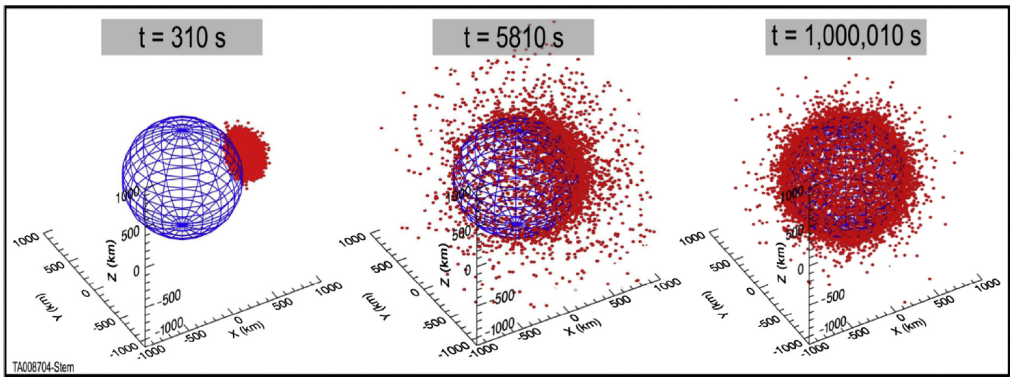

Figure 2.4: Evolution of a transient atmosphere following KSI impact on Charon (Stern et al., 2015a).

A third way in which Charon could develop an atmosphere – although only a transient one in this case – that was suggested was through kilometer-scale Kuiper Belt Objects (KBO's) impacting the surface of Charon and creating an atmosphere with ejecta. This work by Stern et al. (2015a) used modeling of such an event to determine that a kilometer-scale impactor (KSI) would eject enough material from the surface of Charon to create an atmosphere that could last up to 1000 years. Probabilistic modeling based on the known population of KBO's in relevant orbits indicated that Charon would be struck by a KSI roughly once every million years. Smaller impactors, which would still be expected to create a similar, but smaller and less long lived phenomena, were estimated to strike Charon at more frequent intervals. This would indicate that Charon possesses a transient water group atmosphere $> 0.1\%$ of the time.

2.2 New Horizons Results

2.2.1 Encounter Description

The New Horizons encounter with the Pluto-Charon system began several days before closest approach to Pluto with remote observations of the system using the remote sensing instruments on board the mission. This was partially necessary due to the long rotational period of the main bodies, Pluto and Charon, which are mutually phase locked to each other ($\sim$6.4 day period). Mapping of the surfaces of each body therefore had to begin almost one week beforehand in order to achieve coverage of the illuminated hemispheres. For the purposes of plasma modeling, however, the most important period of the encounter was in the 12 hours surrounding closest approach (11:58:59 UT on July 14, 2015), as this was the time during which plasma measurements by the Solar Wind Around Pluto instrument (SWAP) (McComas et al., 2009) and the Pluto Energetic Particle Spectrometer Science Investigation (PEPSSI) R. L. McNutt et al. (2008) were within what was expected to be the interaction region between the solar wind and the Pluto system. Figure 2.5 shows the geometry of the encounter with times for closest approaches and occultations indicated.

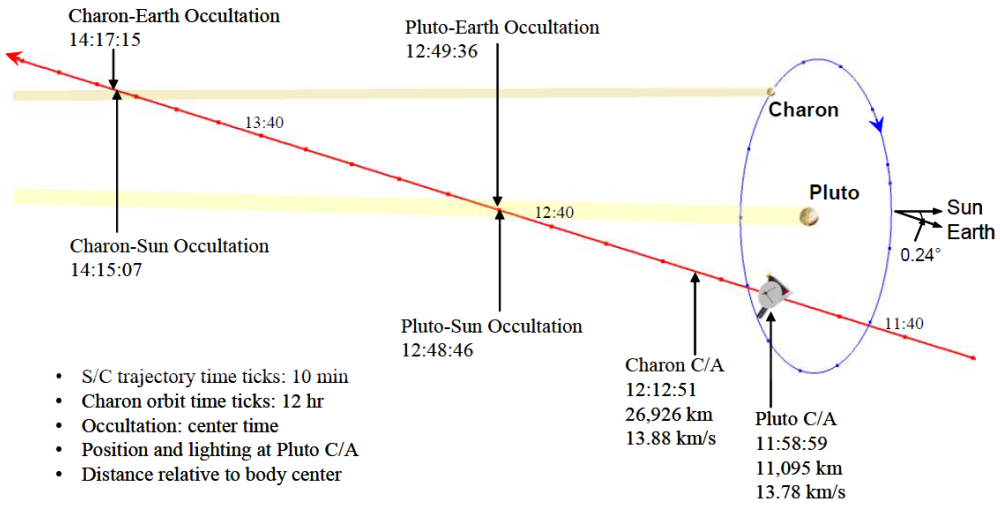

Figure 2.5: Trajectory for New Horizons encounter with the Pluto-Charon system from Guo and Farquhar (2008). Key events are indicated, along with time in UT. Red line indicates the New Horizons trajectory and the shaded regions show Pluto and Charon's shadows.

2.2.2 Observed Atmosphere at Pluto

Results from the New Horizons encounter indicate that Pluto's atmosphere is more compact and slightly cooler than modeling based on stellar occultations had suggested, at 70 K (D. F. Strobel and Zhu, 2017). Gladstone et al. (2016) used UV solar occultations of Pluto's atmosphere to generate temperature and density profiles for different atmospheric constituents up to an altitude of 1800 km. They found a surface pressure at the time of the New Horizons encounter of $\sim$10 μbar. As can be seen in Figure 2.6, the density of most atmospheric constituents drops off much more quickly than had been predicted based on pre-encounter occultations, such as those in Figure 2.1. Not only did they find that the atmosphere was more compact than expected (radio occultations performed by the REX instrument were used to observe the lower atmosphere, while UV occultations from Alice were used for the upper atmosphere and exosphere), CH_4 was the dominant species above 1800 km in

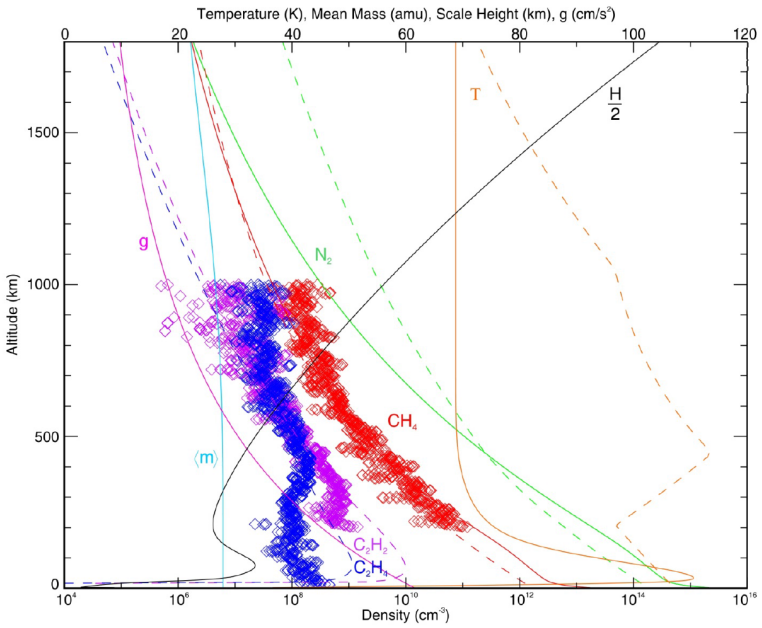

Figure 2.6: Altitude profiles for temperature and number density for different species in the Plutonian atmosphere based on observations by the Alice UV spectrometer and REX instrument (Tyler et al., 2009) on the New Horizons mission (Gladstone et al., 2016).

altitude and accounted for the majority of material escaping from the atmosphere, with an estimated escape rate of $5 \cdot 10^{25}$ s^{-1} compared to 10^{23} s^{-1} for N_2 (Gladstone et al., 2016) (these rates are 1/2 and 1/20,000 of those predicted before the New Horizons encounter, respectively (Zhu et al., 2014; Erwin et al., 2013; Koskinen et al., 2015)). Another interesting detail observed during the encounter was the presence of global and highly structured hazes extending throughout the upper atmosphere of Pluto (Stern et al., 2015b).

2.2.3 Plasma Conditions

During the encounter, a higher than anticipated solar wind density of 0.025 H^+ cm^{-3} was measured, 2.5$\times$ the predicted value, and a lower than expected ion temperature of 7700 K (Bagenal et al., 2016). The solar wind velocity measured during the encounter, however, was somewhat close to the predicted value at 403 km/s (Bagenal et al., 2016). Figure 2.7

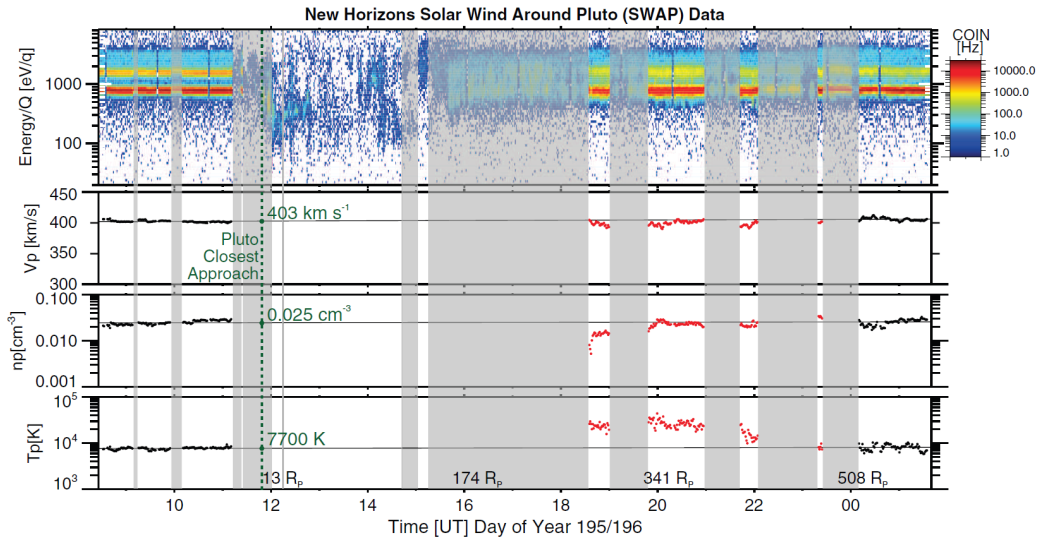

Figure 2.7: (Top) Energy per unit of charge, (Upper Middle) ion velocity, (Lower Middle) ion number density, and (Bottom) ion temperature are plotted for the New Horizons encounter with the Pluto-Charon system. Shaded regions of the plot indicate that SWAP was not within 5° of pointing towards the Sun (Bagenal et al., 2016).

shows data from the SWAP instrument with overlays indicating periods when the instrument was not pointing towards the direction of the free stream solar wind flow, as well as plots of ion velocity, density, and temperature derived from the data.

McComas et al. (2016) used data from the SWAP instrument to develop a conceptual model of the structure of Pluto's interaction with the solar wind, shown in Figure 2.8. Their estimate of the interaction structure includes what the anticipated bow shock stand off distance is upstream of Pluto, as well as what portion of the wake is sheath material, versus heavy pickup ions. This was done by separating particles detections into heavy and light ions through secondary count rate measurements. They concluded that the bow shock created by the interaction of the solar wind with Pluto's ionosphere is 4.5 R_P upstream from the body, and that New Horizons was within Pluto's wake until it was at least 150 R_P downstream of the body. Zirnstein et al. (2016) used data from SWAP to determine

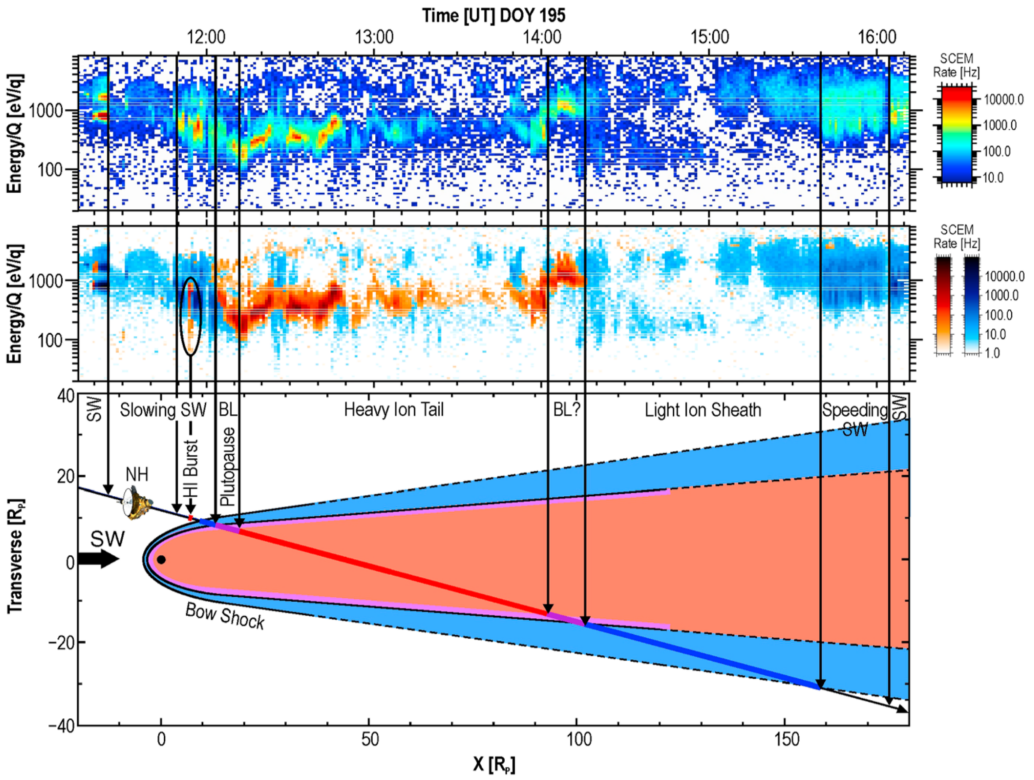

Figure 2.8: (Top) Spectrogram of secondary count rates, (middle) rates separated into light and heavy ions, and (bottom) diagram of modeled interaction structure based on data with NH trajectory overlaid (McComas et al., 2016).

possible directions of the IMF, concluding that it was pointing within 20° of the ecliptic and within 90° of the direction opposite to Pluto's orbital motion. They also concluded that there was no IMF direction that was compatible with the pickup ions measured having been N_2^+ instead of CH_4^+. In terms of IMF direction, this is compatible with all simulations reported within this dissertation. The preclusion of N_2^+ as the dominant species of pickup ion in the system was already discovered and was acted upon in our follow up work, as is discussed in Subsection 4.1.2.

Measurements taken by PEPSSI largely corroborate the findings made by SWAP, as can be seen from the plots in Figure 2.9. Notable features include the observation of energetic particles near closest approach that are interpreted as flow that had been deflected by the

obstacle, as well as the presence of heavy ions in the wake region.

An additional feature that PEPSSI observed is shown in the plot in Figure 2.10, which has time of flight (TOF) count rates mapped along the trajectory of the New Horizons spacecraft, along with relevant geometry and events. The figure shows a large enhancement of particles in the region within the geometric shadow of Charon at roughly the distance that material picked up from the body would be expected to be.

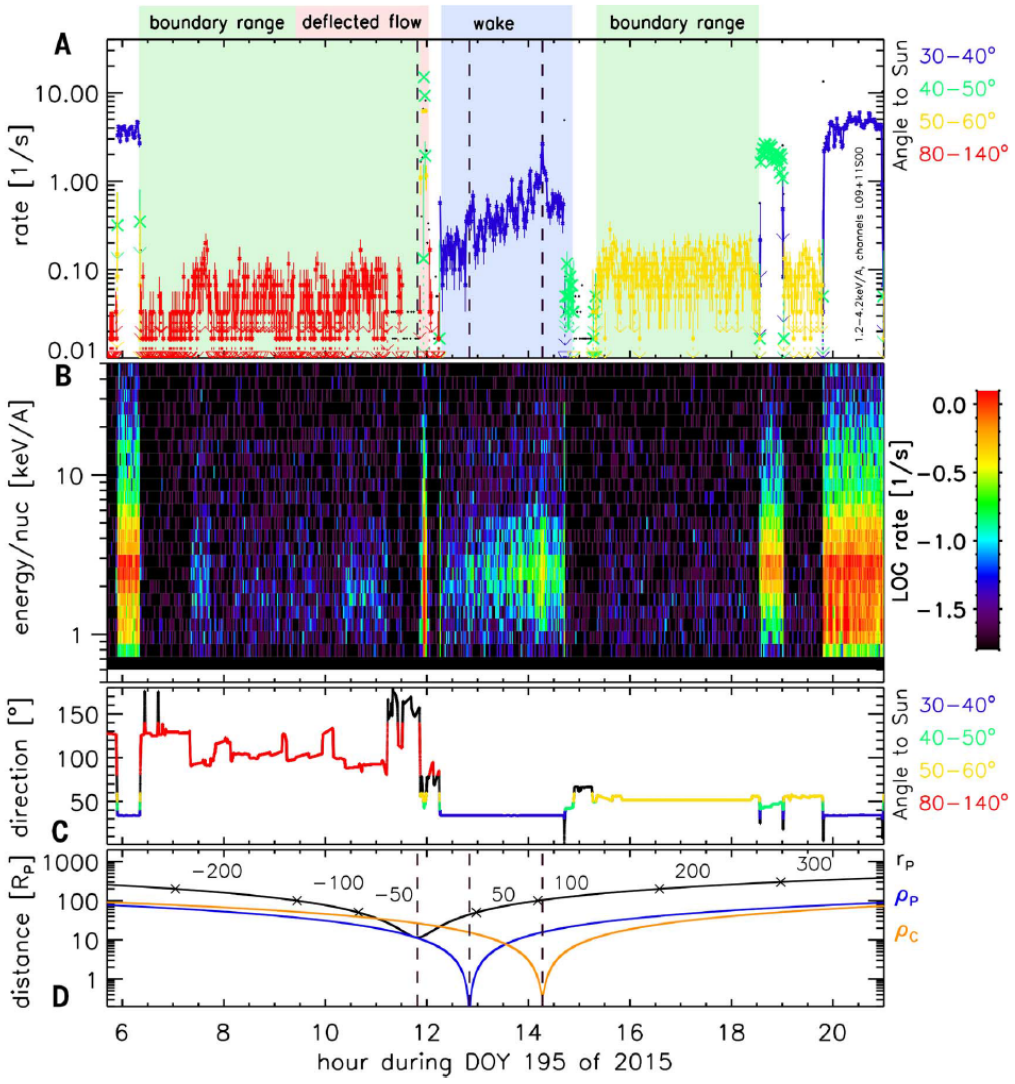

Figure 2.9: (Top) TOF count rates, (Upper Middle) TOF energy spectrogram, and (Lower Middle) angle between PEPSSI S0 and Sun direction, and (Bottom) Distances from Pluto (black), Pluto-Sun line (blue), and Charon-Sun line (orange) (Bagenal et al., 2016).

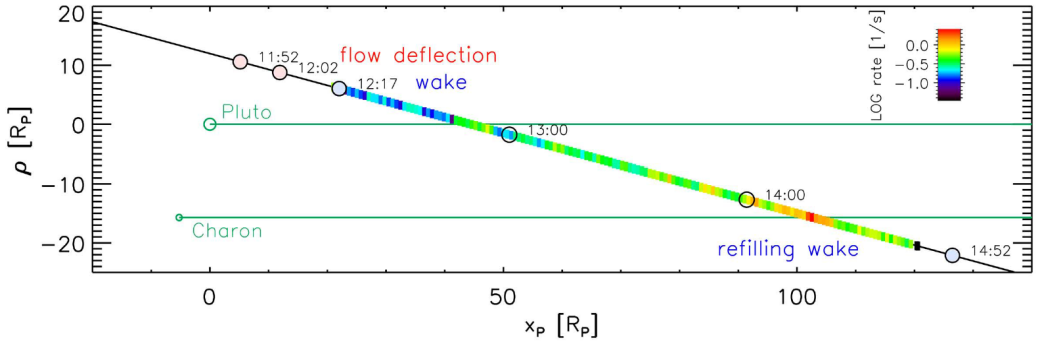

Figure 2.10: TOF count rates are mapped on top of the NH Trajectory. Plane contains NH Trajectory and Pluto. Note enhancement coincident with Charon-Sun line (Bagenal et al., 2016).

2.2.4 Constraints on Charon's Present Atmosphere

The average age of Charon's surface (Jeffrey M. Moore et al., 2016) makes it unlikely that cryovolcanism has recently occurred on Charon, although Desch and Neveu (2017) observed clear evidence of ancient cryovolcanic activity. Experiments by Zheng et al. (2009) show that irradiation of crystalline water ice under the conditions present at Charon could only result in partial amorphization due to a strong temperature dependence, thereby explaining the crystalline water ice signature identified by Cook et al. (2007) without recent cryovolcanism. Similarly, measurements by the Alice UV spectrometer aboard New Horizons, shown in Figure 2.11 appear to preclude Charon currently possessing an atmosphere (Gladstone et al., 2016), with upper limits placed on densities for all species at or below 0.3 nbar. However, the craters which appear to rule out recent cryovolcanic activity on Charon reaffirm that large impactors periodically hit Charon, demonstrating that Charon must go through phases of possessing an ionosphere (Stern et al., 2015a). Beyond this method, modeling by Stern et al. (2017b) and Alissa M. Earle et al. (2017) suggest that Pluto's atmosphere undergoes large scale fluctuation in pressure and temperature over ge-

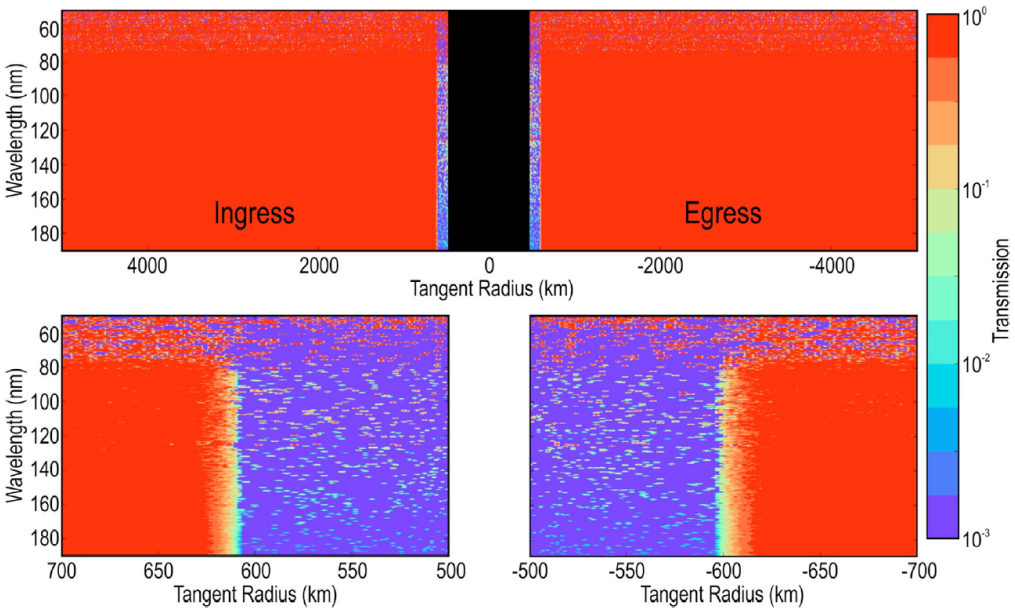

Figure 2.11: Transmission of UV wavelengths is plotted against tangent radius (distance from center of body) for the Alice occultation of Charon. No evidence of a current atmosphere is observed (Stern et al., 2017a).

ological time scales due to changes in albedo and inclination and that Pluto is presently at a predicted minimum. Additionally, work by Keane et al. (2016) indicates that continued loading of volatiles into Sputnik Planitia could result in changes to Pluto's orientation, potentially altering its climate. This reopens the possibility of a parasitic atmosphere being present at Charon during periods in which Pluto has a more significant atmosphere.

This means that, during these periods in which Charon possesses an ionosphere, an ion source distinct from that of Pluto is moving through the Pluto system. In addition to this, the presence of an ionosphere around Charon must appreciably increase any alteration or obstruction of plasma flows within the system that are caused by Charon. While in the freestream flow upstream of Pluto – as the compact Plutonian atmosphere reported by Gladstone et al. (2016) suggests that Charon is for much of its orbit – Charon is likely to significantly modify conditions of the flow incident upon Pluto's ionosphere. This pos-

sibility is intriguing, as, while many moons locally alter the shock of their parent bodies while crossing the shock (Nishino et al., 2011), the only similar occurrence in which the moon was directly upstream of the parent body that has been observed within the solar system was during Cassini's T96 flyby of Titan, when Titan was determined to be outside of Saturn's bow shock (Bertucci et al., 2015). However, Charon's large size relative to Pluto compared to Titan's relative to Saturn indicates that any effect would be more significant on a global scale. A plausible result of this is that Charon could cause a decrease in atmospheric loss from Pluto through shielding from the solar wind. Another possible effect of Charon on Pluto's plasma environment is the modification of Pluto's plasma wake structure. This could be due to either physical obstruction by Charon itself or by the introduction of plasma into the region.

CHAPTER 3

THE EUROPAN PLASMA ENVIRONMENT

One of the Galilean moons of Jupiter, discovered in 1610 by Galileo Galilei, Europa has been a topic of study for centuries. Magnetic field measurements made almost 400 years later by Galileo's eponymous spacecraft suggested the presence of a saline ocean below Europa's icy surface. This investigation aims to separate the induced signature of the ocean from that of the moon's ionosphere. We will therefore now give the necessary context for understanding the Europan plasma environment.

3.1 The Jovian Magnetosphere

3.1.1 Jovian Magnetic Field Structure

The Jovian magnetosphere is the largest magnetospheric plasma structure within the heliosphere, typically extending three million kilometers from the gas giant's surface in the direction of the Sun. This is because, as was shown in Equation 1.1, when a body possesses an intrinsic magnetic field the bow shock stand off distance of that body's magnetosphere is determined by the strength of the body's intrinsic magnetic field. Jupiter's magnetic dipole, exhibiting a magnetic field strength of 428,000 nT at the equator (moment $\sim 1.56 \times 10^{20}$ T·m^3), which is roughly 14$\times$ the strength of the Earth's magnetic field at the equator ($\sim$31,000 nT at the equator, moment $\sim 7.9 \times 10^{15}$ T·m^3), is the strongest of any body within the solar system other than the Sun (moment $\sim 3 \times 10^{23}$ T·m^3) (Tholen et al., 2002).

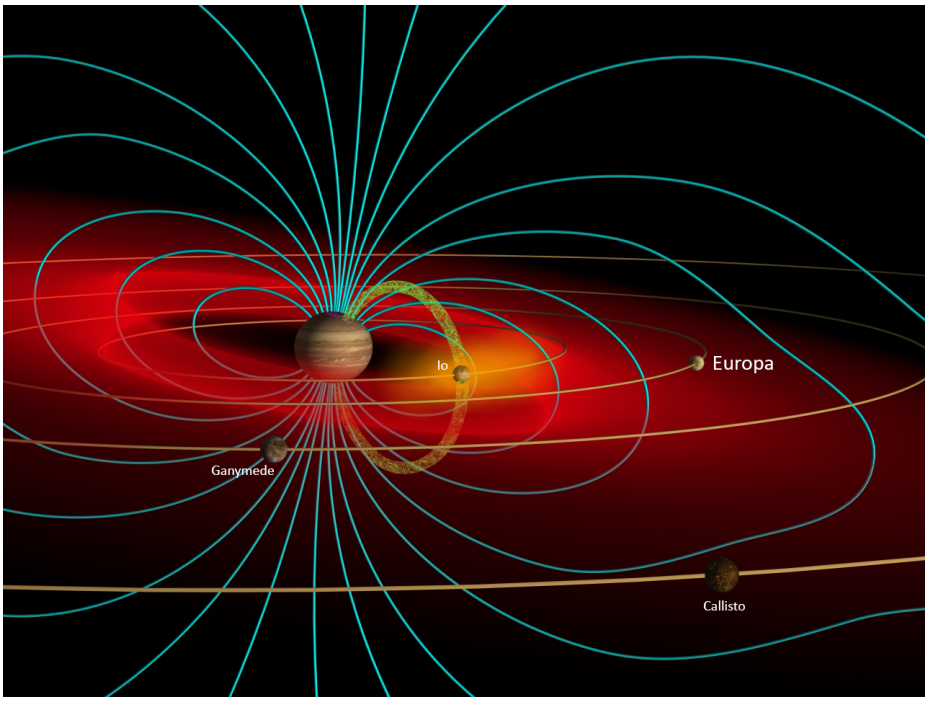

Figure 3.1: Diagram of the Jovian magnetosphere with Galilean satellites labeled. Teal lines represent field lines from Jupiter's magnetic field. Red material represents plasma sheet sourced from Io and Europa. Modified from original image by J. Spencer (1999).

Figure 3.1 shows a depiction of the Jovian magnetosphere with magnetic field lines at various radial distances from the body included. As can be seen, the axis of Jupiter's magnetic dipole is tilted relative to the spin axis of the planet, with an inclination of $\sim$10°. This causes the dipole to wobble as Jupiter rotates over the course of its day (9 hours and 56 minutes). This results on a disparity between locations within the Jovian magnetosphere – where something is relative to features within the Jovian magnetosphere – and orbital locations around Jupiter. As a consequence, objects such as Europa are subjected to periodic changes is magnetic field strength and orientation (which will be discussed further in Section 3.3), as well as incident plasma populations (as will be explained in the next subsection). Within the inner region of the Jovian magnetosphere, which is the region where Europa is positioned, the dipolar structure of the magnetic field is retained. This is not the

case throughout the magnetosphere.

3.1.2 Plasma Sheet

The plasma sheet is a region of Jupiter's magnetosphere in which there is a higher density of plasma than in other section of the magnetosphere. This region is represented in Figure 3.1 by the areas with red coloration. This is the corotational plasma population within a magnetosphere that was mentioned in Section 1.1, and is concentrated in latitude near Jupiter's magnetic equator. A consequence of the tilt of Jupiter's magnetic dipole that was mentioned in the previous subsection is that material in the Jovian plasma sheet moves up an down in latitude from the perspective of objects in Keplerian orbits around Jupiter.

Material within the Jovian plasma sheet originates from several sources, including volcanic material from Io, the solar wind, and particles ejected from Europa's surface. It has long been known that Jovian plasma interacts with Europa in important ways (Wolff and Mendis, 1983). The material from Io is the dominant thermal species within the region that extends from Io's orbit around Jupiter ($\sim$6 R_J) to just within the orbit of Europa ($\sim$9.6 R_J, but still contributes a significant amount of the material present outwards from this region (Bagenal, 1994; Bagenal et al., 2015a). Particles sourced from the solar wind make up the higher energy component of the Jovian plasma sheet population and therefore constitute a higher percentage of the overall plasma population at greater magnetic latitudes. This is because more energetic particles engaging in bounce motion along a dipolar magnetic field line will be able to travel farther along the field line before reaching their mirror points (the point at which all velocity parallel to the direction of the magnetic field line has been converted into motion perpendicular to the magnetic field line), assuming equal pitch angles (the

angle between the component of the particle's velocity that is parallel to the magnetic field line and the component that is perpendicular to the magnetic field line when the particle is at the magnetic equator). Near the orbit of Europa, plasma that consists of ionized material that came from Europa's exosphere gains relative importance within the thermal portion of the Jovian plasma sheet (Delamere et al., 2005).

The farther out from Jupiter's surface, the more the mass of plasma corotating within the plasma sheet distorts the dipolar shape of the Jovian magnetic field. This is a result of the weakening of Jupiter's magnetic field strength with increased distance from the surface of the body, combined with the growth in torque that is required in order to maintain the corotational (super-Keplerian) speed of the plasma within the plasma sheet. This causes corotation lag, whereby material within the plasma sheet is moving at super-Keplerian but sub-corotational speeds and simultaneously bends magnetic field lines near the magnetic equator in the anti-corotational direction. This phenomenon is present at Europa's orbital distance and results in the Jovian background magnetic field having a component in the corotational direction, as well as in the radial and Z directions (where Z is parallel to Jupiter's spin axis) (Volwerk et al., 2001; Zimmer et al., 2000; Kivelson et al., 2000). Work by Paranicas et al. (2002) and Paranicas et al. (2009) suggest that the plasma population near Europa's orbit does not typically vary by more than a factor of two to five in number density. Farther out, the magnetic field lines also begin to bulge outwards, which ultimately results in plasma interchange events, during which magnetic flux tubes with high plasma densities move radially outwards from Jupiter and relatively unpopulated magnetic flux tubes move radially inwards.

3.2 Europa's Exosphere and Ionosphere

While Europa does not possess an atmosphere, it does have an exosphere. The difference between an exosphere and an atmosphere is that an atmosphere is both gravitationally bound to the body that it surrounds, and is collisional, while an exosphere is only gravitationally bound to the body. Here, we define collisional as meaning that the Knudsen number of the gas is significantly less than one ($Kn_n = \frac{\lambda_n}{H_n}$, where λ_n is the mean free path and H is the scale height). The mean free path for a Maxwellian population is given in Equation 3.1, in which k_B is the Boltzmann constant, T_n is the temperature, σ_n is the average cross sectional area of the neutral species, and P_n is the pressure. Note that near the surface of Europa, the exosphere is nearly collisional, meaning that it is on the cusp of being a true atmosphere (Hall et al., 1995; M. A. McGrath et al., 2004).

$$\lambda_n = \frac{k_B T_n}{\sqrt{2}\sigma_n P_n} \tag{3.1}$$

The scale height is given by Equation 3.2, where m_n is the molecular mass of the species and g is the gravitational acceleration ($g = 1.315 m/s^2$ at Europa's surface).

$$H_n = \frac{k_B T_n}{m_n g} \tag{3.2}$$

Because the Europan exosphere is non-collisional, its particles travel on ballistic trajectories, which means that surface interactions are necessary for it to be maintained. Particles from this exosphere are ionized through various processes such as electron impact ionization and photoionization, and create an ionosphere around Europa, which alters the moon's

interaction with the Jovian magnetosphere. Below, we will discuss the sources, composition, and distribution of Europa's exosphere and ionosphere.

3.2.1 Sources

The Europan exosphere is primarily generated by the bombardment of Europa's surface by energetic Jovian magnetospheric plasma (Saur et al., 1998) through a process known as sputtering. A significant portion of this incident plasma is sourced from eruptions of Ionian volcanoes farther in the Jovian magnetosphere, as mentioned in Subsection 3.1.2, as well as some material from the solar wind. Europa's orbit places it slightly outward from the Io plasma torus mentioned in Subsection 3.1.2. This means that much of the material impacting the Europan surface is actually material from the Europan exosphere that has been ionized ($\geq$20% according to Ip (1996)). Multiple factors affect the production rate of exospheric material by sputtering. These include temperature of the ice, the species impacting the ice, and the energy of the impacting particles (Shi et al., 1995; Famá et al., 2008; Cassidy et al., 2010; Johnson et al., 2009). Another method by which Europa gains exospheric material is through sublimation, although this material is of such low energy that it is confined to the volume very near to Europa's surface (J. R. Spencer et al., 1999).

As we have mentioned, Europa's ionosphere is generated through the ionization of material from the exosphere. This occurs through three main processes: electron impact ionization, ion-neutral charge exchange, and photoionization. Of these processes, electron impact ionization is the most important at Europa. Electron impact ionization primarily occurs on the anti-corotational side of Europa, as electrons have much smaller gyroradii than ions, meaning that even very energetic electrons have trouble reaching the corotational side of

Europa. Photoionization makes a lesser contribution than electron impact ionization in total production rate, but, as it is not restricted to the one hemisphere of Europa, it can create ionospheric plasma where other processes cannot. Ion-neutral charge exchange is the final significant source of ionospheric plasma around Europa. This process results in ions from the Jovian magnetosphere recombining by taking an electron from particles from Europa's exosphere, creating ionospheric plasma.

3.2.2 Composition

The Europan exosphere is primarily composed of O_2 sputtered from the moon's surface. In addition to this, an extended sodium exosphere has been detected around Europa by Hall et al. (1995) and Brown and R. E. Hill (1996). Furthermore, Brown (2001) observed potassium within the Europan exosphere. Because exospheric particles are all on random ballistic trajectories, there is no bulk flow direction within the neutral exosphere. The ionospheric population that is derived from this exospheric population is composed primarily of O_2^+, sourced from exospheric O_2. As the O_2^+ population is created from the O_2, it also has no bulk flow direction when it is initially ionized, although it does gain velocity as a result of electromagnetic forces acting on it.

3.2.3 Distribution

The Europan exosphere is not uniformly spread across the surface of the moon, according to numerous observations. Some of this asymmetry is to be expected as a result of the source of the exosphere (sputtering by incident energetic particles from the Jovian plasma sheet). This is because corotational plasma is moving faster than Europa, which is moving

at a Keplerian speed, and is therefore constantly overtaking the moon. This means that the hemisphere of Europa which is being overtaken by the corotational plasma – this is always the same side because Europa is phase locked to Jupiter – is struck by more plasma than the side facing Europa's direction of motion, and should therefore experience a greater rate of exospheric production. Observations reported by Lane et al. (1981), Noll et al. (1995), and Hendrix et al. (2011) support the presence of this hemispherical asymmetry. Hubble Space Telescope observations have been the basis for a number of efforts to model the Europan exosphere, including work by Shematovich et al. (2005), Smyth and Marconi (2006), Cassidy et al. (2008), Cassidy et al. (2009), Plainaki et al. (2010), and Plainaki et al. (2012).Saur et al. (2011) estimated that the minimum column density for exospheric O_2 is 10^{12} cm^{-2} (compare to $(1.5 \pm 0.5) \cdot 10^{13}$ cm^{-2} from Hall et al. (1995)). Observations reported by Hall et al. (1998) using data from the Cassini Ultraviolet Imaging Spectrograph (UVIS) are in agreement with these measurements, although C. J. Hansen et al. (2005) indicate additional spatial variability.

There are several mechanisms which could result in this more complex distribution of exospheric material. The first is that higher energy plasma is able to bounce farther along Jupiter's magnetic field lines. This means that, while thermal plasma that is corotating near Europa is confined to a fairly small range of magnetic latitudes, these energetic particles (which tend to have come from the solar wind, as was mentioned in Subsection 3.1.2) are able to access to opposite face of Europa and sputter material. Furthermore, work by Cassidy et al. (2007) and Cassidy et al. (2013) using HST data suggests that, not only is the Europan exosphere asymmetrical between the corotational (pointed in the direction of the movement of corotational plasma) and anti-corotational hemispheres, but that its source

rate also varies based on the texture and composition of different regions of the surface of Europa. Paranicas et al. (2009) have reported that some regions of Europa's surface experience little sputtering due to a combination of lowered accessibility to high energy JMP particles and surface properties. Surface composition is affected by radiolysis within Europa's surface, caused by the impacts of energetic electrons (Cassidy et al., 2010), which are more prevalent on the anti-corotational hemisphere (Paranicas et al., 2001). This is further complicated by the fact that O_2 that is sputtered from the Europan surface tends to be ejected repeatedly rather than sticking to the moon's surface at the end of a ballistic trajectory, effectively hopping randomly around the surface of Europa. This weakens the link between observable surface features and exospheric distribution. Paterson et al. (1999) reported a maximum heavy ion number density of 40 cm^{-3} during Galileo's closest approach to Europa during flybys E4 and E6 (distances from Europa of 700 km and 600 km, respectively). This provides a ceiling to the density of Europa's extended ionosphere. Figure 3.2 shows the observed exospheric distribution and Figure 3.3 shows electron density profiles above Europa – observe disparity between PLS and radio occultation densities at relevant altitudes. Also note that mapping of regional variations in exospheric density is not global, adding uncertainty to the average state of Europa's exosphere.

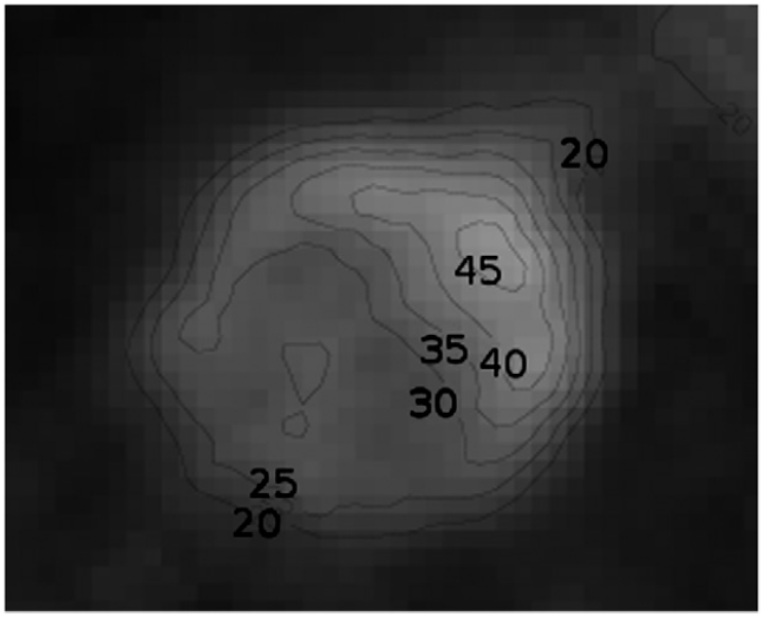

Figure 3.2: HST image of line emission at 1356 Åresulting from electron-impact dissociation of O_2 in Europa's exosphere. Calculated column density contours are overlaid with units of 10^{14} O_2 cm^{-2} (Cassidy et al., 2007).

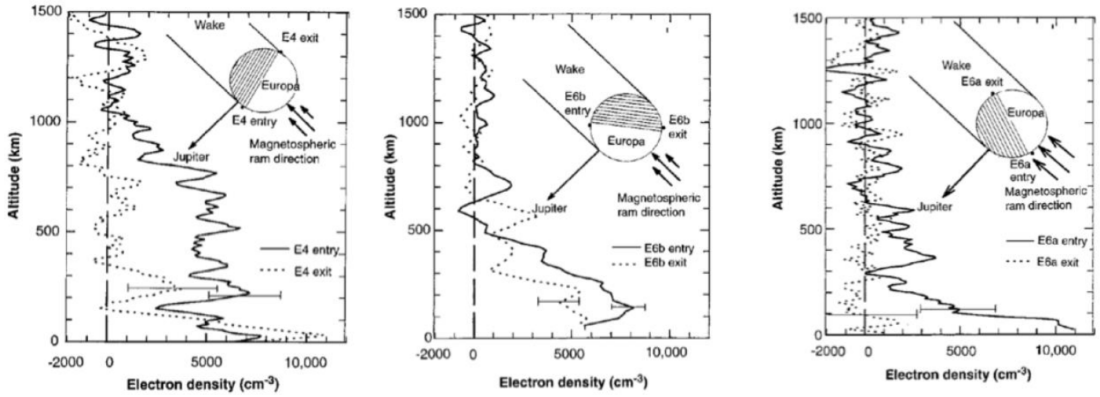

Figure 3.3: Radio occultation derived electron density profiles above Europa during multiple Galileo flybys. Modified from Kliore et al. (1997).

3.2.4 Water Plumes

Roth et al. (2014) observed what they interpreted to be plumes of water vapor above the surface of Europa in late 2012. Figure 3.4 shows the initial observations by the Hubble Space Telescope compared against emissions from a plume of water vapor above the Europan surface. Subsequent observations by Roth et al. (2017) did not detect a similar feature, but multiple observations by Sparks et al. (2016) and Sparks et al. (2017) using a different technique have indicated the presence of plumes. These detections have been interpreted as evidence of relatively frequent cryovolcanism on the surface of Europa (Sparks et al., 2017), and are believed to present an opportunity to probe the composition of the reservoir(s) of liquid water which are suspected to exist below the surface of Europa as a result of magnetometer measurements, as will be discussed further in the following section. It should be noted that, while plumes of water erupting above the surface of Europa would have to be sourced from a volume of liquid water below the surface, this source would not necessarily be the ocean proper. Research by Schmidt et al. (2011) suggests that subsurface melt lenses could exist on Europa. If present, such structures would be a more likely source for material ejected by plumes, due to the shorter distance that the liquid water would have to travel through cracks in the ice before reaching the surface compared to if it were to come from the ocean. Plumes of water vapor would also cause further spatial variability of the Europan exosphere (B. D. Teolis et al., 2017), altering interpretations of the moon's interaction with the Jovian plasma environment.

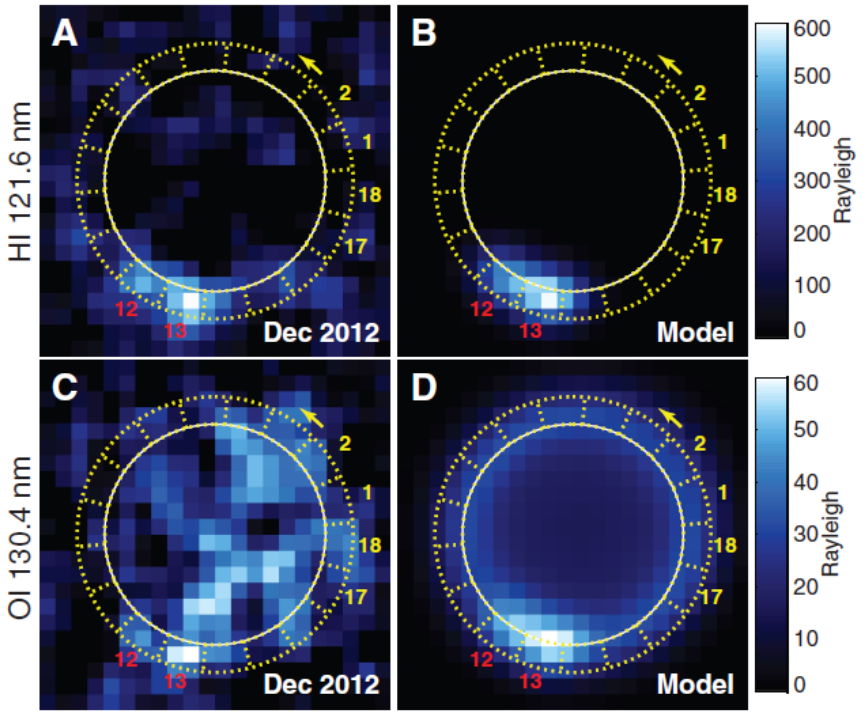

h

Figure 3.4: (Left) HST observations of Europa in December 2012, and (Right) model results for observations of water plumes above the Europan surface (Roth et al., 2014).

3.3 Europa's Induced Magnetic Dipole

3.3.1 Generation and Relevance

A magnetic dipole was detected within Europa through analysis of alterations made to the Jovian background magnetic field that were measured by the Galileo magnetometer (see Figure A.7) during flybys E4, E14, and E26 among others (Kivelson et al., 1997; Khurana et al., 1998; Kivelson et al., 1999; Kivelson et al., 2000). Figure 3.5 shows measurements of magnetic field components during these flybys of the moon, as well as how these measurements compare against the signal that would be expected from a highly conducting sphere (see Kivelson et al. (2009) for additional detail). It was eventually determined that the magnetic dipole coming from the moon was induced rather than intrinsic because its di-

rection changed depending on the orientation of the time-varying components of the Jovian background magnetic field. If the dipole were intrinsic, it would either not vary noticeably with time, or would not vary with the same period as Jupiter's (and therefore the Jovian magnetic dipole's) period of rotation.

The presence of an induced magnetic dipole being generated within Europa is significant, because it necessitates the existence of a highly conducting material near the surface of the moon. Zimmer et al. (2000) calculated a minimum conductivity of 0.060 S/m, Schilling et al. (2007) found a minimum conductivity of 0.5 S/m, Khurana et al. (2009) assumed 2.7 S/m, and Paranicas et al. (1998) derived a minimum value of 8 S/m, while Hand and Chyba (2007) estimated that chemical fluxes from the surface ice into the ocean would result in salinity comparable to that of Earth's oceans within 50 Myr. As most cryocrystals (ices), particularly water ice which composes almost all of the Europan surface, have a conductivity far below this value, a solidly frozen body of ice cannot explain the presence of the induced dipole observed at Europa. It is therefore expected that a saline water ocean exists below the surface of Europa.

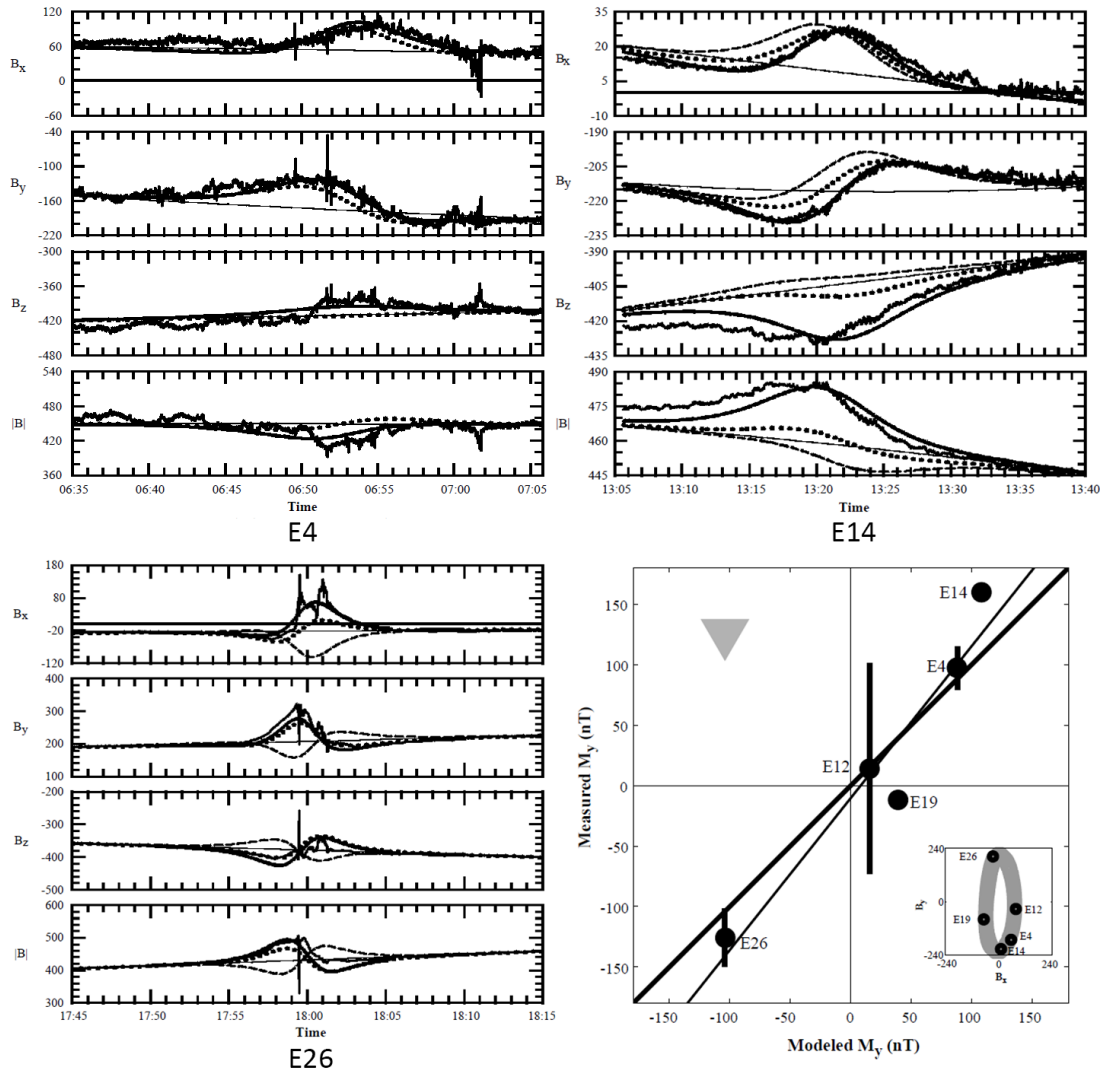

Figure 3.5: Plots of magnetic field values measured by the Galileo magnetometer overlaid with fitted background field values and values from an induced dipole field for Galileo flybys E4 (Top Left), E14 (Top Right), and E26 (Bottom Left). (Bottom Right) Equatorial dipole moments fitted to data (thin line) are also compared to predictions for a highly conducting sphere (thick line) Kivelson et al. (2000).

3.3.2 Variation with Location

The strength and direction of the induced dipole generated with this putative subsurface ocean varies depending on the time-varying component of the Jovian background magnetic field near Europa. As has been previously mentioned, variations in the background field are dominated by changes to the radial and corotational components of the magnetic field and are caused by the tilt of the Jovian magnetic dipole relative to Jupiter's axis of rotation. It is therefore useful to define how these components tend to vary between different locations that Europa can occupy within the Jovian magnetosphere (Volwerk et al., 2001; Zimmer et al., 2000; Kivelson et al., 2000). Figures 3.6 and 3.7 show these locations, where A is below the Jovian plasma sheet, C is above the Jovian plasma sheet, and both B and D are within the Jovian plasma sheet. Note, however, that while both B and D are within the plasma sheet, the corotational component of the Jovian background magnetic field is pointing in different directions in each. In B, it is directed in the anti-corotational direction, while in D it is parallel to the direction of corotation. The corotational component of the background magnetic field is smaller in magnitude when Europa is either above or below the plasma sheet. The magnitude of the radial component of the background field varies greatly, reaching $\sim$50% of the spin-aligned component in locations A and C, and being roughly 0 nT when Europa is within the center of the Jovian plasma sheet.

In addition to these components which vary over the time period of Jupiter's rotation, there is an additional component that changes with the period of Europa's orbit around Jupiter (85 hours). This is driven by the eccentricity of Europa's orbit around Jupiter. At perijove, Europa is $\sim$665,000 km from the center of Jupiter, and at apojove Europa is $\sim$677,000

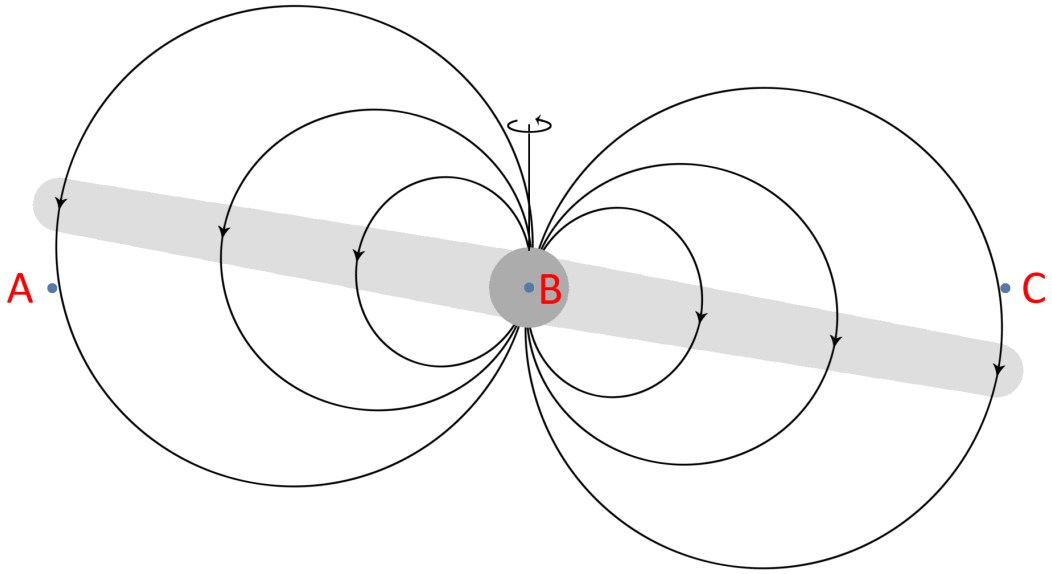

Figure 3.6: Side view of Europa's location within the Jovian magnetosphere at different times. Jupiter is at center of diagram with the spin axis indicated above. Blue circles represent Europa. Tilted, light gray line indicates plasma disk. Black lines are magnetic field lines. Sun is always in the direction opposite to the bulk flow velocity of corotating JMP (into page at location A, to the left at location B, etc.)

km away. This creates a small variation in the Z (spin-aligned) component of the the background magnetic field. While it is harder to measure, the induced response to the variation of this component of the Jovian background magnetic field with time is important, as its longer wavelength allows for the depth of the ocean below the Europan surface to be determined.

By combining the induced response to the short period variations in the Jovian background magnetic field with the long period response, it should be possible to constrain the distance of the ocean below the surface, the salinity of the ocean, and the depth of the ocean. In this way, measuring the variation of the Europan dipole moment can act as the most powerful diagnostic tool for characterizing the depths of Europa that is available.

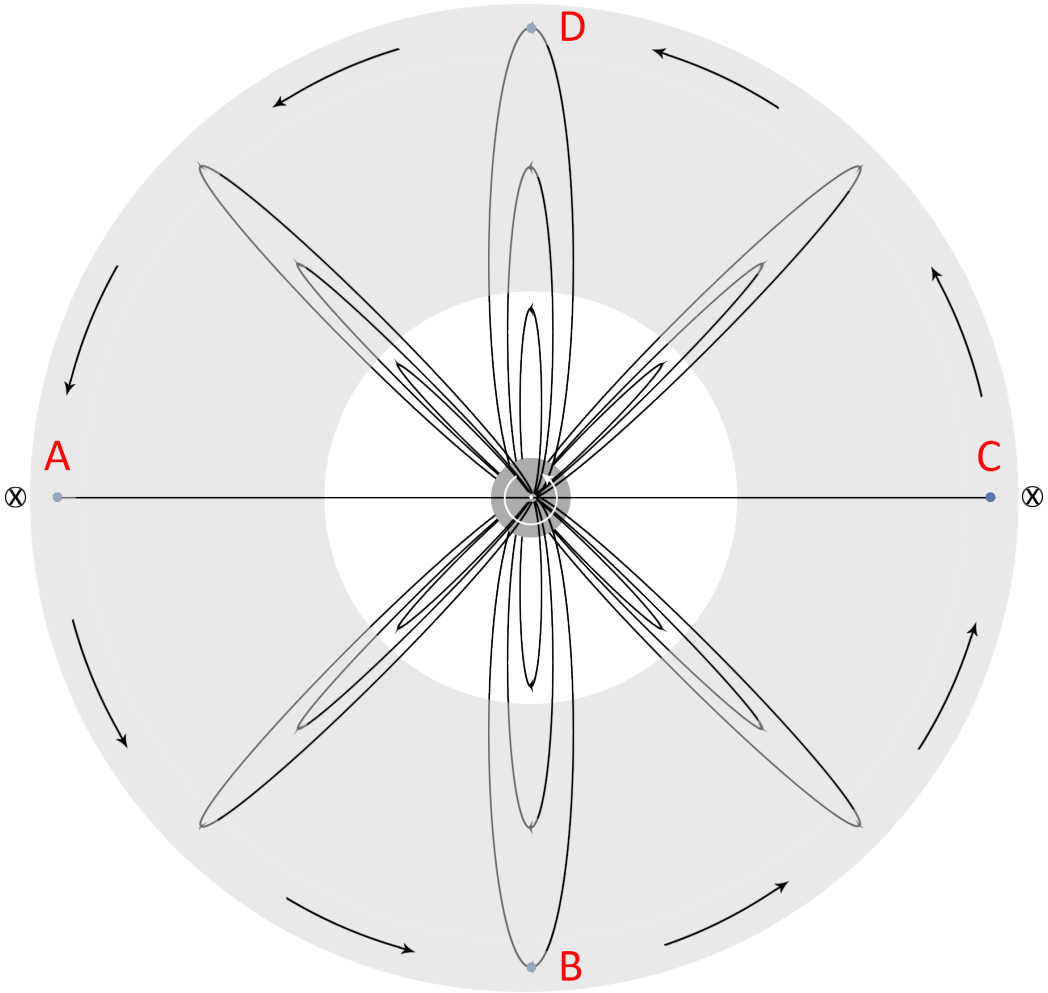

Figure 3.7: Overhead view of Europa's location within the Jovian magnetosphere at different times. Jupiter is at center of diagram with the spin axis superimposed. Blue circles represent Europa. Tilted, light gray torus indicates plasma disk with flow direction indicated by black arrows. Black lines are magnetic field lines. Sun is always in the direction opposite to the bulk flow velocity of corotating JMP.

3.4 Europa Clipper Mission

The Europa Clipper mission is a NASA mission currently under development for launch in the early to mid 2020's. The goal of the Europa Clipper is to determine the potential habitability of Europa by performing a large number of flybys of the moon. This is in contrast to previous mission plans for the exploration of Europa, which called for a spacecraft to enter into orbit around the body and take measurements from there. Through careful trajectory planning, near global coverage of the surface of the moon with the remote sensing instruments planned to be included on the mission can be achieved. It is therefore believed that as much or more data can be gathered about Europa by performing flybys than by entering into orbit. An initial plan for flybys to be performed during the Europa Clipper's primary mission phase can be seen in Figure 3.8.

This mission design was chosen because of the intense radiation environment in the vicinity of Europa which is harmful to spacecraft systems (Truscott et al., 2011). A mission in orbit around Europa would likely only be able to survive for around one month before its systems were compromised by radiation exposure. This time limit would make it so that only $\sim$8 orbits of Europa around Jupiter could be observed. The fact that the component of the Europan induced dipole that can reveal the depth of the ocean depends on Europa moving between perijove and apojove (as was mentioned in Subsection 3.3.2) means that this could impair the mission's ability to thoroughly characterize the ocean's dimensions. The large distance between Earth and Jupiter also restricts data transmission rates, demanding a powerful transmitter if all of the mission's data were to be returned to Earth within one month. By staying in orbit around Jupiter rather than Europa, the Europa Clipper can

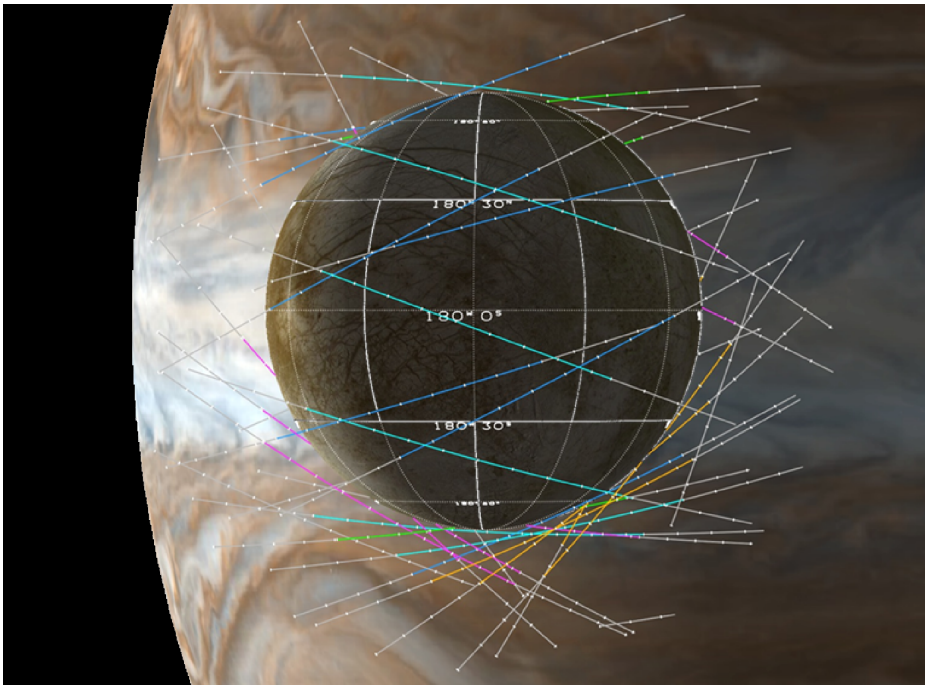

Figure 3.8: Notional spatial distribution of EC flybys from “Europa Study 2012 Report”.

spend relatively little time within the high radiation environment near Europa and transmit its data back to Earth during the period between flybys of Europa.

The Europa Clipper will carry two instruments that are directly relevant to understanding the plasma environment near Europa: ICEMAG and PIMS. ICEMAG is a magnetometer which will measure the strength, direction, and gradient of the magnetic field near Europa and PIMS will measure the plasma population near Europa (Westlake et al., 2016). ICEMAG will allow for the strength and orientation of the induced magnetic dipole within Europa to be determined (Raymond et al., 2015), while PIMS will allow for distortions in the magnetic field caused by the presence of varying plasma populations to be accounted for, which is necessary in order for the signature of the Europan magnetic dipole to be accurately measured by ICEMAG. Figures A.3 and A.4 show diagrams of the instruments. In addition to these instruments, modeling by Johnson et al. (1998) suggests that levels of or-

ganic molecules and salts could be high enough in the Europan exosphere for the MASPEX Waite Jr et al. (2015) mass spectrometer instrument – also planned to be launched on the Europa Clipper – to detect them. Furthermore, work by J. F. Cooper et al. (2001) indicates that energetic particle bombardment of the Europan surface can produce both simple and complex organic molecules through interactions with non-ice elements already present within the Europan ice.

CHAPTER 4

THE ICY BODIES MODEL

4.1 Modeling the Pluto-Charon System

4.1.1 Previous Modeling Efforts

Largely because of the lack of available data, few modeling efforts had been undertaken in the Pluto system before those that are described here. That being said, it is instructive to briefly go over them in order to provide context for what we have done in the present work. Sauer et al. (1997) were the first to perform modeling of the interaction between Pluto and the solar wind. Using two dimensional bi-ion fluid and hybrid simulations, they concluded that Pluto was likely to behave like a weak comet. This was a common perception at the time, with Bagenal and Ralph L. McNutt (1989) also deciding that a comet-like interaction was likely, albeit based on analysis rather than simulation. Both concluded that a single ion treatment was unlikely to be able to accurately model the system.

The next modeling work to be published on the topic was by Delamere and Bagenal (2004). This was the first work to be done with a fully three dimensional model, deploying a hybrid model in which ions were treated as particles and electrons were treated as a massless fluid. Also of note, is that this simulation assumed a charge ratio of 10 Da/q, due to computation limitations. Various atmospheric outflow rates were simulated. The authors determined that Pluto's interaction with the solar wind could be anywhere between a Venus-like interaction and a comet-like interaction. They also concluded that in the Venus-like instance, a bow shock could form upstream of Pluto, and that the wake behind Pluto would be highly

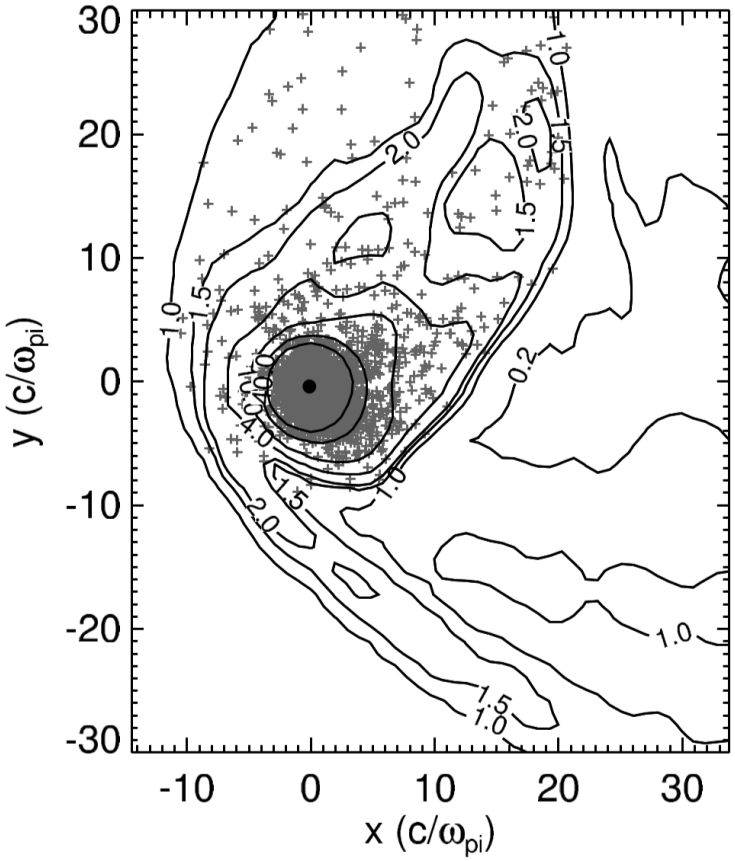

Figure 4.1: Total ion density near Pluto from (Delamere and Bagenal, 2004). Distances measured in solar wind ion inertial lengths ($\sim$2 R_P). Selected heavy pickup ions are indicated by pluses, while solar wind density is indicated by isolines. IMF is out of plane.

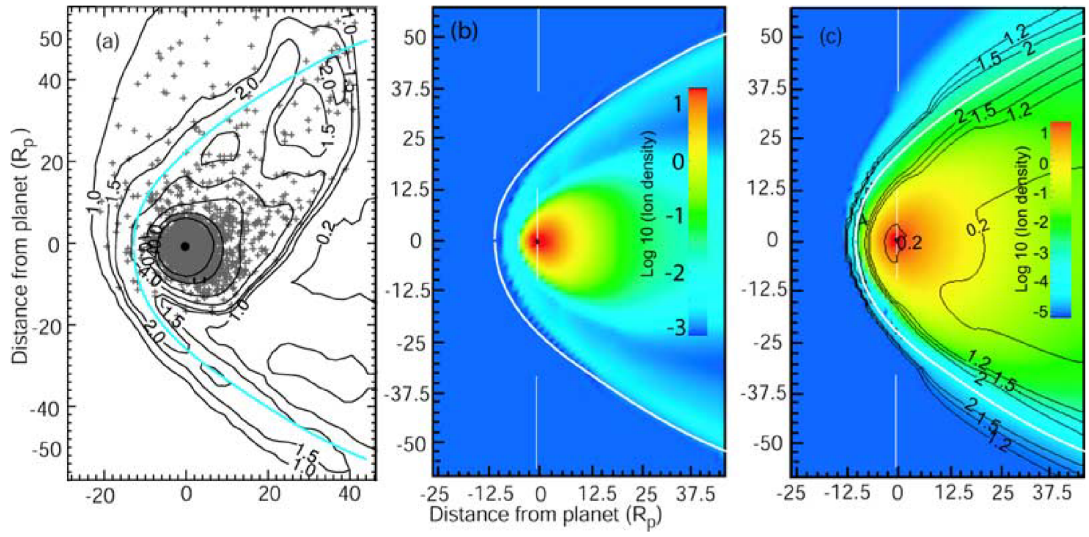

Figure 4.2: (Left) Total ion density and heavy pick up ions using a hybrid method, (Center) total ion density using an ideal MHD method, and (Right) total ion density and solar wind density contours using a multifluid MHD method. (Harnett et al., 2005).

structured regardless of the type of interaction. Figure 4.1 shows total ion density near Pluto along with select heavy pickup ion macro-particles.

Harnett et al. (2005) followed this work with a comparison to assess the utility of a multifluid MHD treatment for the system. In order to carry this comparison out, they performed ideal MHD and multifluid MHD simulations using the same parameters as those used by Delamere and Bagenal (2004) and then performed direct comparisons between the different results. Figure 4.2 shows plots of this comparison. They concluded that, as had been widely believed, an ideal MHD model was not able to capture significant elements of the interaction, but also that the multifluid MHD treatment shared qualitative ion-cyclotron features with the hybrid treatment, such as asymmetries between flows of solar wind protons and heavy pickup ions. Harnett et al. (2005) then went further and performed a parameter space exploration using the multifluid MHD model in order to assess how the system behaved under different scenarios. Results using different system parameters can been seen

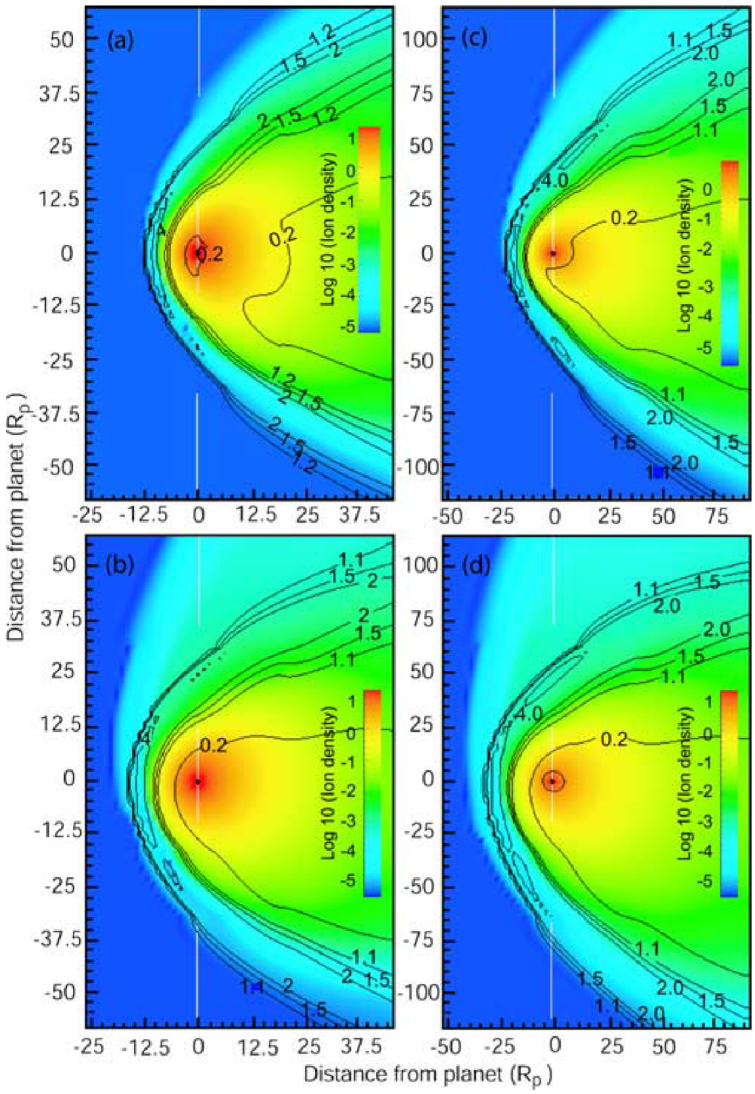

Figure 4.3: Cases A and B have a solar wind number density of 0.01 cm^{-3} and speed of 450 km s^{-1} versus 0.0025 cm^{-3} and 900 km s^{-1} for cases C and D. Cases A and C use a pickup ion mass per charge of 10 Da/q versus 28 Da/q for cases B and D (Harnett et al., 2005).

in Figure 4.3. It is readily apparent that in the cases which use heavier pickup ions, with a ratio of 28 Da/q the gyroradius of the ions being picked up is much greater. As similar, but less pronounced effect is seen for the cases which used a faster solar wind speed compared to those with a more typical solar wind velocity.

Several years later, Delamere (2009) continued his previous work, this time using a mass of 28 Da/q, as a result of advances in computing power in the preceding five years. Some of the analysis focused on the structured wake region that was noted previously. This included the notable role that Kelvin-Helmholtz instabilities played on the interface between the wake region of the interaction and the region of free stream flow. All cases that were simulated assumed an atmospheric escape rate of at least 10^{26} N_2 s^{-1}, $\sim$1000$\times$ the estimated rate by Gladstone et al. (2016) using New Horizons data. Figure 4.4 shows simulations performed using an escape rate of $2 \cdot 10^{27}$ N_2 s^{-1}. A strong role for asymmetries between the flow of solar wind protons and heavy pickup ions in the plane perpendicular to the IMF was again found. This was the last work on the topic to be published before the investigations discussed here were begun.

None of the previous work on this topic has considered the presence of Charon within the system. Bagenal and Ralph L. McNutt (1989) speculated that Charon might create a cavity in the solar wind flow in its wake and Sauer et al. (1997) speculated that it might be possible that Charon might pass within Pluto's interaction region over the course of its orbit, but not simulations had been carried out to study the topic further. In contrast, this work is concerned with Charon's effects on the Plutonian interaction with the solar wind, with particular emphasis placed on any impact that Charon, while upstream of Pluto, may have on the formation of a bow shock in the system. Both system geometry and the

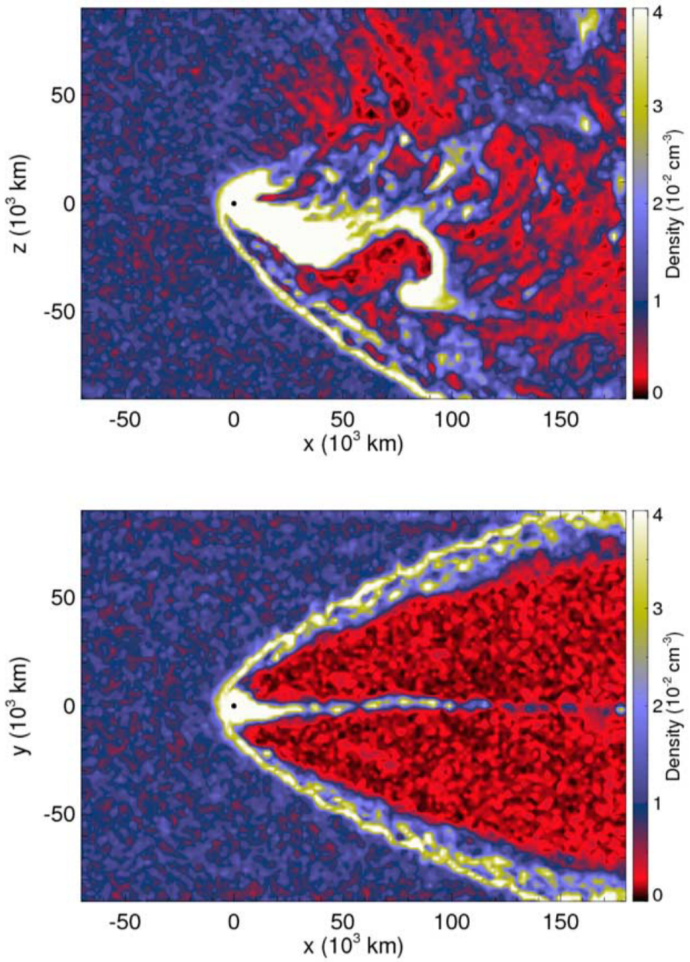

Figure 4.4: Total ion number density in the XY and XZ planes (Delamere, 2009). Note that IMF is now in the Y direction, rather than the Z, as it was in Figure 4.1.

presence of an ionosphere around Charon are considered in different scenarios simulated for the present work.

4.1.2 Pluto-Charon Simulation Parameters

A series of simulations were run in order to characterize the behavior of the system throughout the relevant parameter space. The system input parameters are shown in Table 4.1. These values were chosen in order to simulate what were expected to be typical solar wind and IMF conditions at Pluto, based on available data and modeling. The peak ionospheric number density at Pluto was based on chemical modeling performed by Krasnopolsky and D. Cruikshank (1999), while peak ionospheric density at Charon was chosen to be a small fraction of that at Pluto (3%) on the basis that any transient atmosphere which Charon may possess would be unlikely to be dense relative to Pluto's. The scale height of the imposed ionosphere was chosen in order to produce an interaction region similar in size to previous modeling efforts. Additional cases were simulated using a greatly expanded ionosphere, in keeping with pre-encounter predictions that Pluto would be comet-like in nature. Figures showing results from these simulations can be found in Subsection A.1.

The primary parameters that were varied were the presence and location of Charon with respect to Pluto, as well as the presence of an ionosphere around Charon, as shown in Table 4.2. These configurations were chosen in order to test the extremes of possible values for system parameters, as well as to generate a baseline for comparison in the instance of case P.1.1. For context, Charon had no detectable ionosphere (Gladstone et al., 2016) and was to the side and slightly downstream of Pluto at the time of the New Horizons encounter. It was predicted that case P.1.5 would exhibit the most extreme alteration due to

Table 4.1: Plasma parameters used for solar wind, Pluto, and Charon. *Temperatures are incorporated through the state equation. **Peak ion density for the Charon sourced species is not set to exactly 0 cm^{-3} due to numerical constraints.

Parameter	Value(s) Used
Magnetic Field (nT)	0.2 (Bagenal et al., 1997)
Solar Wind Speed (km/s)	380 (Bagenal et al., 2015b)
Solar Wind Density (H^+cm^{-3})	0.01 (Bagenal et al., 1997)
Solar Wind Temperature (K)*	9000 (Richardson and C. W. Smith, 2003)
Pluto Species Mass (Da/q)	28 (Krasnopolsky and D. Cruikshank, 1999)
Pluto Peak Ion Density (cm^{-3})	750 (Krasnopolsky and D. Cruikshank, 1999)
Pluto Ion Temperature (K)*	130 (Sicardy et al., 2003)
Charon Species Mass (Da/q)	28
Charon Peak Ion Density (cm^{-3})	25, $\sim$0**
Charon Ion Temperature (K)*	40

Table 4.2: Simulations performed. All cases were run for 1500 s of simulated time in order to allow for a quasi-steady-state to be reached.

Charon Absent	(P.1.1)	
Charon without Ionosphere	Charon Downstream (P.1.2)	Charon Upstream (P.1.4)
Charon with Ionosphere	Charon Downstream (P.1.3)	Charon Upstream (P.1.5)

the presence of Charon within the system.

For the follow up work on Pluto, two cases were carried out in order to assess the validity of newly implemented neutral particle interactions within the model, to see how the model would perform with the atmospheric and plasma parameters that were observed by New Horizons during its flyby of the system, and to see how realistic the ionospheric profiles that we generated for the model before the New Horizons encounter were by comparing their results with those using the same solar wind conditions as previously modeled, but with a neutral atmospheric profile created by Gladstone et al. (2016) based on Alice UV occultation data. The plasma parameters used for these simulations, cases P.2.1 and P.2.2, are shown in Table 4.3. The radius of Pluto was also altered slightly from 1187 km (Stern et al., 2015b), which was used for the initial set of simulations, to 1188 km as a result of

Table 4.3: NH based plasma parameters used for solar wind and Pluto in follow up work with ion-neutral interactions P.2.2. P.2.1 used same parameters as P.1.1 where applicable. *Temperatures are incorporated through the state equation.

Parameter	Value(s) Used
Magnetic Field (nT)	0.2 (Bagenal et al., 1997)
Solar Wind Speed (km/s)	380 (Bagenal et al., 2016)
Solar Wind Density (H^+cm^{-3})	0.025 (Bagenal et al., 2016)
Solar Wind Temperature (K)*	9000 (Richardson and C. W. Smith, 2003)
Pluto Species Mass (Da/q)	16 (CH_4) (Bagenal et al., 2016)

analysis by Nimmo et al. (2017) of New Horizons data (Charon's measured radius remained at 606 km).

4.2 Modeling Europa's Plasma Interaction

4.2.1 Previous Modeling Efforts

Unlike Pluto, Europa has been the subject of relatively extensive modeling work for an icy world. The techniques used for these studies have ranged from single fluid MHD to multi-fluid MHD to hybrid kinetic. Much of this work has been focused on trying to simulate the conditions that existed during specific flybys of Europa by the Galileo spacecraft – most prominently the E4 flyby – in order to match see how effectively they have reproduced instrument measurements, including the magnetic induction signal of the Europan subsurface ocean.

Notable work done with MHD models include those by Saur et al. (1998), Kabin et al. (1999), Liu et al. (2000), Schilling et al. (2008), and Blöcker et al. (2016). Saur et al. (1998) performed a study attempting to match HST observations of emissions from the Europan exosphere, carried out with a two fluid model which assumed a constant background

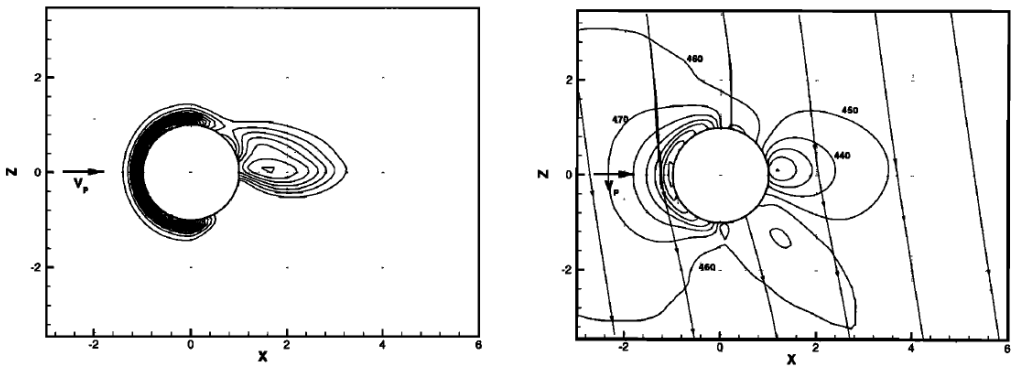

Figure 4.5: The left panel shows incident particle density contours (the outermost contour corresponds to 40 cm$^{-}3$) and right panel shows magnetic field direction and magnetic field strength contours around Europa. Single fluid MHD simulation using Galileo E4 flyby plasma parameters (Kabin et al., 1999).

magnetic field. Figure 4.5 shows results from Kabin et al. (1999) using an ideal MHD approach to model the E4 flyby in order to attempt to replicate the observed induction signal reported by Khurana et al. (1998). A modified version of the same model was then used by Liu et al. (2000) to again attempt to match observations made during the E4 flyby, with the model having been enhanced to use a two-species ideal MHD approach. More recently, Schilling et al. (2008) used a single fluid MHD model coupled with an internal induction model in order to try to match the signal observed during the E4 flyby. Blöcker et al. (2016) employed a single fluid MHD model to explore the effects of inhomogeneities in the neutral density on the plasma interaction and compare their results against several flybys, including the E26 flyby.

A pair of studies of the system have been performed by Lipatov et al. Their first study, Lipatov et al. (2010) used a hybrid kinetic model in combination with the a neutral exospheric distribution based on Cassidy et al. (2007) to try to match the E4 flyby observations with somewhat mixed results, possibly due to issues with the resolution of the simulation near

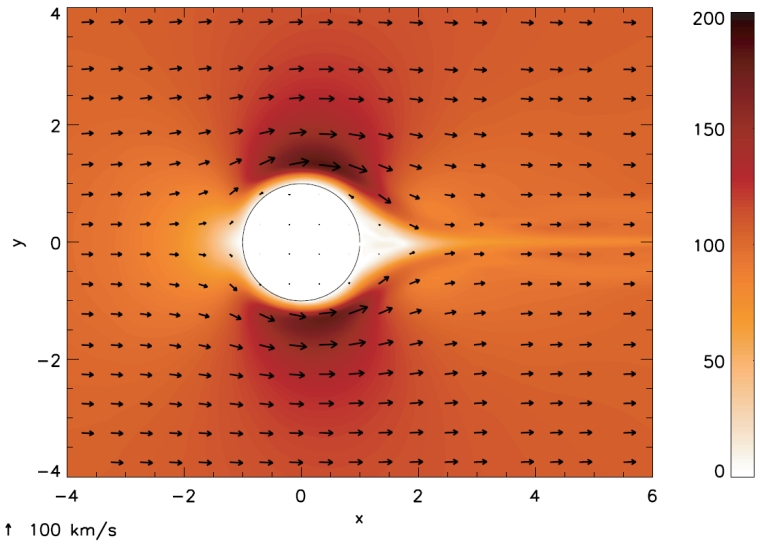

Figure 4.6: JMP velocity vector field and magnitude showing Alfvén wing structure (wings are perpendicular to page). Single fluid MHD simulation using Galileo E4 flyby plasma parameters (Schilling et al., 2008).

to the surface of the body. They are, however, able to produce Alfvén wings, as can be seen in Figure 4.7. Their follow up work, Lipatov et al. (2013), had similar issues, but was able to better match observed magnetic field measurements.

More recent work by Rubin et al. (2015) used a multifluid MHD approach to perform an extensive analysis in which they compare model results against measurements from the E4 and E26 flybys. They are able to match the magnetic signature of the the induction response very well for both flybys. Figure 4.8 shows their O^+ and O_2^+ density plots for the E26 flyby, with the spacecraft trajectory overlaid on the plots. They state that the model will able to accommodate the simulation of the induced dipole field through modeling of the conductive components of the Europan interior, but defer implementation of this possibility to future work on the topic.

As can be seen, the existing body of modeling work having to do with Europa puts significant focus on reproducing measurements from a couple of flybys from the Galileo mission.

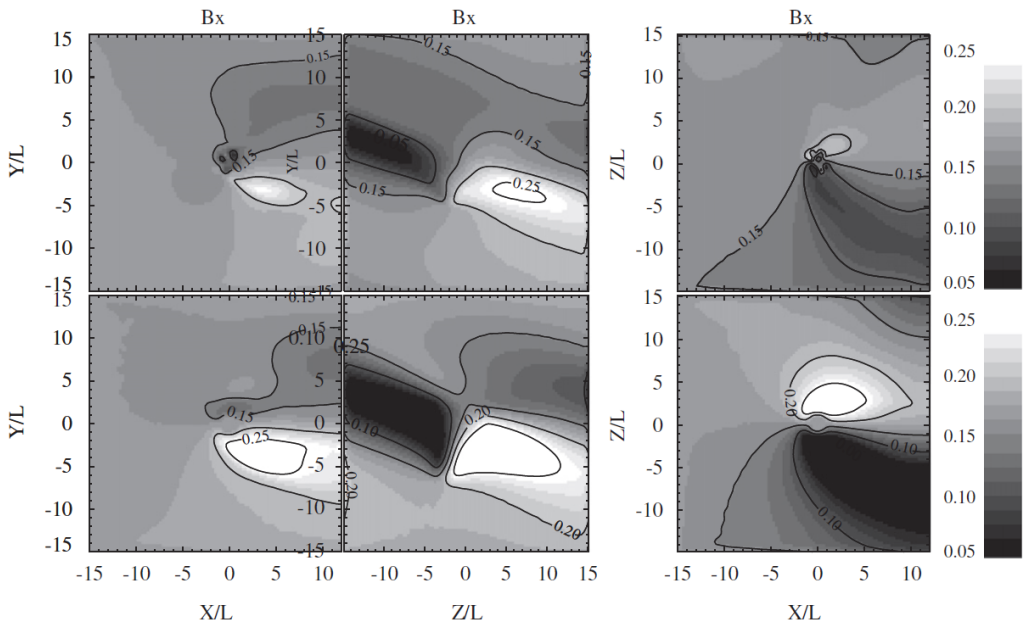

Figure 4.7: Alfvén wings shown in B_x for two different upstream conditions. Simulated by Lipatov et al. (2010) using a hybrid model.

This has much to do with the fact that the E4 and E26 flybys had relatively simple magnetoplasma parameters and therefore can act as easily analyzed checks of how successfully a model is reflecting the physical processes present in the near-Europa plasma environment. However, it might also have to due with the clear goal of such studies compared to more open-ended investigations.

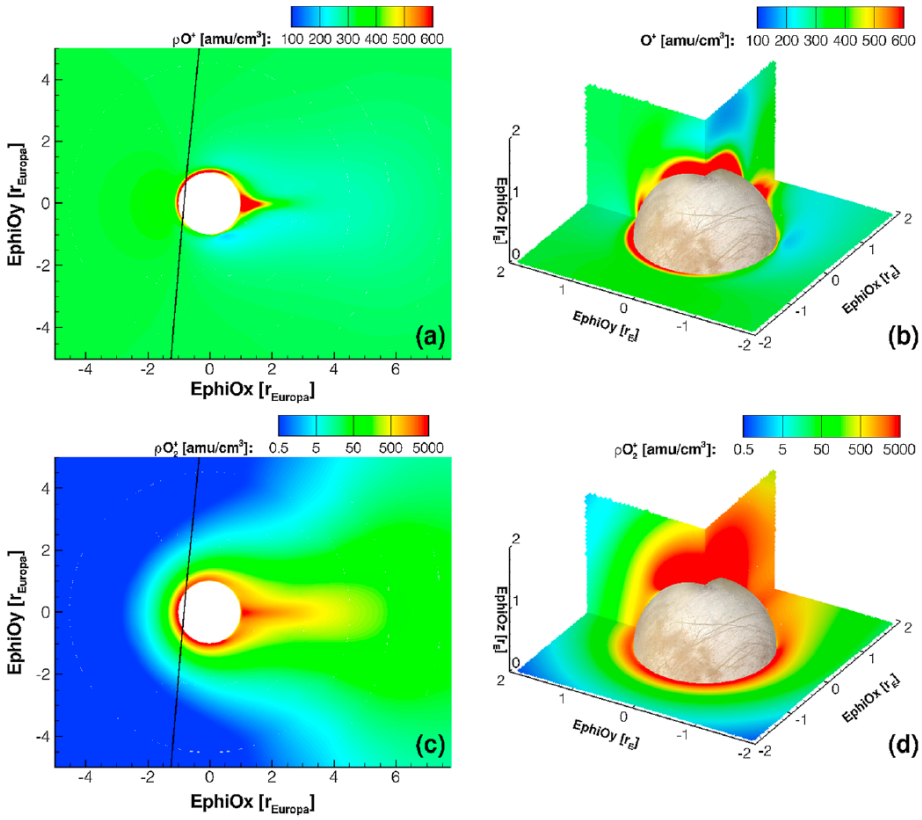

Figure 4.8: JMP and ionospheric density plots with Galileo trajectory overlaid. Simulation performed using E26 flyby plasma parameters by Rubin et al. (2015).

4.2.2 Europa Simulation Parameters

Our investigation of the Europa system involved a series of simulations designed to isolate what role Europa's ionosphere plays in its interaction with the Jovian magnetosphere in anticipation of the Europa Clipper mission now in development. We selected system plasma parameters that were representative of periods when Europa was either inside of or above/below the Jovian plasma sheet. Also, as we explained in Subsection 3.3.2 and showed with Figures 3.6 and 3.7, the strength and orientation of Jupiter's magnetic field can be different even at different locations within the plasma sheet. The parameters that we selected are listed in Table 4.4. While Jovian magnetospheric plasma (JMP) density and the X and Y components of the magnetic field strength varied, the velocity of the JMP within the domain's coordinate system remained the same, as did the fact that the species used was O^+. The temperatures of various components of the JMP were also kept constant. Table 4.5 lists the different cases that we performed simulations of for this investigation. Cases E.1.1 through E.1.4 had no neutral sourced ionosphere around Europa, while E.1.5 through E.1.8 did. The cases were paired so that, for example, E.1.1 and E.1.5 were in the same location within the Jovian magnetosphere. The four locations that were used corresponded to locations A - D shown in Figures 3.6 and 3.7, with location A being above the plasma sheet, B being within it, C being below it, and D being within it, but with the varying component of the background Jovian magnetic field pointed in the opposite direction within the simulation domain.

Table 4.4: Plasma parameters used for Europa plasma environment. *Magnetic field values are derived from measured values during the following Galileo flybys: E11 and E15 (Volwerk et al., 2001), E14 (Zimmer et al., 2000), and E26 (Kivelson et al., 2000). **Temperatures are incorporated through the state equation.

Parameter	Value(s) Used
Magnetic Field X (nT)*	-50 to 50
Magnetic Field Y (nT)*	-200 to 200
Magnetic Field Z (nT)*	-400
JMP Speed (km/s)	84.2 ($v_{\mathrm{corot}} - v_{\mathrm{E}}$)(Bagenal et al., 2015a)
JMP Species Mass (Da/q)	16 (Bagenal et al., 2015a)
JMP Density (cm^{-3})	100 to 150 (Bagenal et al., 2015a)
JMP Temperature (eV)**	130 (Bagenal et al., 2015a)
Europa Species Mass (Da/q)	32
Electron Temperature (eV)	20, 300 (Bagenal et al., 2015a)

Table 4.5: Simulations performed. All cases were run for 750 s of simulated time in order to allow for a quasi-steady-state to be reached.

Position \ Exosphere	No Exosphere	Exosphere
A	(E.1.1) B_x = 20 B_y = 200 ρ_{JMP} = 100	(E.1.5) B_x = 20 B_y = 200 ρ_{JMP} = 100
B	(E.1.2) B_x = -50 B_y = 0 ρ_{JMP} = 150	(E.1.6) B_x = -50 B_y = 0 ρ_{JMP} = 150
C	(E.1.3) B_x = -20 B_y = -200 ρ_{JMP} = 100	(E.1.7) B_x = -20 B_y = -200 ρ_{JMP} = 100
D	(E.1.4) B_x = 50 B_y = 0 ρ_{JMP} = 150	(E.1.8) B_x = 50 B_y = 0 ρ_{JMP} = 150

4.3 Structure of Model

The model that was used in this study is an evolved form of a multifluid treatment that has been applied to numerous planetary bodies in the past. Previously studied bodies include Ganymede (C. Paty and R. Winglee, 2006) and Titan (Snowden et al., 2011), as well as the study at Pluto which compared results from hybrid and multifluid MHD models (Harnett et al., 2005). The model is a global, three-dimensional, fully multifluid, magnetohydrodynamic model, which is appropriate for the Pluto system as the freestream turning distance of solar wind H^+ ($\sim$17 R_P) is smaller than the interaction region (defined as the diameter of the main shock on the plane passing through Pluto's terminator, which is $>$35 R_P under simulated conditions), and the gyroradius of the solar wind H^+ within the shock and wake falls to as low as 1 R_P. It describes plasma behavior using a system of conservation equations, which are solved for each ion species: conservation of mass, conservation of momentum, and the energy equation of state. Electrons are treated as a separate, massless fluid where number density is derived through quasi-neutrality. Magnetic fields, electric fields, and currents are calculated using Maxwell's equations and the generalized Ohm's law. A second order Runge-Kutta method is used to solve each equation at each point on a nested grid.

Figure 4.9 shows a representation of the nested grid structure that was used for simulations of the Pluto-Charon system. There are a total of six grid boxes within the simulation, but only five are shown within the figure. Note that Charon is place within the innermost grid of the simulation domain which has a resolution of $\sim$64 km per grid point, and Pluto is place within the next highest resolution grid, with a resolution of $\sim$128 km per grid point.

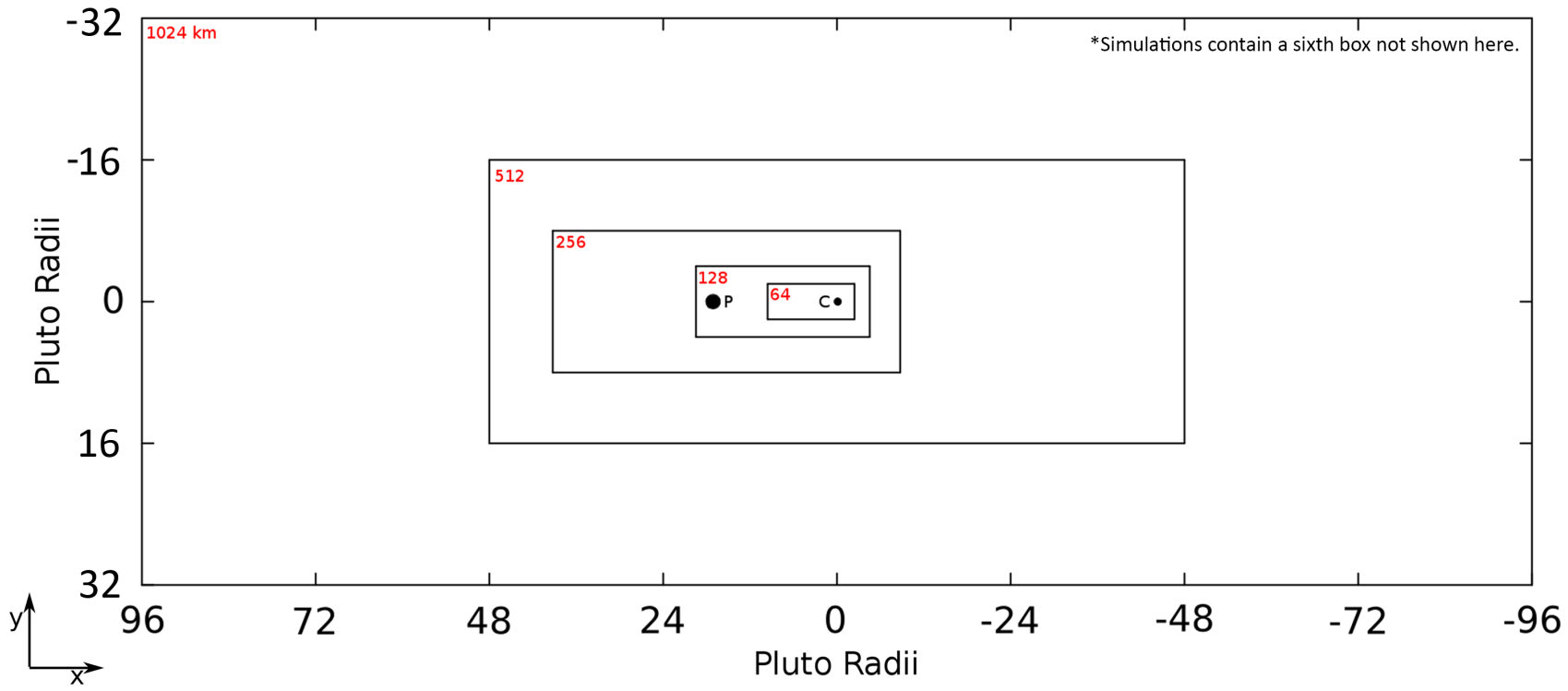

Figure 4.9: Representative gridding pattern used within simulations of the Pluto-Charon system. Configuration shown used in cases P.1.2 and P.1.3. Variations of this pattern were used for other cases. Z dimensions are equal to those in Y.

This was chosen as a result of computational limitations that would have made running the simulation with both bodies placed within the highest resolution grid intractable. Nevertheless, the choice does not have an negative effect on the simulation, as this arrangement allows each body to be simulated at the same resolution in units of km/R_o, or the radius of that body. The total simulation domain is $\sim$384 R_P, or 456,576 km, in length (X) and $\sim$128 R_P, or 152,192 km, in width and height (Y and Z). The exact arrangement of grid boxes changes, depending on the relative locations of Pluto and Charon with the simulation (the configuration shown in the figure was used in cases P.1.2 and P.1.3). Figure 4.10 shows the simulation grid that was used in the Europa simulations that have been performed. Four grid boxes were used in these simulations, with Europa placed within the center of the innermost grid box, with a resolution of $\sim$52 km per grid point. The total simulation domain is 26.8 R_E, or 41,835 km, in length (X) and 24 R_E, or 37,464 km, in width and height (Y and Z). Incident plasma enters the system from the -X direction (for more information, see Section 4.8). The Europa simulations use the EphiO coordinate system, in which X points in the direction of Europa's orbit, Y points towards Jupiter, and Z completes the system.

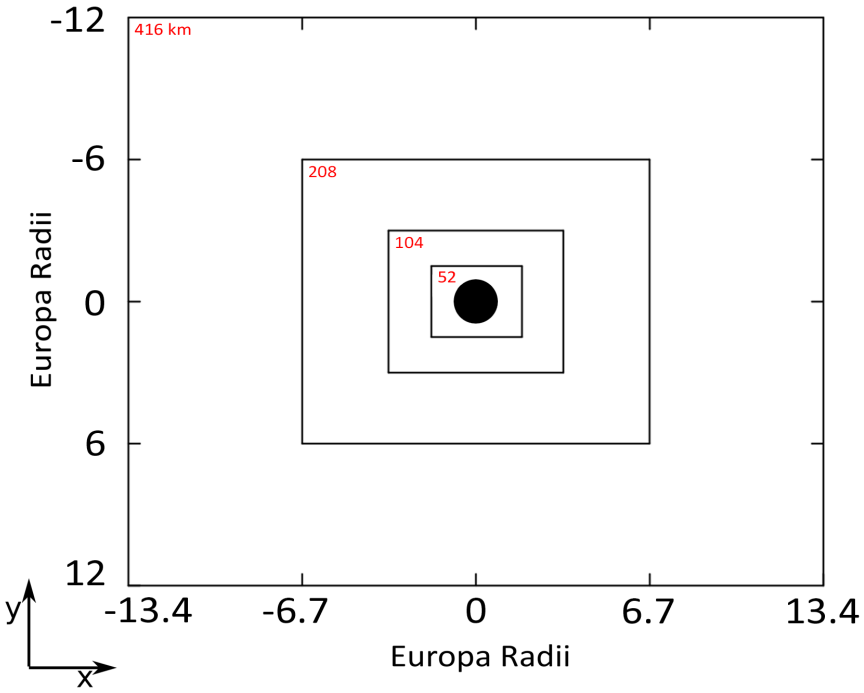

Figure 4.10: The gridding pattern used within simulations of the near Europa environment. Z dimensions are equal to those in Y.

4.4 Governing Equations

In tracking several ion species, the conserved quantities are calculated separately for each ion species; here subscript α denotes the species, and subscript e the electrons, o indicates the planetary body, $\vec{v}$ is ion/electron velocity, P denotes pressure, q is ion charge, m is the mass, n is number density, ρ is mass density, and γ is the ratio of specific heats (set to 1.67 within the model – actual values range between 1.32 for CH_4^+ and 1.67 for O^+ (Haberman and John, 1980)). $\vec{E}$ and $\vec{B}$ are the electric and magnetic fields, respectively, and $\vec{J}$ is the current density.

The conservation of mass (Equation 4.1) (to which source and loss terms have been added, which are discussed in Section 4.5), conservation of momentum (Equation 4.2), and time

dependent pressure from equations of state pressure equations (Equations 4.3 & 4.4) are from the multifluid formulation of C. Paty and R. Winglee (2006), with the addition of heat terms which are described in Subsection 4.5.4. The conservation of momentum equation has been modified to include a summation of gravitational terms, as shown in the first summed term in Equation 4.2, as well as to include changes in momentum due to neutral interactions, as shown in the second summed term. A Coriolis term has not been implemented due to the long period of the Pluto-Charon system.

$$\frac{\partial \rho_\alpha}{\partial t} + \nabla \cdot (\rho_\alpha \vec{v}_\alpha) = S_\alpha - L_\alpha \tag{4.1}$$

$$\begin{aligned} \rho_\alpha \frac{d\vec{v}_\alpha}{dt} = n_\alpha q_\alpha (\vec{E} + \vec{v}_\alpha \times \vec{B}) - \nabla P_\alpha - \sum_o \Big(\frac{\mathrm{G} M_o}{R_o^2} \Big) \rho_\alpha \hat{r}_o \\ + \sum_n \left\{ \rho_\alpha v_{\alpha_{\mathrm{inc}}} n_{\alpha_{\mathrm{inc}}} \sigma_{\mathrm{ce}} (\vec{v}_n - \vec{v}_\alpha) + \vec{v}_n S_\alpha \right\} \end{aligned} \tag{4.2}$$

$$\frac{\partial P_\alpha}{\partial t} = -\gamma \nabla \cdot (P_\alpha \vec{v}_\alpha) + (\gamma - 1) \vec{v}_\alpha \cdot \nabla P_\alpha + \sum_n Q_{\mathrm{in},\alpha} \tag{4.3}$$

$$\frac{\partial P_e}{\partial t} = -\gamma \nabla \cdot (P_e \vec{v}_e) + (\gamma - 1) \vec{v}_e \cdot \nabla P_e + \sum_n Q_{\mathrm{en}} \tag{4.4}$$

where M_o refers to the mass of the body in question and R_o refers to the distance between the particle and that body. An electron momentum equation, similar in form to Equation 4.2, can be solved for the electric field in the limit where $\frac{d\vec{v}_e}{dt}$ is small – a reasonable assumption given the ion cyclotron timescales present in these simulation (5–50 s for the Pluto simulations and $\sim$0.5 s for the Europa simulations) – and the gravity term is

neglected in order to obtain a generalized Ohm's law. Since there are no large scale and rapidly changing electric fields we can assume a negligible displacement current, hence the plasma current, $\vec{J}$, can be described simply by:

$$\vec{v}_e = \sum_\alpha \frac{n_\alpha}{n_e}\vec{v}_\alpha - \frac{\vec{J}}{en_e} \tag{4.5}$$

$$\vec{J} = e\Big(\sum_\alpha n_\alpha \vec{v}_e - n_e\vec{v}_e\Big) \tag{4.6}$$

Equation 4.5 can be solved for the electron velocity, $\vec{v}_e$, and substituted into Ohm's law to obtain a relationship independent of electron velocity (Equation 4.7).

$$\vec{E} = -\sum_\alpha \frac{n_\alpha \vec{v}_\alpha \times \vec{B}}{n_e} + \frac{\vec{J}\times\vec{B}}{en_e} - \frac{\nabla P_e}{en_e} + \eta(\vec{r})\vec{J} \tag{4.7}$$

Here the resistivity, η, is prescribed only near the base of the ionosphere of each object ($\sim 10^3$ ohm-meters); everywhere else in the simulation it is assumed to be zero. The changes in the magnetic field are determined by the induction equation (Equation 4.8), which are then used with Ampère's Law (Equation 4.9) to find the associated currents.

$$\frac{\partial \vec{B}}{\partial t} = -\nabla \times \vec{E} \tag{4.8}$$

$$\vec{J} = \frac{1}{\mu_0}\nabla \times \vec{B} \tag{4.9}$$

These equations are solved explicitly at each grid point in a nested grid with second or-

der accuracy. Any ions that impact the surface of the bodies are assumed to be lost to the system. See Section 4.8 for more information on the inner boundary. Ionospheric constituents for the initial investigation of the Pluto-Charon system were initialized based on a Chapman profile for the 1/28 q/Da group derived from the chemical modeling done by Krasnopolsky and D. Cruikshank (1999) using the parameters given in Table 4.1, combined with N_2^+ ionized in situ in the extended atmosphere. These populations are treated as one species, hereafter referred to as either Pluto sourced 28^+ or Charon sourced 28^+. The follow up work done on Pluto with neutral interactions included, substituted CH_4^+ for 28^+, as was shown in Table 4.3. Only two fluids are used in the Europa simulations, O^+, the dominant species of the Jovian plasma sheet at Europa's orbital distance, and O_2^+ resulting from interactions with Europa's O_2 exosphere.

A multifluid treatment is useful for this system as it allows for tracking of separate ion species. This is necessary as scenarios are considered in which Charon acts as a distinct ion source within the system. Additionally, the multifluid treatment is able to capture asymmetries within bow shocks that result from gyromotion of heavy pick up ions sourced from Pluto or Charon due to the inclusion of the generalized Ohm's law. As Figure 4.11 shows, multifluid MHD treatments are also able to replicate gyromotion of heavy pickup ions, even when the interaction region is smaller than the gyroradius of the the heavy pickup ions. The three fluid species used in the Pluto portion of the work described in this document are a solar wind H^+ species, a Pluto sourced 28^+ species, and – in cases P.1.3 and P.1.5 – a Charon sourced 28^+ species.

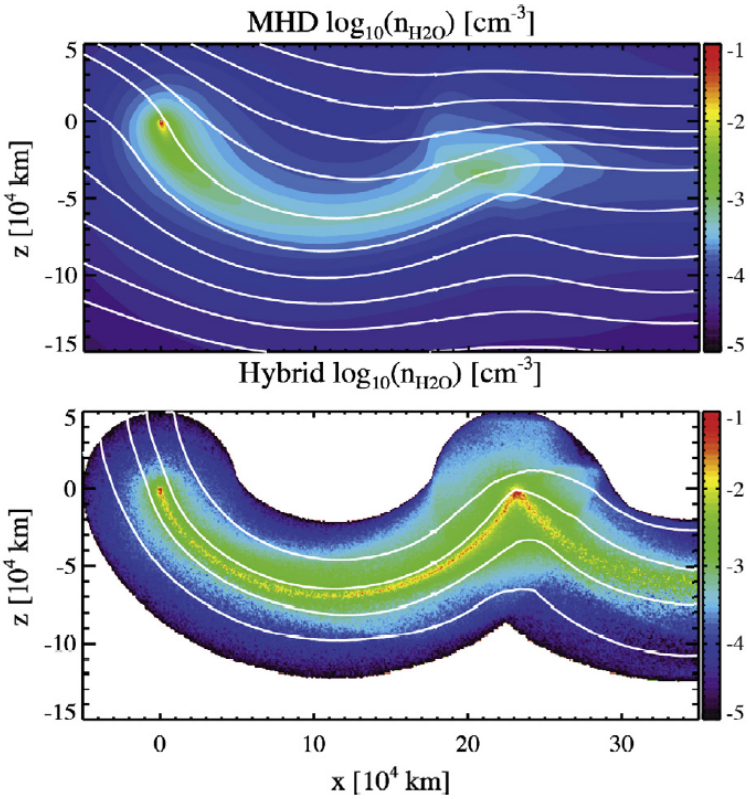

Figure 4.11: Comparison of heavy pickup ion number density near comet 67P/Churyumov–Gerasimenko in a multifluid MHD model and a hybrid model from Rubin et al. (2014). IMF in the Y direction. $\vec{B}$ is into the page.

4.5 Neutral Particle Interactions

Three major mechanisms for the addition or loss of mass, momentum, or energy from fluids have been implemented within the model for these investigations. They consist of electron impact ionization, in which energetic electrons strike neutral particles and eject electrons in the process; photoionization, in which energetic photons – often in the EUV – excite electrons to their ionization energy; and ion-neutral charge exchange, in which an ion's electron shell comes in contact with that of a neutral particle and an electron is transfered to the ion from the neutral particle. Equation 4.10 represents the ion creation rate for an ion species as a result of all of these mechanisms and is a term in Equations 4.1 and 4.2.

$$S_\alpha = \left(\frac{\partial \rho_\alpha}{\partial t}\right)_{\mathrm{e}} + \left(\frac{\partial \rho_\alpha}{\partial t}\right)_{\mathrm{ph}} + \left(\frac{\partial \rho_\alpha}{\partial t}\right)_{\mathrm{ce}} \tag{4.10}$$

In order to simulate the ion production rate from a given neutral particle interaction, it is necessary to know the likelihood that the two particles in question are going to interact with each other. This value is expressed as a cross section and, when combined with other values which will be described in the following sections, gives the ion production rate.

Pluto's Atmospheric Profile

For cases that were run with the Icy Bodies Model at Pluto, the neutral atmospheric profile was assumed to be hemispherically symmetric and was derived from a fit of the neutral density profile for CH_4 created by Gladstone et al. (2016) based on UV occultation data gathered by the New Horizons spacecraft during its encounter with the Pluto-Charon system. Equation 4.11 gives the radial number density profile for CH_4 as implemented within

the model, where R is the radial distance from the center of Pluto.

$$n(R) = 10^{22}\big(R - \mathrm{R_P}\big)^{-4.398} \tag{4.11}$$

Europa's Exospheric Profile

Deciding on an appropriate representation of Europa's exosphere to implement within the model was more difficult due to the complex nature of its generation and the absence of comprehensive observational coverage, as discussed in Section 3.2. After carrying out a survey of the literature, we determined that attempting to reproduce regional effects such as those reported in Cassidy et al. (2007) would be unlikely to produce a meaning improvement to the fidelity of the simulation. This is due to both the lack of a reliable mapping between surface features and exospheric density and the relatively coarse gridding used within the simulation (compared to the size of the regional features thought to affect exospheric distribution).

$$n_{Leading}(R) = n_0 \exp\left(-\frac{|R - \mathrm{R_E}|}{H_0}\right) + n_1 \exp\left(-\frac{|R - \mathrm{R_E}|}{H_1}\right) \tag{4.12}$$

$$n_{Trailing}(R) = n_{Leading}\big(1 + 2\cos(\alpha)\big) \tag{4.13}$$

We therefore decided to use the comparatively simple exospheric O_2 number density distribution developed by Rubin et al. (2015), which is the summation of Equations 4.12 and 4.13, in which $H_0 = 20$ km, $n_0 = 5 \cdot 10^8$ cm^{-3}, $\mathrm{R_E}$ is the radius of Europa, $H_0 = 500$ km, $n_1 = 5 \cdot 10^4$ cm^{-3}, and α is the angle made with the upstream flow direction. The

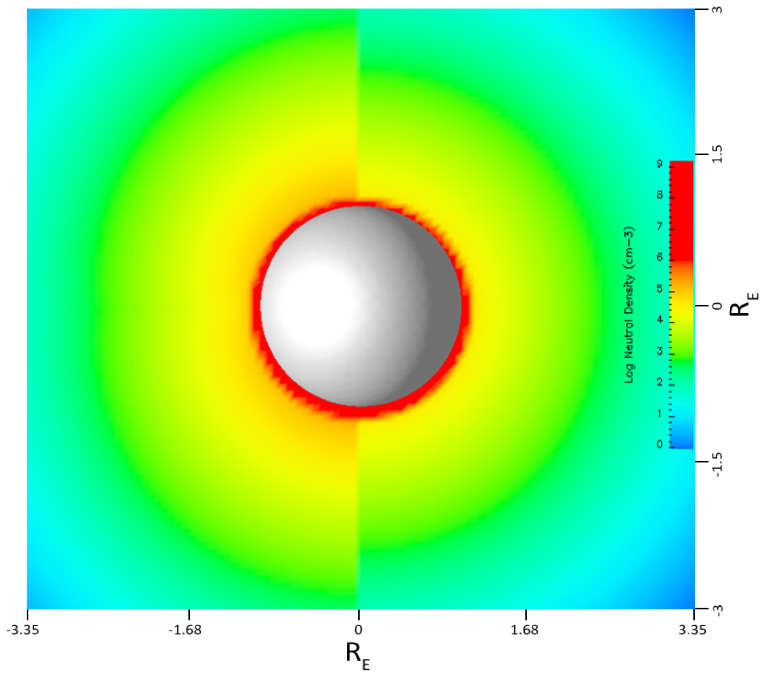

Figure 4.12: The distribution of Europa's exosphere as implemented within the Icy Bodies Model, from Rubin et al. (2015). Note that falloff continues smoothly beyond region shown and that color bar was chosen to highlight hemispheric asymmetry.

two summed distributions are consistent with Cassidy et al. (2007), and the column density matches well to those reported by Hall et al. (1995). The enhancement added on the trailing hemisphere is consistent with the increased rate of sputtering that results from Europa being overtaken by corotational JMP. Figure 4.12 shows the distribution as implemented within the model. The use of this distribution has the added benefit of easing future comparisons between simulation results.

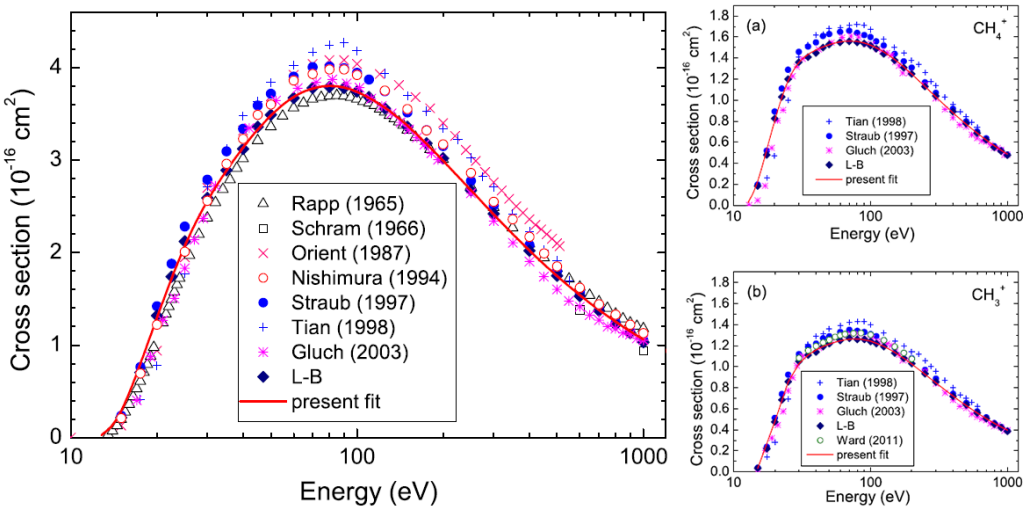

Figure 4.13: (Left) Plot of gross total electron impact ionization cross sections for CH_4. (Right) Plots of partial electron impact ionization cross sections CH_4^+ and CH_3^+ from Song et al. (2015).

4.5.1 Electron Impact Ionization

Equation 4.14 give the Icy Bodies Model's implementation of the ion production rate resulting from energetic electrons impacting a body's neutral atmosphere.

$$\left(\frac{\partial \rho_\alpha}{\partial t}\right)_e = m_\alpha n_{n,\alpha} n_e v_e (fr_t \sigma_{\mathrm{e_t}} + fr_h \sigma_{\mathrm{e_h}}) \tag{4.14}$$

The value m_α is the mass of an α ion, $n_{n,\alpha}$ is the number density of neutral particles that can become α ions, n_e is the number density of electrons, v_e is the bulk velocity of the electrons, fr_t is the fraction of electrons that are in the thermal population and fr_h is the fraction that are in the hot population, while $\sigma_{\mathrm{e_t}}$ and $\sigma_{\mathrm{e_h}}$ are the electron impact ionization cross sections for the thermal and hot electron populations, respectively.

For the Pluto-Charon simulations, we used CH_4 cross sections from Song et al. (2015) (shown in Figure 4.13) and chose values for the thermal and hot solar wind electron pop-

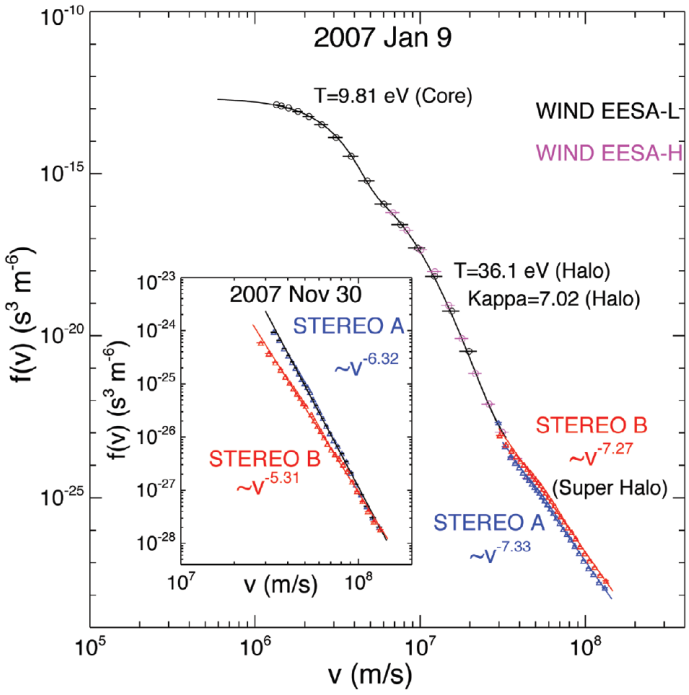

Figure 4.14: Plot of omnidirectional electron velocity distribution function from Yoon et al. (2013).

ulations based on work by Yoon et al. (2013) (see Figure 4.14). These values are based on observations at 1 AU, however, which means that they are likely to differ from those at Pluto's orbital distance. Solar wind electron measurements taken in the outer solar system would be useful, but it is unlikely to be a mission with the necessary instruments before the proposed ice giants flagship mission that is currently being studied for a possible launch at some point after 2025.

For the simulations that were performed on the Europa system, O_2 cross sections were taken from Itikawa (2009) and Anzai et al. (2012) and can be seen in Figure 4.15. Rates from Schreier et al. (1993) and Banks and Kockarts (1973) indicate that dissociative electron impact ionization of O_2 ($O_2^+ + e^- \rightarrow O^+ + O + 2e^-$) is a small component of total ion production resulting from electron impact ionization ($\sim$10%), and is therefore not currently

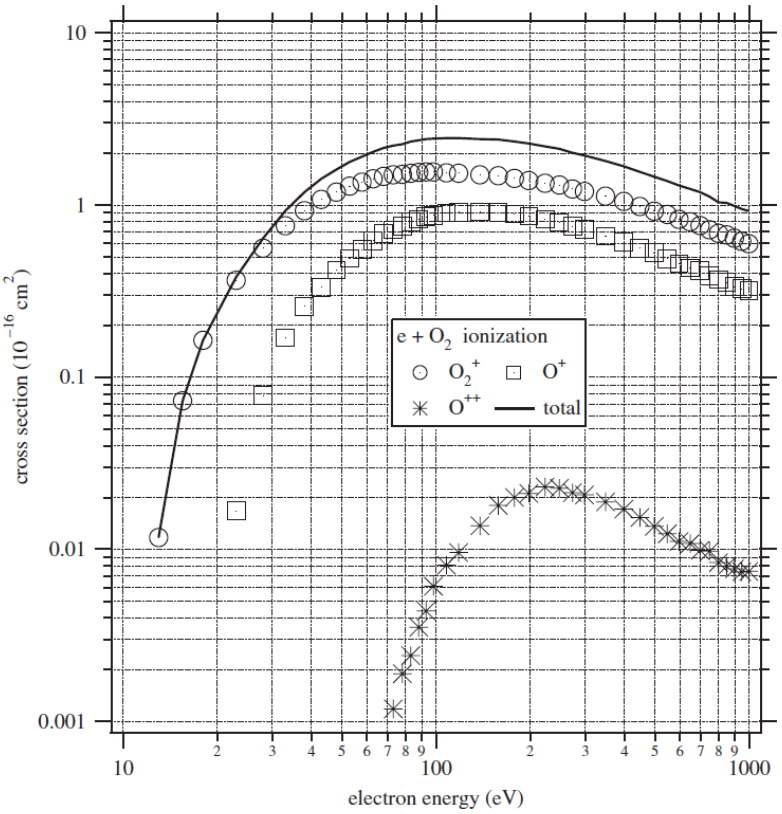

Figure 4.15: Plot of electron impact ionization cross sections for O_2. Values for O_2^+ are used Itikawa (2009).

included. The thermal and hot electron populations were chose to be 20 eV and 300 eV, respectively. These energies are from the medium Jovian plasma sheet values presented in Bagenal et al. (2015a).

4.5.2 Photoionization

Photoionization was implemented in the model by tracking the extinction of wavelength bins for which source rates are taken from Samson et al. (1989), although we have also examined flux rates published by Huebner et al. (1992) and work is ongoing to switch to the HEUVAC model by Richards et al. (2006). Fluxes are considered independently for each column parallel to the x-axis (as previously mentioned the Sun is in the -X direction

in both simulations of the Pluto-Charon system and of Europa). Any solar flux within a column that reaches the surface of a body is set to zero, creating shadows behind bodies within the system. While this does not allow for the existence of penumbras behind bodies within the simulation, this is not a significant effect in either system, given the small system sizes compared to the Sun-system distances (in neither system is the penumbra even one grid point wide at the back of the simulation domain). The ability to track extinction through the atmospheres of bodies and for those bodies to cast shadows causes asymmetric photoionization distributions, even in systems with radially symmetric atmospheres. It also allows for one body to impede photoionization of another body that it is eclipsing. Rates are calculated once at the beginning of a simulation and used for the remainder of the instance. This is because photon fluxes are assumed to be constant – the effects of events such as solar flares have not been explored with the model yet – and neutral particle populations within the systems simulated evolve on a much longer time scale. Photoionization rate distributions therefore do not change notably over the duration of the simulation.

$$\left(\frac{\partial \rho_\alpha}{\partial t}\right)_{\mathrm{ph}} = \sum_{\lambda} m_\alpha n_{n,\alpha} \Phi_\lambda \sigma_{\mathrm{ph},\lambda} \tag{4.15}$$

Equation 4.15 gives the ion production rate due to photoionization, where Φ_λ equals the photon flux in wavelength bin λ and $\sigma_{\mathrm{ph},\lambda}$ is the photoionization cross section for wavelength bin λ. For the Pluto simulations we used CH_4 photoionization cross sections published by Kameta et al. (2002), shown in Figure 4.16. Eighteen wavelength bins are used for our current implementation of CH_4 photoionization. For the Europa simulations, we use the O_2 photoionization cross sections from Itikawa and Ichimura (1990). Figure 4.17

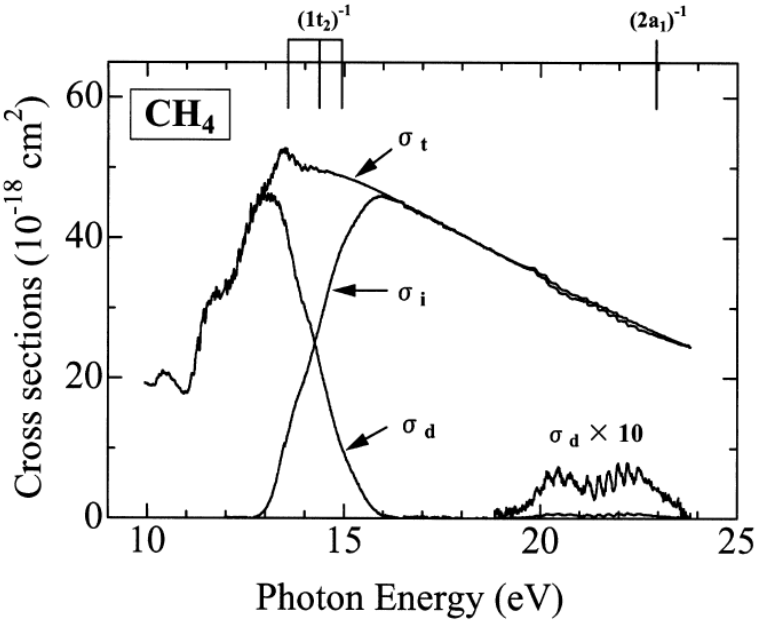

Figure 4.16: Plot of cross sections for neutral dissociation (σ_d), photoionization (σ_i), and photoabsorption (σ_t) for CH_4 from Kameta et al. (2002).

shows these cross sections. Currently, we use 29 wavelength bins and their corresponding cross sections to calculate O_2 photoionization in Europa simulations.

Figure 4.18 shows the photoionization rate distribution generated by the model for the Pluto-Charon system when Charon is directly upstream of Pluto. One can observe the asymmetry of the distribution resulting from extinction through the atmosphere. Not only is the rate on the Sun-side of the body significantly higher, extinction of solar flux causes it to drop dramatically before reaching the surface of Pluto. Note the shadow cast by each body. It may appear that Pluto's shadow possesses a penumbra. This is a result of extinction through the atmosphere, however. The localized effect of Charon eclipsing Pluto is also apparent in the plot.

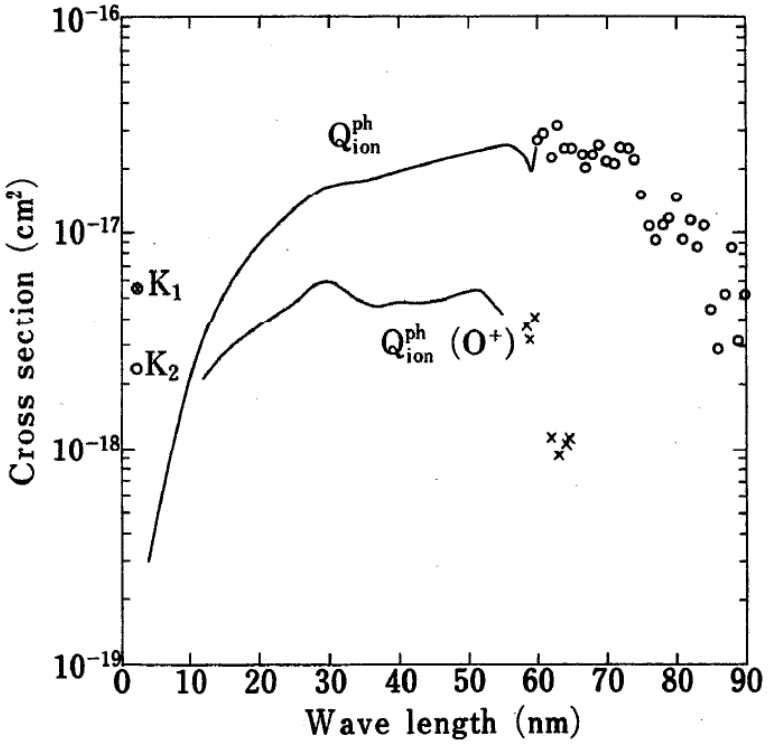

Figure 4.17: Plot of photoionization cross sections for O_2 from Itikawa and Ichimura (1990).

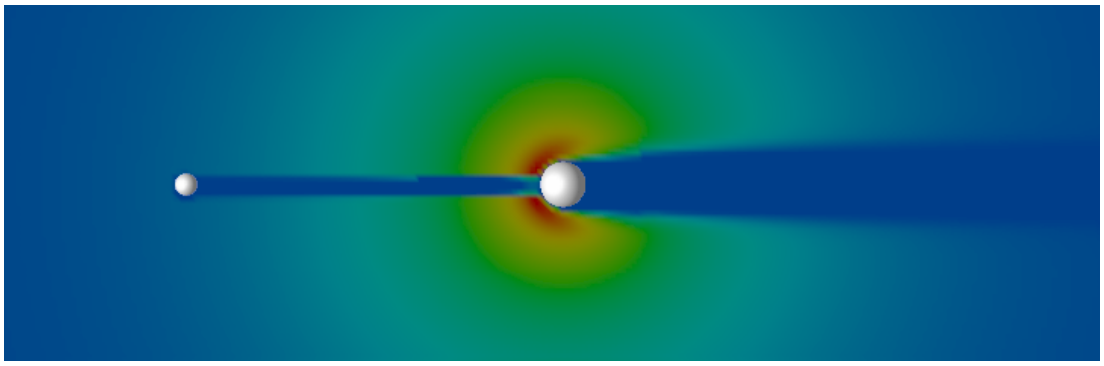

Figure 4.18: Demonstration of photoionization implementation within the model using configuration in which Charon is directly upstream of Pluto. Normalized photoionization rate is shown. Note that bodies cast shadows and incident flux is extincted as it passes through the neutral atmosphere. Sun is to the left.

4.5.3 Ion-Neutral Charge Exchange

One way that ion-neutral charge exchange is slightly more complicated to implement within the model than electron impact ionization or photoionization is that it involves mass being lost from fluids within the system, not just gained. It is therefore necessary to track changes to both the fluid for the species that is being created through the loss of electrons and the fluid for the species that is gaining electrons and recombining to become neutral (the incident species). Equation 4.16 gives the ion generation rate for the ion species being created, where $n_{n,\alpha}$ is the number density for the species being generated,$n_{\alpha_{\rm inc}}$ is the number density for the incident ion species, $v_{\alpha_{\rm inc}}$ is the bulk flow speed for the incident species, and $\sigma_{\rm ce}$ is the ion-neutral charge exchange cross section. Equation 4.17 provides the ion loss rate for the incident species, where $m_{\alpha_{\rm inc}}$ is the mass of the incident species, and $L_{\alpha_{\rm inc}}$ is the loss rate. This feeds back into Equations 4.1 and 4.2.

$$\left(\frac{\partial \rho_\alpha}{\partial t}\right)_{\rm ce} = m_\alpha n_{n,\alpha} n_{\alpha_{\rm inc}} v_{\alpha_{\rm inc}} \sigma_{\rm ce} \tag{4.16}$$

$$\left(\frac{\partial \rho_{\alpha_{\rm inc}}}{\partial t}\right)_{\rm ce} = m_{\alpha_{\rm inc}} n_{n,\alpha} n_{\alpha_{\rm inc}} v_{\alpha_{\rm inc}} \sigma_{\rm ce} = L_{\alpha_{\rm inc}} \tag{4.17}$$

We took different approaches for the implementation of ion-neutral charge exchange for the Pluto-Charon work than for Europa. For the Pluto simulations we used a single ion-neutral charge exchange cross section (40 Mb) for interactions between the solar wind and CH_4 within the Plutonian atmosphere and exosphere. This is because the rate, as reported by Koopman (1968), varies by less than $\sim$20% over the relevant energy range, as can be

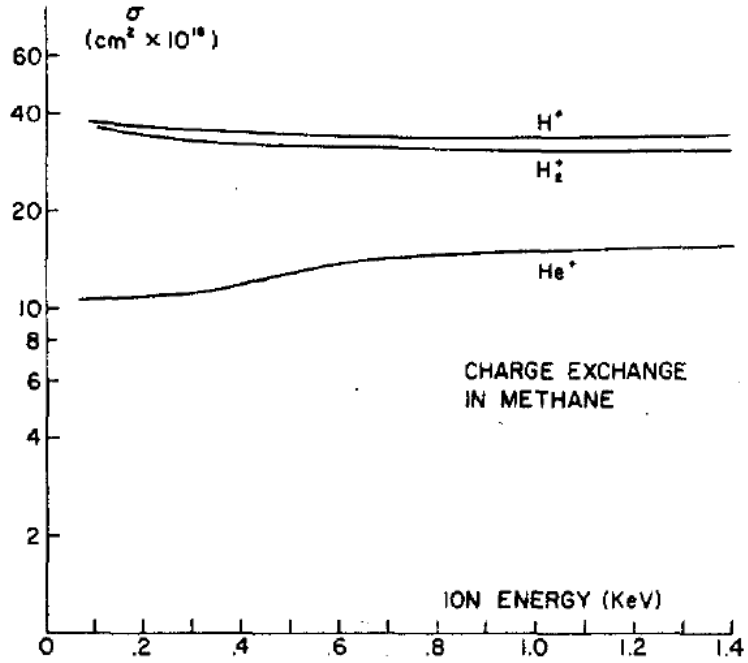

Figure 4.19: Plot of charge exchange cross sections for H^+ + CH_4 from Koopman (1968).

seen in the plot in Figure 4.19.

With Europa, it was necessary to use a more sophisticated treatment for several reasons. The first is that O^+ + O_2 charge exchange cross sections vary more widely with energy than those of H^+ + CH_4. Equation 4.18 gives the ion-neutral charge exchange cross section at a given energy of incident O^+ (Lindsay and Stebbings, 2005), where a_x values are empirical constants and E is the energy of the incident ion. This is calculated at each grid point within the model for every time step. Figure 4.20 shows a plot of the relevant cross sections. Note that values for the (^{4}S) rather than the (^{2}D,^{2}P) excitation state of O^+ are used. Cross sections for energetic ions are taken from Luna et al. (2005).

$$\sigma_{\mathrm{ce},O^+-O_2\rightarrow O_2^+}(E) = a_1(1-e^{\frac{-a_2}{E}})^2 + (a_3 - a_4 \ln E)^2(1-e^{\frac{-E}{a_5}})^4 \qquad (4.18)$$

The other reason is that much more information about how incident plasma parameters at

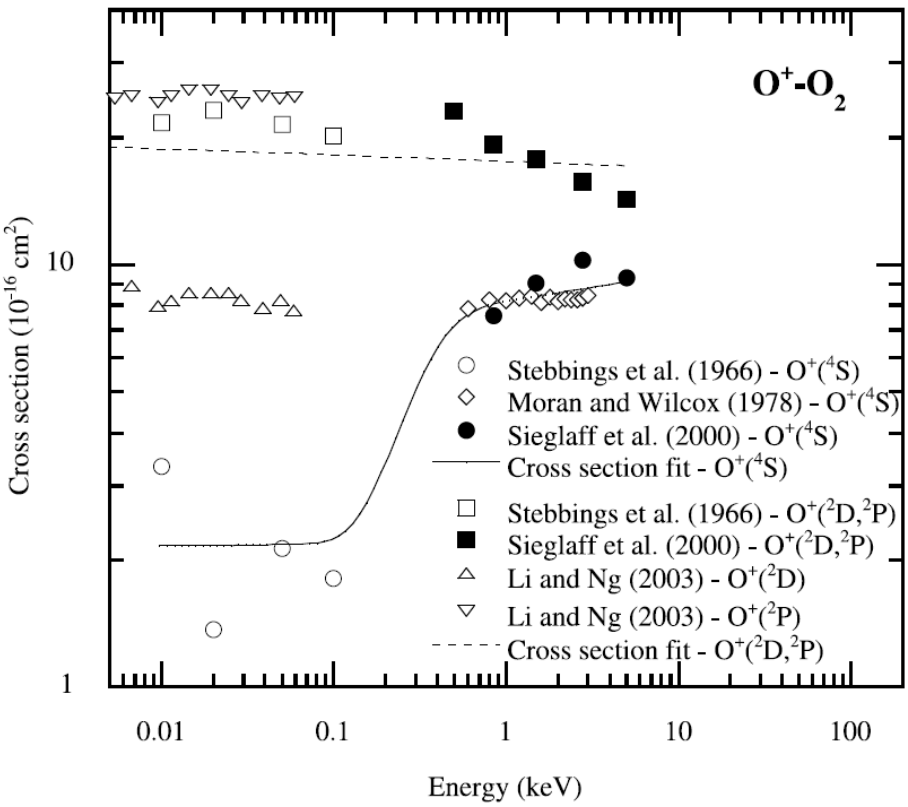

Figure 4.20: Plot of charge exchange cross sections for $O^+ + O_2$ from Lindsay and Stebbings (2005). O^+ (^4S) values are used.

Europa can change is known. This means that it is possible to choose from a range of documented case when deciding what to simulate. As the main purpose of our initial investigation of the Europan environment is to see how the ionosphere around Europa alters its interaction with the Jovian magnetosphere, most of our simulations so far have been based on what are expected to be average values at different locations within the Jovian magnetosphere. The values that we have chosen are based on the medium case from Bagenal et al. (2015a) which were based on simulations presented in (Delamere et al., 2005). Figure 4.21 shows radial profiles of relative abundance, and Figure 4.22 shows temperature profiles for different species, with O^+ being both the most abundant and the most energetic ion species near Europa's orbital distance from Jupiter.

It may be worthwhile to investigate the effect of adding S^{++} as a second species within the model. While the species fluid itself will not behave differently from O^+, due to it having the same mass to charge ratio, it has a significant fraction of the O^+ number density near Europa and will engage in charge exchange with O_2 at different rates, as ion-neutral cross sections for $S^{++} + O_2$ differ from those of $O^+ + O_2$.

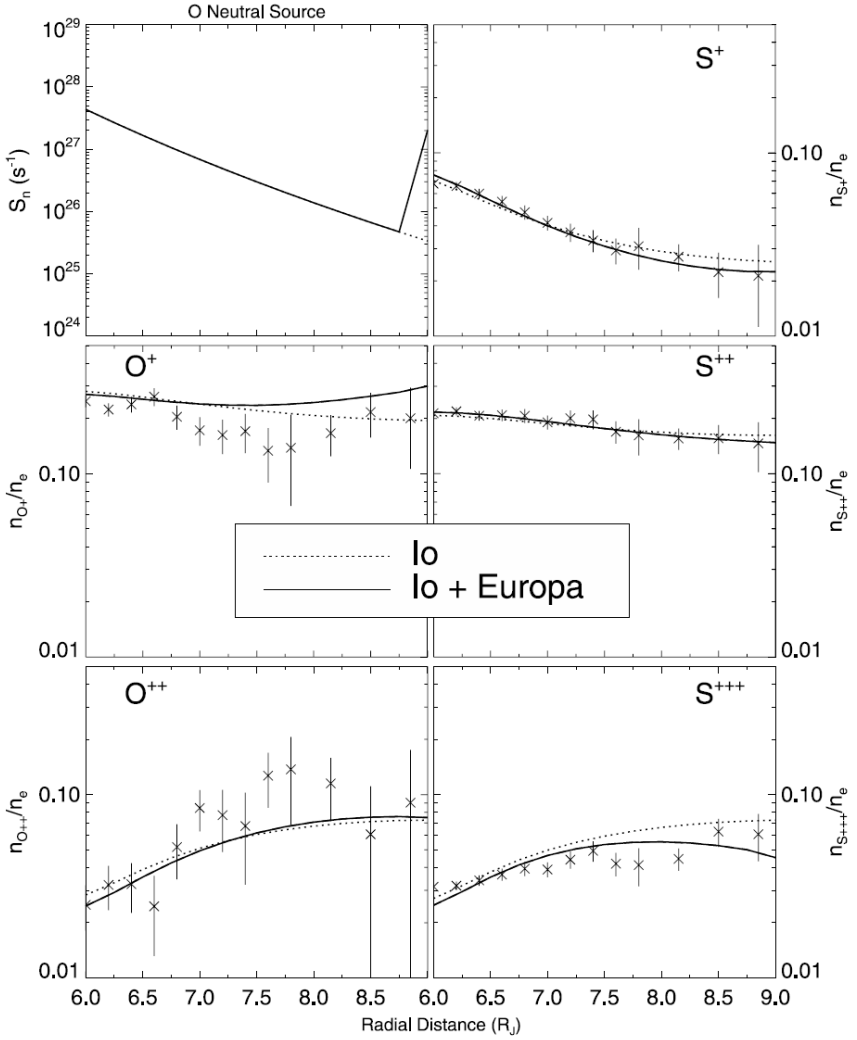

Figure 4.21: Relative abundances of Jovian plasma torus species from Delamere et al. (2005).

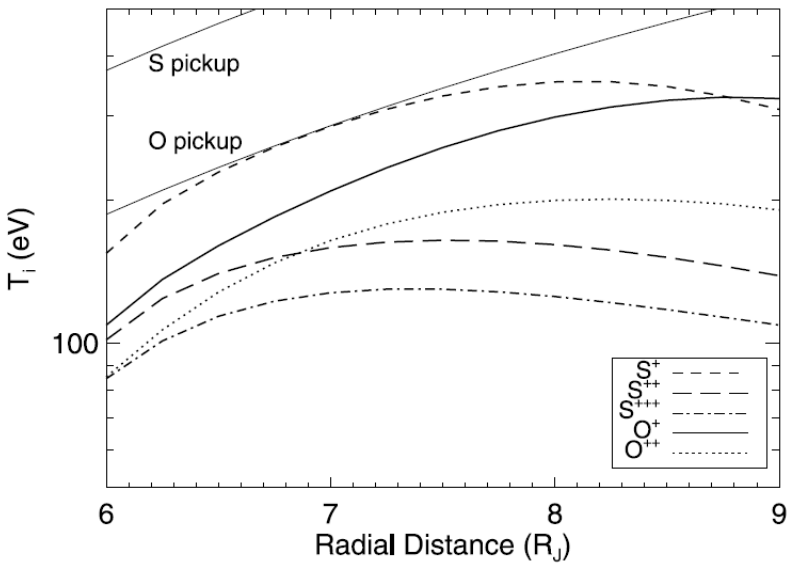

Figure 4.22: Jovian Plasma Radial Temperature Profile from Delamere et al. (2005).

4.5.4 Thermal Exchange

Heat exchange between the plasma and neutral particle populations has been implemented based on the work of Snowden et al. (2011) which involved the modeling of Titan's interaction with the Saturnian plasma environment using another variant of the R. M. Winglee (1998) model. Equation 4.19 gives the heat transfer to the plasma species, where $v_{n,\alpha}$ is the neutral velocity and $P_{n,\alpha}$ is the neutral pressure. Note that the neutral particles within both the Pluto system and the Europa system are relatively cold and therefore, this term results in an effective drop in average ion temperature. Equation 4.20 gives the electron cooling term. These equations feed back into Equation 4.3 and 4.4, respectively.

$$Q_{\mathrm{in},\alpha} = \frac{2m_\alpha n_\alpha v_{\alpha_{\mathrm{inc}}} \sigma_{\mathrm{ce}}}{m_\alpha + m_{n,\alpha}} \left(\frac{n_\alpha}{n_{n,\alpha}} P_{n,\alpha} - P_\alpha + \frac{n_\alpha m_{n,\alpha} (v_\alpha - v_{n,\alpha})^2}{3} \right) + S_\alpha \left(\frac{P_{n,\alpha}}{m_\alpha n_{n,\alpha}} + \frac{(v_{n,\alpha} - v_\alpha)^2}{3} \right) \tag{4.19}$$

$$Q_{\mathrm{en}} = \frac{P_{n,\alpha}}{n_{n,\alpha}} \sum_{\alpha} \left(\frac{S_\alpha}{m_\alpha} \right) \tag{4.20}$$

4.6 Accommodating Multi-Body Systems

In order to simulate Charon's effect on the Pluto-solar wind interaction, it was necessary to modify the structure of the model in a number of ways. In order to provide future flexibility, we decided to implement the multi-body capability in a highly extensible manner, so that an arbitrary number of bodies can be placed within the simulation domain in whatever locations are required. This will provide benefits for future uses of the model, but it did further complicate the modifications necessary to the model. These modifications included generalizing the way in which inner boundary conditions are implemented within the model, automating the way in which the model generates ionospheres and atmospheres around bodies, and the way in which the model determines locations of grid points, so that it was independent of the location of bodies – effectively, the presence of a planetary body within the simulation was made to be entirely optional, which might open up other possible applications in the future. Even processes involved in how an individual body is constructed within the model were made to be extensible, allowing, for example, more realistic neutral atmospheres with however many neutral species profiles might be required in order to accurately reflect the object being studied.

4.7 Modeling Europa's Induced Dipole

Currently Europa's induced dipole is implemented by imposing an analytical dipole based on the strength and direction of the X and Y components of the Jovian magnetic field (in the EphiO coordinate system). As has been discussed in Section 3.3, the Z component does vary as a result of the eccentricity of Europa's orbit, but the primary variations that drive the induced dipole are the X and Y components. This is done by taking in the direction and strength of the non-Z component of the background magnetic field, generating a dipole field based on the strength of the varying component of the magnetic field, rotating the coordinates of the field into a more convenient orientation, applying the required tilt to the dipole, then transforming the coordinates back into the EphiO coordinate system. This method will be revisited now that our initial investigation of the Europan interaction with the Jovian magnetosphere has been completed, as the ability to capture the effects of longer period, eccentricity based variations in the induced dipole field will allow the Icy Bodies Model to be used for investigations into the depth of Europa's subsurface ocean.

4.8 Inner Boundaries and Upstream Conditions

The inner boundary of the model uses a variation of the ghost cell method, in which simulation cells have physical values within them, and can alter the non-ghost cells around them, but cannot be altered themselves. This allows the model to simulate the presence of a solid body within the system without many of the complications that can arise from such boundaries. A consequence of this technique is that the inner boundary of the model does transfer some amount of material into the system due to numerical diffusion and pres-

sure gradients between ghost cells and the active simulation domain. In earlier versions of the model, this was the only source of plasma into the simulation and was therefore desirable so that the ionospheric species present within the simulation were not depleted over time. With the addition of volumetric plasma sources within the model, however, this is no longer necessary, and ghost cell pressures and densities have been decreased in order to minimize mass and momentum transfer out of the inner boundary. Unfortunately, due to the limitations that Alfvén velocities within the ghost cells place on the simulation's time step size, this can only be reduced so much without impairing the efficiency of the model. Ionospheric resistivity is increased with decreasing altitude above the body.

The upstream conditions are implemented within the model through further use of ghost cells at the -X boundary of the simulation, in which incident flow parameters are set in order to provide a continuous flow of new upstream material into the system (solar wind in the Pluto simulations and JMP in the Europa simulations). Typically, the model is initialized with some portion of the simulation domain prepopulated with the incident plasma fluid so that the results may be obtained more quickly. The model is capable of varying upstream conditions dynamically, but we have not done so in any of the simulations described within this dissertation, as they have not been focused on transient phenomena. Subsection 7.2.1 discusses possible future investigations that could make use of this capability.

CHAPTER 5

THE PLUTO SYSTEM

5.1 Interaction Characteristics

When Pluto is considered independently of Charon, as it is in case P.1.1, the interaction between Pluto's ionosphere and the solar wind is what one would expect from an unmagnetized body. Visible in the first panel of Figures 5.1, 5.2, and 5.3, the subsolar standoff distance for the shock is at 7 R_P and the shock distance on the plane of the terminator is 20 R_P in the -Z direction and 15 R_P in the Z direction, in line with results from Harnett et al. (2005) with similar system parameters. Furthermore, a plasma sheet forms downstream of Pluto with corresponding draping of magnetic field lines, which is expected for such an obstacle to the flow of the solar wind (case P.1.1 in Figure 5.7).

5.2 Structural Effects

As can be seen by comparing cases P.1.1 and P.1.5 in Figures 5.1 and 5.2, the shock structure sunward of Pluto is greatly altered by the presence of Charon upstream when Charon possesses an ionosphere. The the maximum density enhancement decreases by $\sim$50% between cases P.1.1 and P.1.5 (in case P.1.1 the H^+ density jumps from 0.01 cm^{-3} to 0.1 cm^{-3}, while in case P.1.5 it only increases to 0.05 cm^{-3}) and the maximum plasma pressure within the shock drops by $\sim$60% (from 600 fPa to 230 fPa). Furthermore, the region directly upstream of Pluto is at or below the freestream solar wind density. Additionally, the shock angle is decreased for the shock overall. While cases P.1.2 and P.1.3 demonstrate

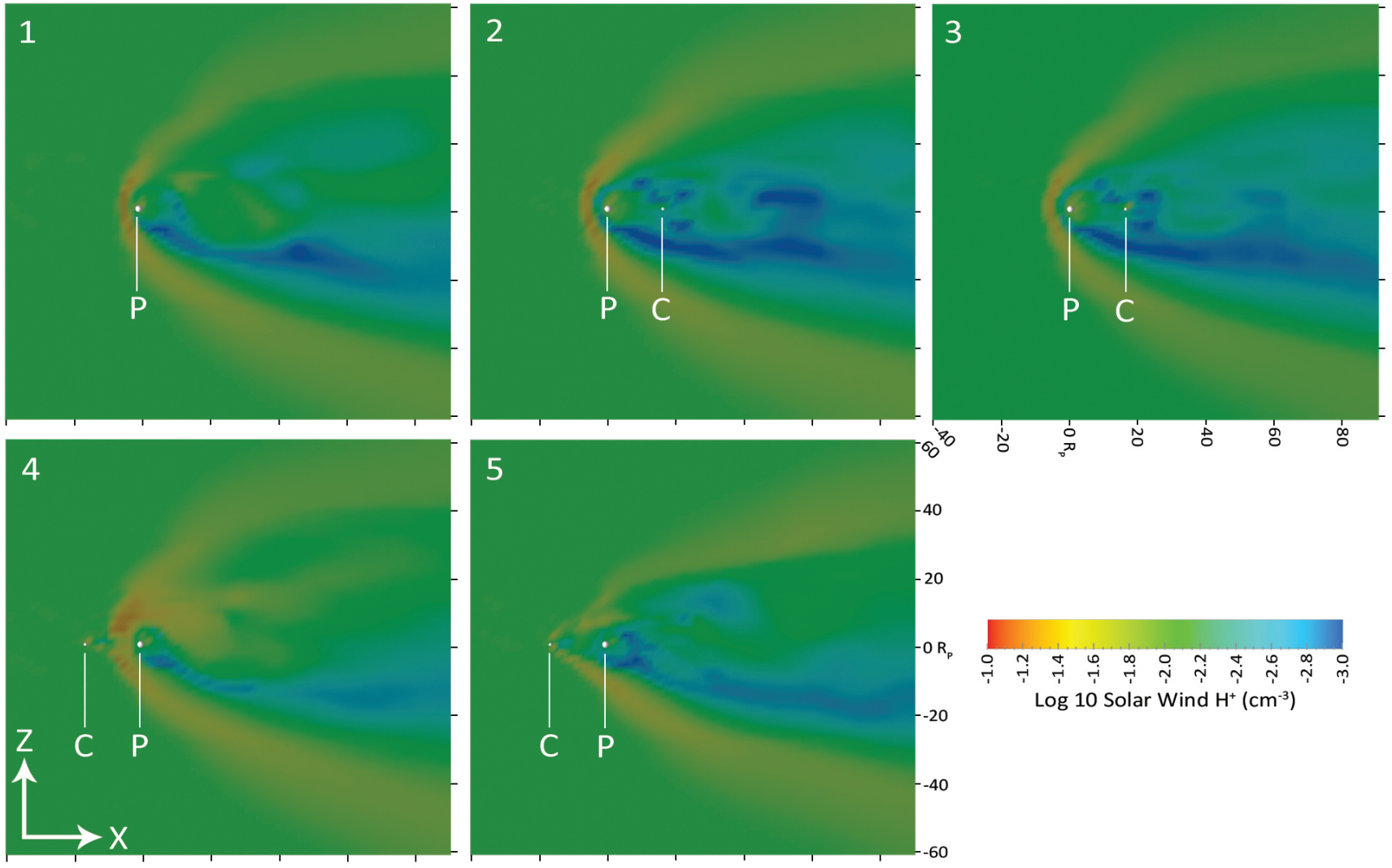

Figure 5.1: Number density of H^+ from the solar wind for cases P.1.1 through P.1.5 is shown in the XZ plane (Y is pointing out of the plane). Solar wind flow is in the positive X direction and the IMF is pointed in the negative Y direction. Positions of Pluto and Charon are labeled in each case and each body is at Y = 0.

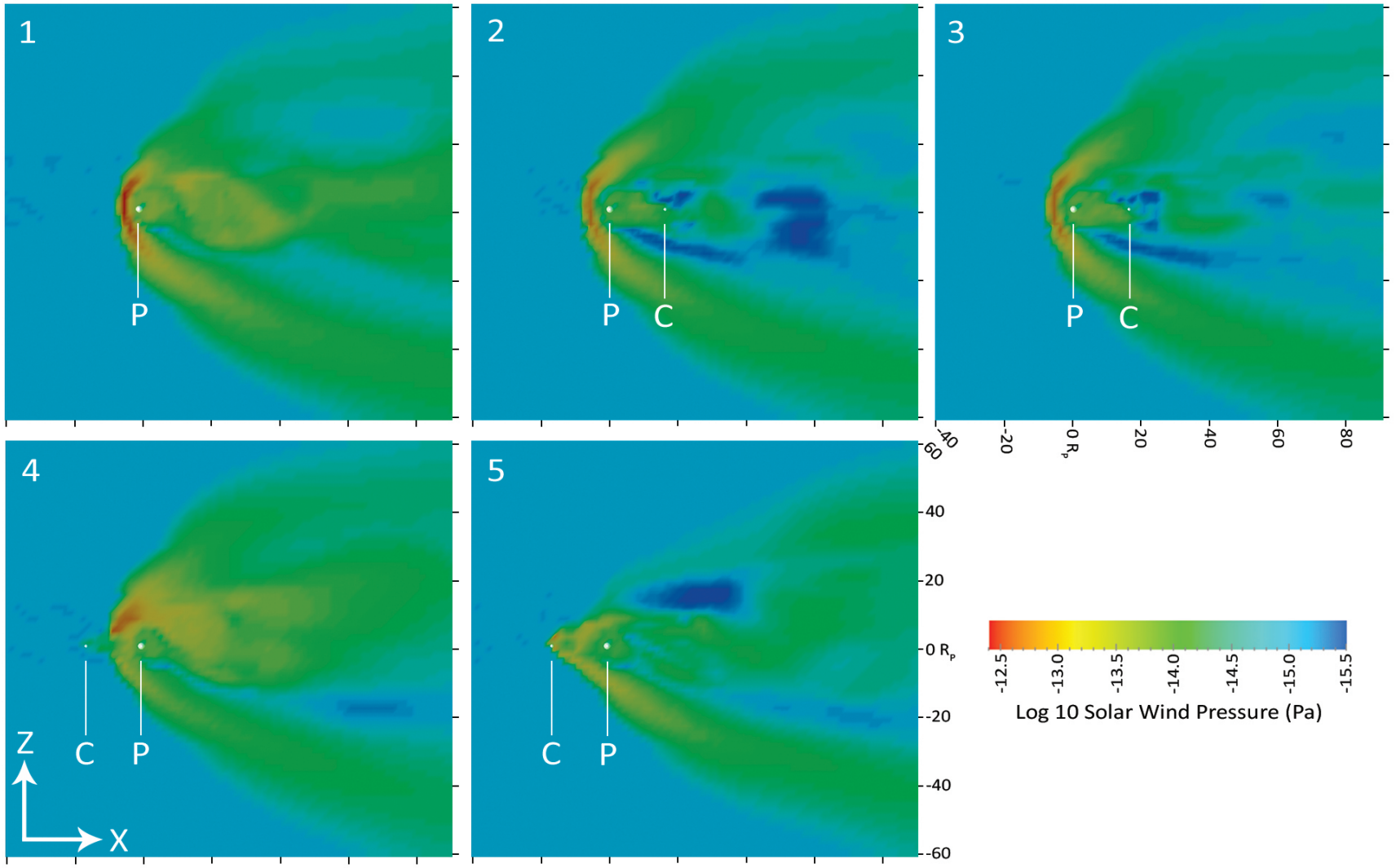

Figure 5.2: Solar wind H^+ plasma pressure for cases P.1.1 through P.1.5 is shown in the XZ plane. Frames are oriented as in Figure 5.1.

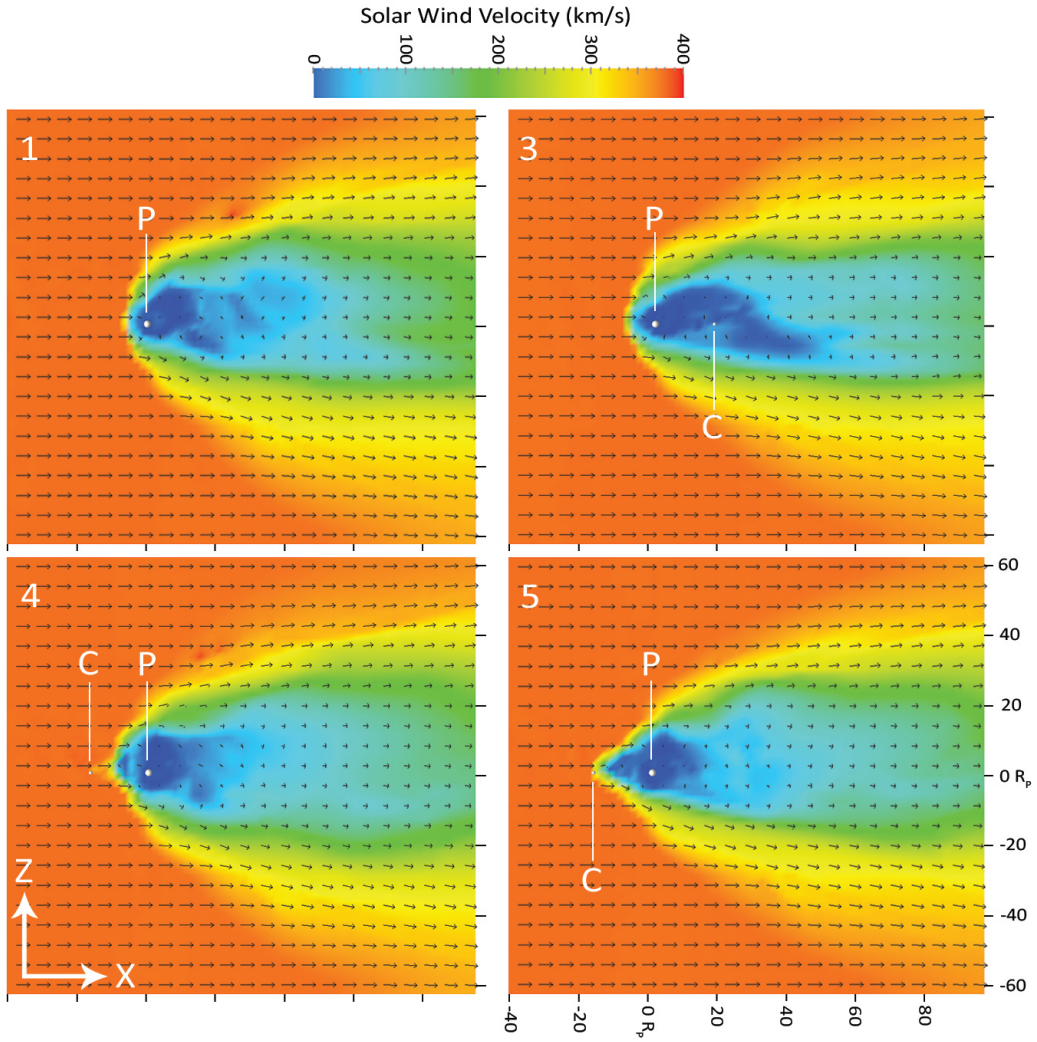

Figure 5.3: Solar wind velocity vector fields are shown for cases P-1-1, P-1-3, P-1-4, and P-1-5. Frames are oriented as in Figure 5.1

notable differences from case P.1.1, namely more fine-scale structure within the ionopause, they are largely similar to each other. Therefore only case P.1.3 will be given attention in some of the discussion in this chapter. As is to be expected given the supersonic, super-Alfvénic upstream conditions in case P.1.4 (the case in which Charon is upstream of Pluto but does not have an ionosphere), Charon causes a significant – if localized – effect within the system. This is in contrast to the subsonic regimes that icy moons of Jupiter and Saturn typically inhabit, where plasma is able to flow around the object.

Alterations to the structure of the interaction region in case P.1.5 are even more evident in the solar wind velocity fields shown in Figure 5.3. Rather than the rounded shape seen in the upstream direction in cases P.1.1 and P.1.3, Pluto and Charon form a unified obstacle to the solar wind flow in case P.1.5. Conversely, the confined nature of Charon's effect in case P.1.4 is highlighted by looking at the velocity field.

Magnetic field vector fields for each case are shown in Figure 5.7. Charon's effects are less apparent in the magnetic field data than in the solar wind density and velocity data. While density increases are impeded and flow is drastically slowed by the presence of Charon, marked magnetic field increases are still present in the region between Pluto and Charon in case P.1.5, with a lesser increase in the vicinity of Charon. Charon's effect on the magnetic field configuration is even less pronounced in case P.1.4.

5.3 Pickup Ion Asymmetries

Asymmetries due to the direction of the IMF dictating gyromotion are present in each of the cases, although they are most apparent in case P.1.5 due to asymmetric pickup occurring from two distinct plasma sources as seen in the corresponding panel in Figure 5.5.

IMF-caused asymmetries are also clearly visible in the plots of Pluto sourced 28^+ velocity vector fields displayed in Figure 5.6. Both Pluto sourced 28^+ and Charon sourced 28^+ move preferentially in the -Z direction due to gryomotion. As the ions move away from their parent bodies and into the magnetosheath, they follow the direction on the magnetic field within the magnetosheath. This is to be expected, as the ions only undergo gyromotion if their velocity vector has a component which is perpendicular to the direction of the magnetic field through which they are traveling. In cases P.1.1 and P.1.3, in which the

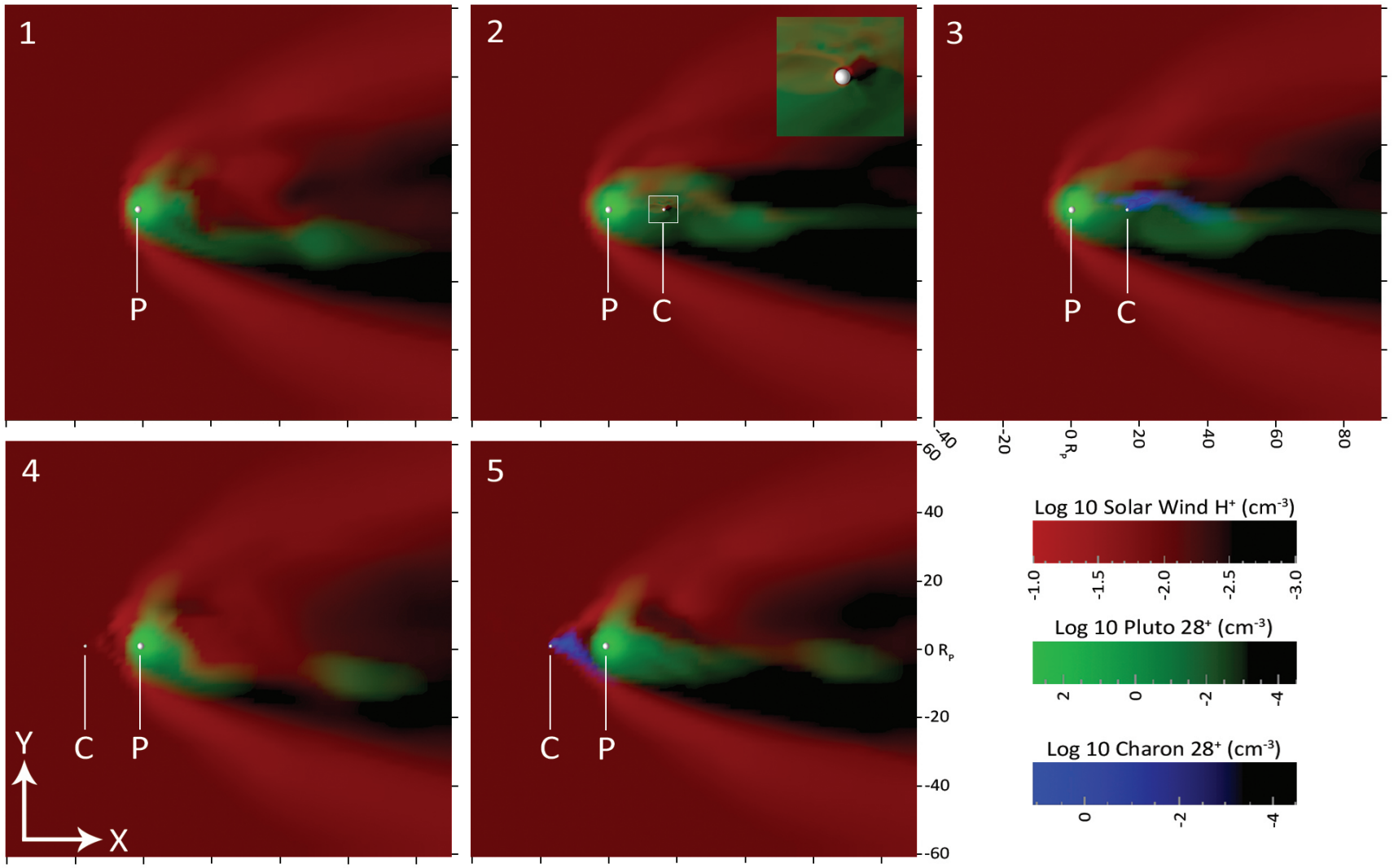

Figure 5.4: Densities for each species are shown in the XY plane for cases P.1.1 through P.1.5. Colors correspond to different species, with opacity indicating density. Red is solar wind H^+, green is 28^+ sourced from Pluto, and blue is 28^+ sourced from Charon. The magnified view of Charon in case P.1.2 uses data from a higher resolution inner grid box in order to show the geometric wake downstream of Charon. This higher resolution data is also shown within the white indicator box. While a similar wake is present in case P.1.3, no magnified view is provided, as the Charon sourced 28^+ ion species dominates the region in question. Frames are oriented as in Figure 5.7.

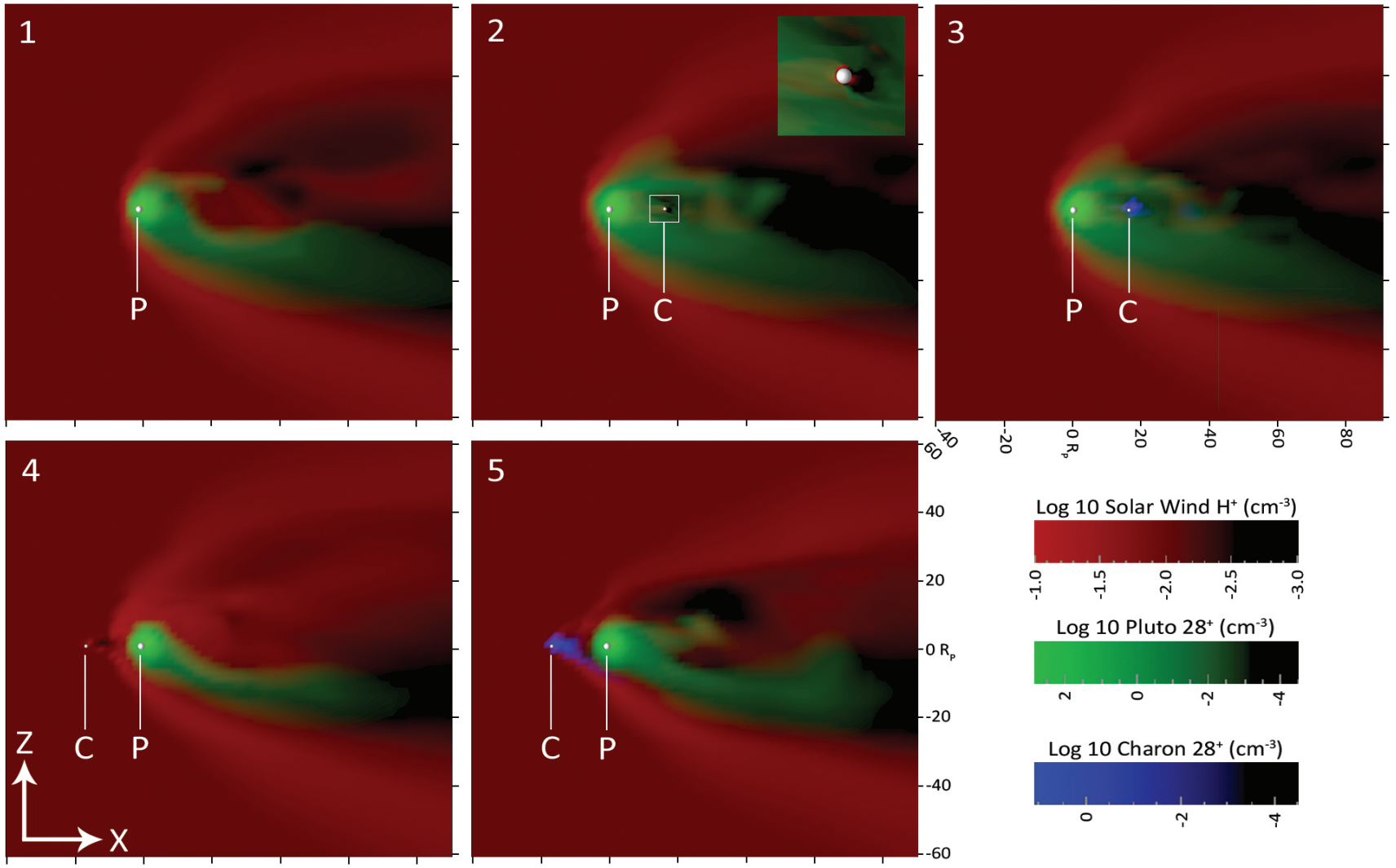

Figure 5.5: Densities for each species are shown in the XZ plane for cases P.1.1 through P.1.5. Colors correspond to different species, with opacity indicating density. Red is solar wind H^+, green is 28^+ sourced from Pluto, and blue is 28^+ sourced from Charon. The magnified view of Charon in case P.1.2 uses data from a higher resolution inner grid box in order to show the geometric wake downstream of Charon. This higher resolution data is also shown within the white indicator box. While a similar wake is present in case P.1.3, no magnified view is provided, as the Charon sourced 28^+ ion species dominates the region in question. Frames are oriented as in Figure 5.1.

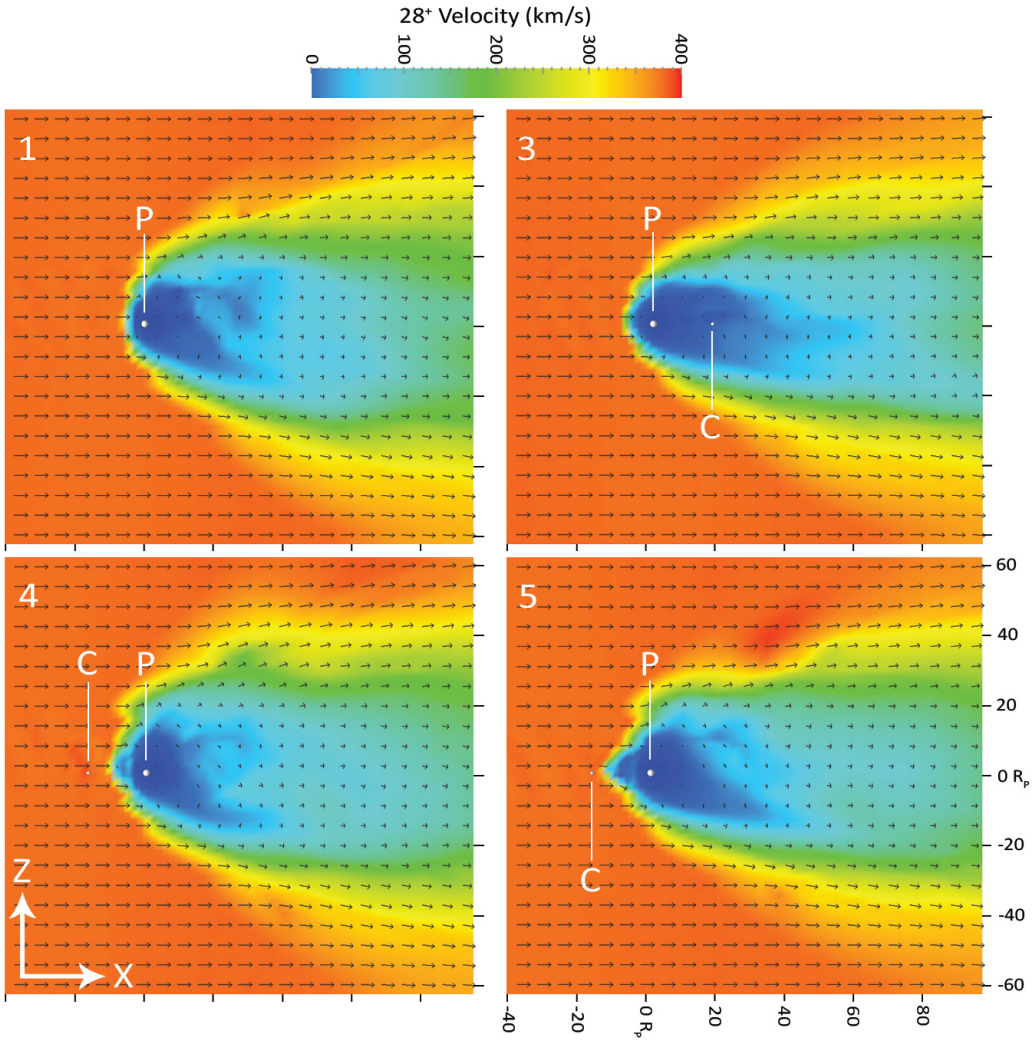

Figure 5.6: 28^{+} velocity vector fields are shown for cases P-1-1, P-1-3, P-1-4, and P-1-5. Frames are oriented as in Figure 5.1

shock structure is not altered by Charon, the gyromotion of heavy pick up ions from Pluto is more overt than in case P.1.4, which is in turn more overt than in case P.1.5. This is a consequence of the the shock angle and attendant shape of the magnetosheath.

5.4 Plasma Wake

5.4.1 Mass Loss from System

In case P.1.1 the Pluto sourced pickup ions, as can be seen in the figure, have a bulk velocity and density of $\sim$100 km/s and 0.006 cm^{-3} respectively, which agrees well with measurements made by SWAP (Solar Wind Around Pluto) during the New Horizons encounter (90 km/s and 0.009 cm^{-3}) (McComas et al., 2016). Close comparison of cases P.1.4 and P.1.5 against cases P.1.1 and P.1.3 in Figures 5.4 and 5.5 reveals a 75% decrease ($\sim 5\times10^{-3}$ cm^{-3} vs. $\sim 2\times10^{-2}$ cm^{-3}) in local peak density. We also calculated integrated fluxes of the Pluto sourced 28^{+} species within the tail region 50 R_P downstream of Pluto, finding a flux of $\sim 1.11\times10^{24}$ s^{-1} in case P.1.1, which is comparable to the $\sim 5\times10^{23}$ s^{-1} calculated by McComas et al. (2016) based on SWAP measurements made during the New Horizons encounter. For cases P.1.4 and P.1.5 we calculated fluxes of $\sim 9.2\times10^{23}$ s^{-1} and $\sim 9.0\times10^{23}$ s^{-1}, respectively. These are averages of values measured over $\sim$500 s of simulated time (from $\sim$1500 s EST to $\sim$2000 s EST). Flux rates were also measured at both greater and lesser distances downstream of Pluto within the simulation (25 R_P and 100 R_P), with little variation from the given values. This corresponds to a $\sim$20% decrease in heavy ion flux between case P.1.1 and case P.1.5. These relative fluxes were stable once a quasi-steady state is reached, suggesting that Charon is providing some degree of shielding against at-

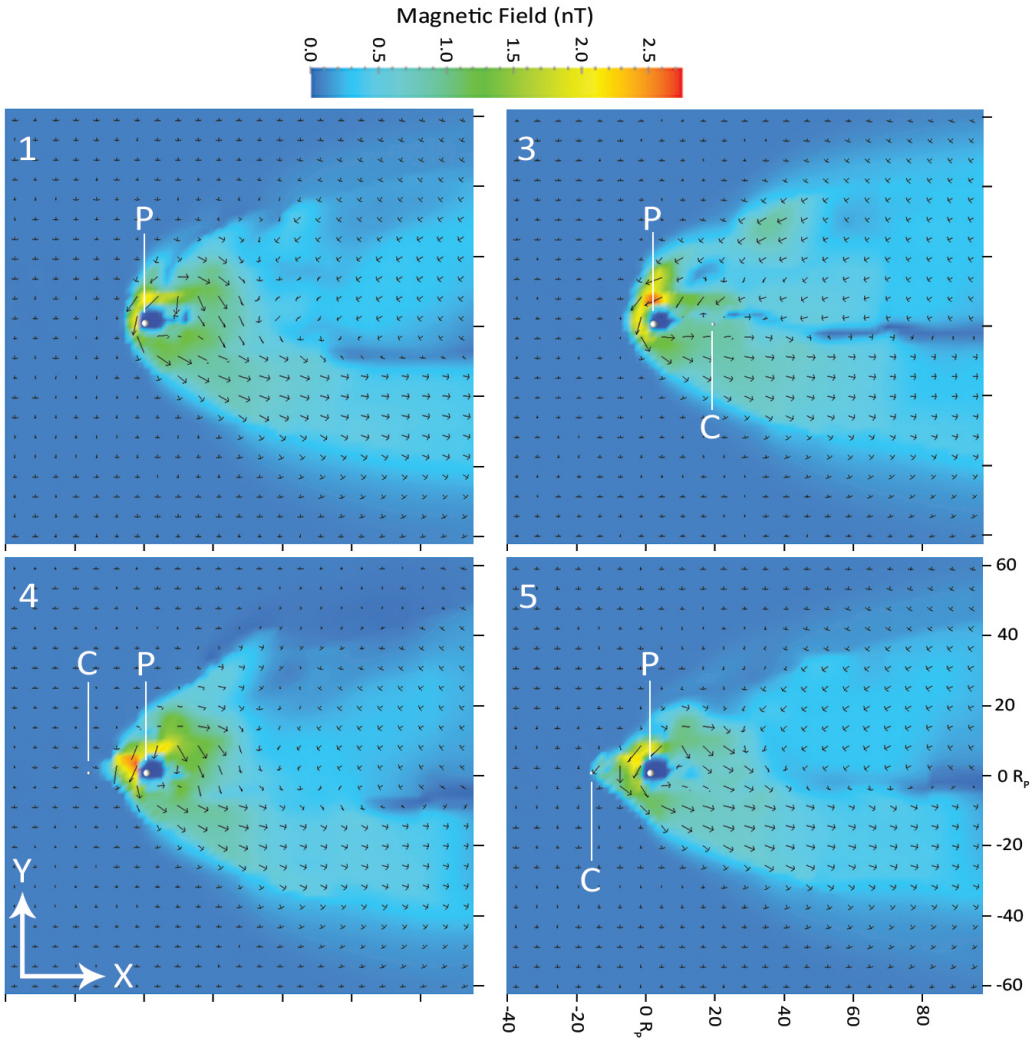

Figure 5.7: Magnetic field vector fields are shown for cases P-1-1, P-1-3, P-1-4, and P-1-5.

mospheric loss while upstream.

5.4.2 Plasma Sheet

Case P.1.3 manifests a notable reconfiguration of magnetic fields relative to case P.1.1. In case P.1.3, the formation of the region of anti-parallel magnetic field lines behind Pluto – corresponding to a plasma sheet – is observed to occur closer in to Pluto than in the other cases. The density structure of these plasma sheets can be seen in Figure 5.4. In case P.1.3

of the figure, plasma originating from Charon is present in a region which is depleted of solar wind plasma. In each of the cases a concentration of solar wind H^+ predictably coincides with a region of anti-parallel magnetic field vectors as shown in Figure 5.7, indicating the location of the plasma sheet.

5.4.3 Geometric Wake behind Charon

A geometric wake in the flow of Pluto sourced 28^+ that extends $\sim$3 R_C is present downstream of Charon in cases P.1.2 and P.1.3, as can be seen in Figures 5.4 and 5.5. This is result matches well with Monte Carlo modeling results by Hoey et al. (2017) and observations of Charon's poles which indicate the possibility of material lost from Pluto being deposited on Charon (W. M. Grundy et al., 2016). This is a particularly plausible explanation for Charon's polar discoloration in light of the discovery by New Horizons that most material escaping from Pluto's atmosphere is CH_4 rather than N_2 as CH_4 could cause a coloration similar to what was observed.

5.5 Volumetric Sources

Cases P.2.1 and P.2.2 were performed for several reasons, as discussed in Subsection 4.1.2. Chief among them was to see how the addition of neutral particle interactions to the model would change the system's interaction with the solar wind and to assess how the unexpectedly dense solar wind at the time of the New Horizons encounter might have altered the interaction compared to what was thought to be a normal set of conditions. In order to accomplish this we performed one simulation (P.2.1) with the same system parameters that were used for case P.1.1 (as close as was possible, given the changes that were made to im-

plement accurate volumetric plasma sources within the model) and one simulation (P.2.2) with the plasma parameters that were measured by New Horizons during its encounter.

The results, shown in Figures 5.8 and 5.9 show that case P.2.1 matches closely to P.1.1 in terms of bow shock stand off distance and structure of the interaction region, with the exception of an increase in solar wind particles being diverted in the +Z direction. This result corresponds well with such a feature being more prominent within the results of Delamere (2009), which used a hybrid kinetic treatment. Overall, the changes made to implement neutral particle interactions within the model seem to have remained consistent with those obtained using the previous version of the model, except where those differences indicate a more physically accurate result.

The results of case P.2.2 showed that when the solar wind is significantly more dense and moves at a faster speed, the bow shock stand off distance moves closer in to the body, as would be expected. The shock structure has a more acute angle in the -Z direction compared to case P.2.1 (visible is both the XZ panel in Figure 5.8 and the density and velocity plots in Figure 5.9). Gyromotion is also somewhat less pronounced in this case, as can be seen in Figure 5.8. We interpret this as being a similar phenomenon to what was noted in Section 5.3, where the change in the shock structure affects pick up ion motion. Comparisons between the results for case P.2.2 and New Horizons results are given in Subsection 5.6.2.

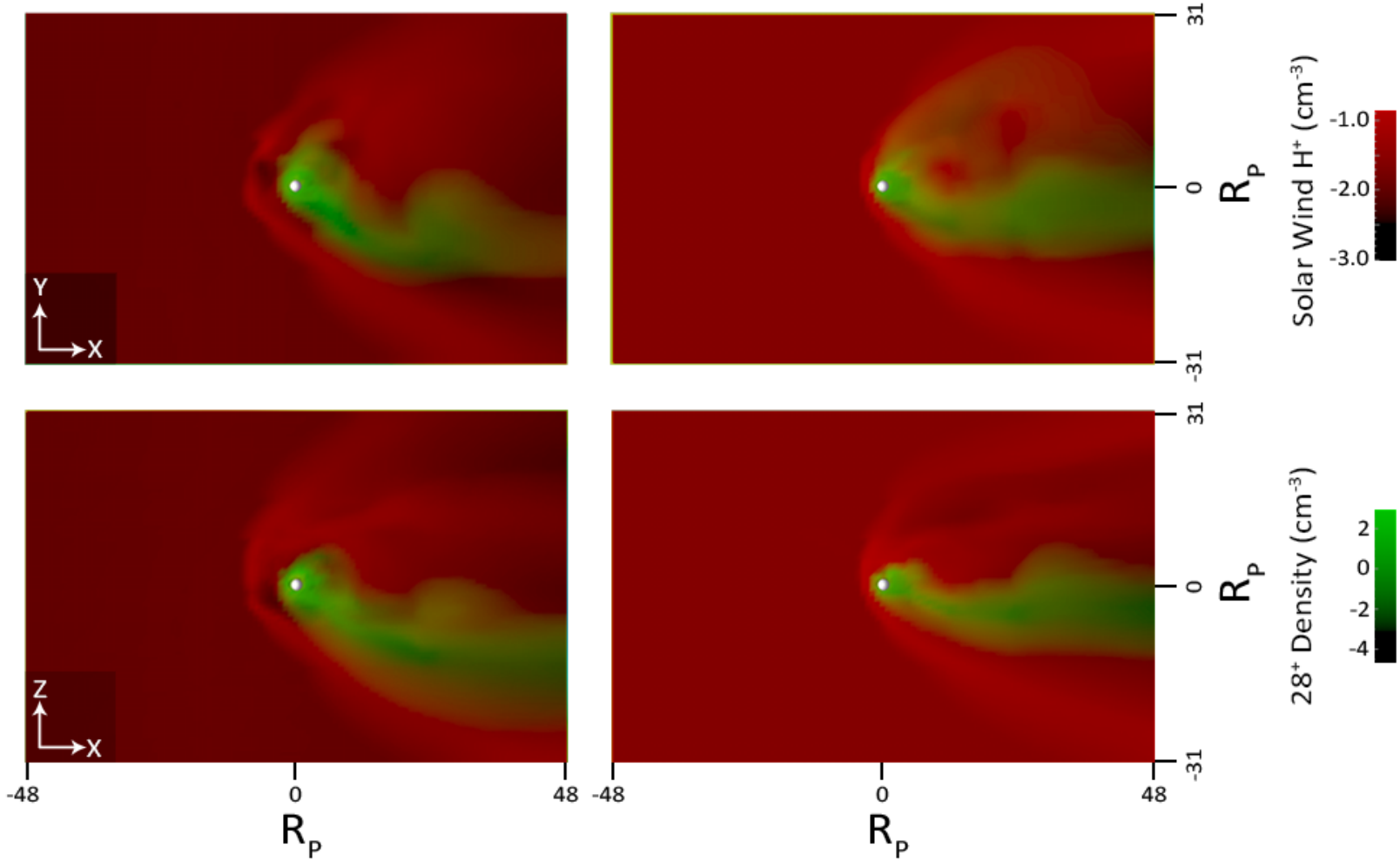

Figure 5.8: Plots of solar wind and CH_4^+ number densities in the XY and XZ planes from case P.2.1 (Left) and P.2.2 (Right).

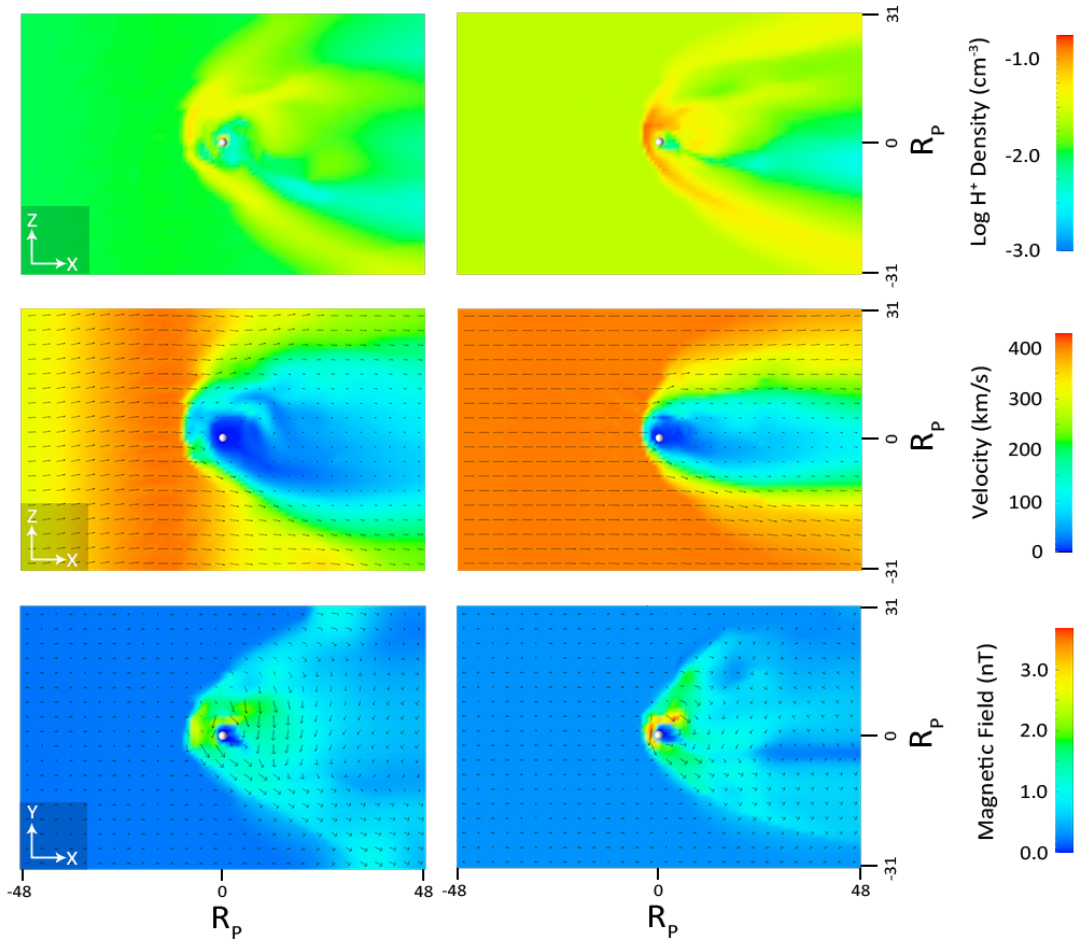

Figure 5.9: Plots of (Top) solar wind number density, (Middle) solar wind velocity vector fields, and (Bottom) magnetic field vector fields from case P.2.1 (Left) and P.2.2 (Right). Areas near axis labels are shaded to increase visibility.

5.6 Validation of Results

5.6.1 System Structure

Figure 5.10 shows plots of profiles of values taken along the X direction of a simulation performed by Delamere (2009), while Figure 5.11 shows the same for the P.1.1 case that was simulated for this work. The profiles have been plotted in order to ease the comparison of results from the two models. There are several differences that should be noted, the first being that they see a smaller peak ion density and a larger peak magnetic field strength than are present in our results. No indication of inner boundary conditions is given, so it may be possible that their simulation ignores the presence of Pluto's physical surface, treating it as a point source of neutral particles (this seems likely to be the case, as the resolution of their simulation is $>\mathrm{R_P}$ at 1800 km). This would explain some of the differences between our simulation and theirs, as we impose an ionospheric profile down to the surface of Pluto, which requires a high local density near the surface. The interior of Pluto is filled with unalterable ghost cells with predetermined plasma values, as was discussed in Section 4.8. Values within the surface of Pluto are therefore not representative of what is occurring at other locations within the simulation, explaining the region of zero magnetic field strength in the middle of the pile up region, as well as the much higher second peak in solar wind density within our model compared to theirs. The smaller, first peak in solar wind density corresponds to the shock structure, and matches well with their peak solar wind density. The most significant deviation between results that cannot be trivially explained by the presence of a simulated solid object within the Icy Bodies Model is the comparatively sudden drop in bulk flow speed within our model. This is partially due to the large increase

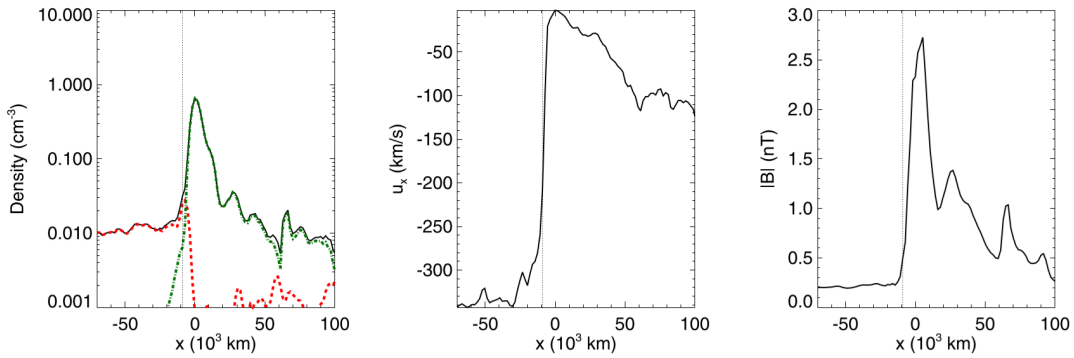

Figure 5.10: Profiles along X dimension for number densities (black is total, red is solar wind, and green in pickup ion), bulk velocity, and magnetic field strength (Delamere, 2009).

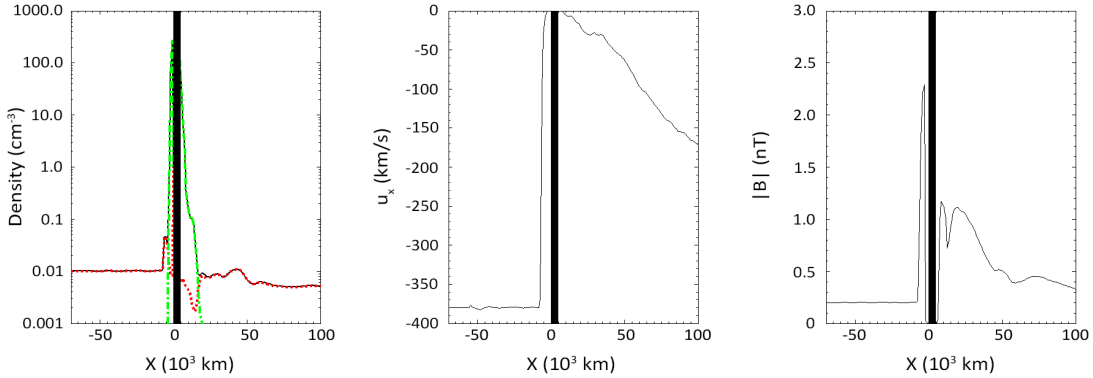

Figure 5.11: Profiles taken from case P-1-1 along X dimension (through center of Pluto) for number densities (black is total, red is solar wind, and green in pickup ion), bulk velocity, and magnetic field strength. Black region immediately around zero is within Pluto. Used for comparison with Delamere (2009) results shown in Figure 5.10.

in ionospheric density near the surface of Pluto, which greatly impacts the bulk flow speed. Many key features do match well between the two models, however, notably the locations of the bow shocks and the similar enhancements in solar wind density within the bow shocks, as well as the comparable velocity and magnetic field strength profiles in the wake region of the simulations.

5.6.2 Comparison with New Horizons Results

Because very different plasma parameters were used for cases P.1.1 through P.1.5, based on pre-encounter estimates, it is helpful to compare the results of these simulations with those of New Horizons in multiple different ways. The best quantitative comparison that can be made between the two is the heavy ion mass loss rates that were discussed in Section 5.4.1. The close match between the values from the model and the estimates McComas et al. (2016) made based on observations during the encounter are encouraging. Cases P.2.1 and P.2.2 are also useful for making this comparison, as they were performed using both sets of parameters – the pre-encounter parameters and the measured parameters – and can therefore act as a bridge between the initial cases that were simulated with what was observed at Pluto. The most significant comparison that can be made is between case P.2.2 and the results from McComas et al. (2016) as well as Bagenal et al. (2016). SWAP measurements and the resulting model of the shape of the interaction region (see Figure 2.8) indicate that the bow shock near Pluto at the time of the New Horizons encounter was $\sim$4.5 $\mathrm{R_P}$ upstream of the body. This matches well with the value of 4.4 $\mathrm{R_P}$ from case P.2.2. This, in combination with the broad similarities in results between cases P.2.1 and P.1.1 and the similar mass loss rates, suggest that the results from cases P.1.1 through P.1.5 are a reasonable representation of what the system interaction would look like under less extreme solar wind conditions.

CHAPTER 6

THE EUROPAN INTERACTION

In contrast to Pluto and Charon's interaction with the solar wind, Europa is embedded within a sub-Alfvénic and subsonic flow with periodically varying upstream magnetic field conditions. This has several implications. One is that no shock forms upstream of the body in either the cases in which Europa is within the thermal population of the Jovian plasma sheet, or in the cases where it is above/below the plasma sheet. Another is that Alfvén wings can be observed in the space near the body, as will be discussed in Subsection 6.3.2. Some general characteristics of the interaction that are either a consequence of using a multifluid MHD treatment or enhancements that have been made to the model are also worth noting. These include the observable asymmetry in the enhancement of Jovian magnetospheric plasma on the upstream or anti-corotational side of Europa as well as the increase in ion production rate with decreasing distance from Europa's surface. All of these features are visible in the exploratory results discussed below. All visualizations use the EphiO coordinate system, in which the X axis is in the direction of the orbital motion of Europa as well as the corotational flow, the Y axis points towards Jupiter, and Z points in the direction of Jupiter's spin axis.

6.1 Effect of Position within Jovian Magnetosphere

As was discussed in Section 3.3.2, Europa's induced dipole is generated in response to changes in the background Jovian magnetic field. These changes are a result of the tilt in Jupiter's magnetic dipole relative to its rotation axis as well as the eccentricity of Europa's

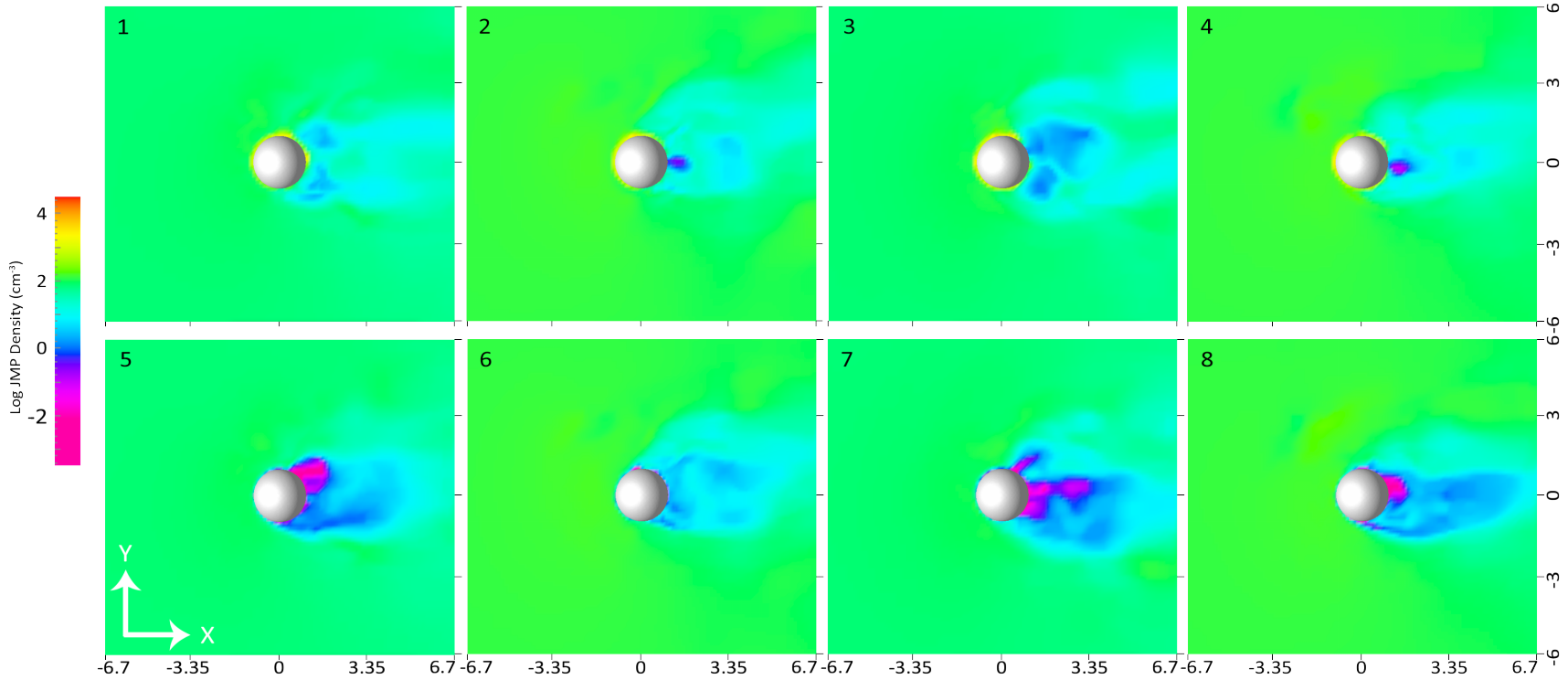

Figure 6.1: JMP number densities are shown for each case in the XY plane. Europa is at the center of each panel and coordinates are in EphiO.

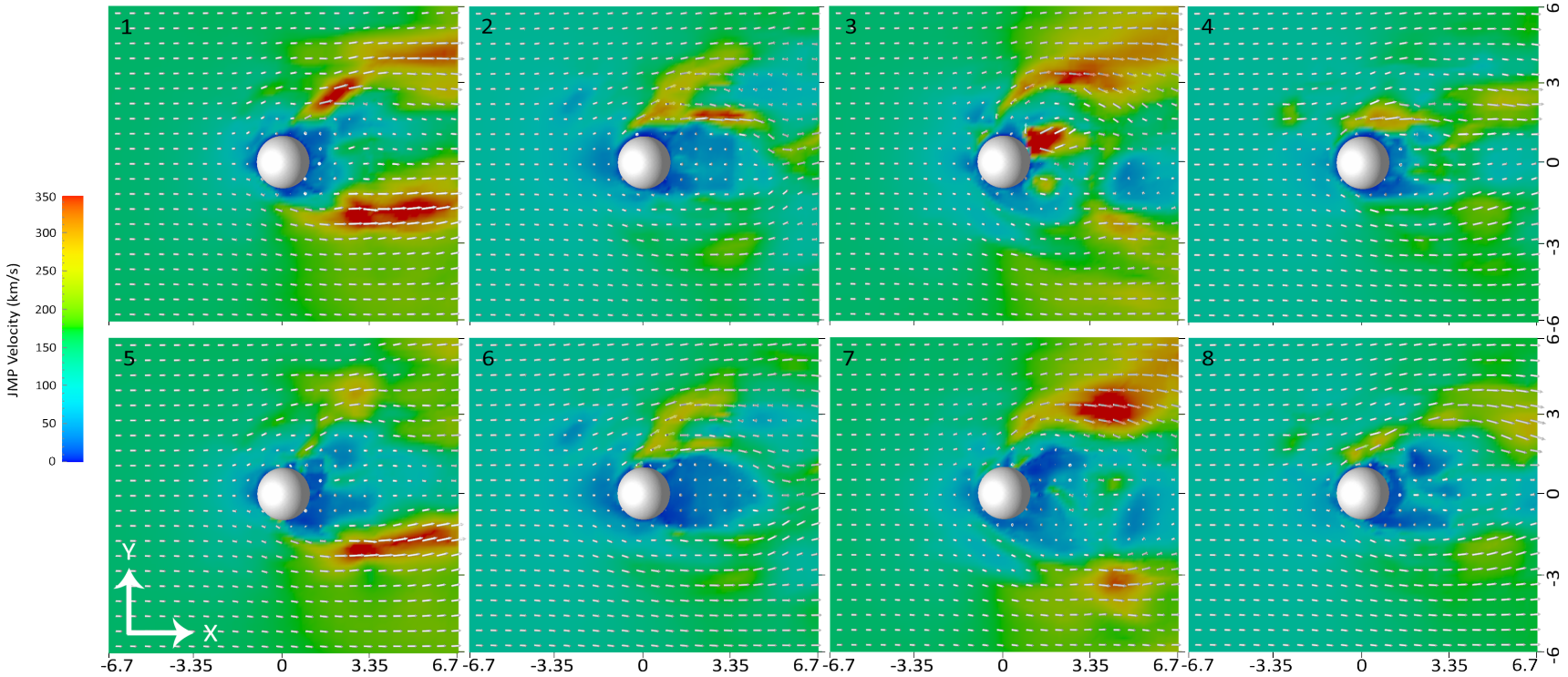

Figure 6.2: Velocity vector fields for JMP are shown for each case in the XY plane.

orbit around Jupiter. The cases which have been simulated here were chosen in order to be representative of the plasma conditions around Europa at different locations within Jupiter's magnetosphere – see Subsection 4.2.2 for more details about the choice of parameters at each location – so that the role that Europa's passage through the Jovian magnetosphere plays on its interaction with said magnetosphere could be explored.

As can be seen in Figures 6.1 and 6.2, the interaction changes appreciably between the various magnetospheric positions that Europa can occupy. In cases E.1.1, E.1.3, E.1.5, and E.1.7 there is mirroring of regions of enhanced Jovian magnetospheric plasma velocity across the XY plane. This is a result of the reversal in the direction of the significant Y component of the background magnetic field between cases E.1.1 & E.1.5 and cases E.1.3 & E.1.7.

Cases E.1.1, E.1.3, E.1.5, and E.1.7 (positions A and C within the magnetosphere) differ from cases E.1.2, E.1.4, E.1.6, and E.1.8 (positions B and D) in that the peak magnetic field strength of the region near Europa is significantly higher in the former. This is a result of the large time varying Y component of the background magnetic field which is present in these cases but not in the others. A slight asymmetry in the ionospheric species can be seen in cases E.1.2, E.1.4, E.1.6, and E.1.8 in Figure 6.3, which is caused by pickup ion gyromotion. It is far less pronounced than the asymmetries present with the simulations of the Pluto-Charon system because of the differences in the gyroradii of pickup ions between the two systems (0.045 R_E vs 253 R_P).

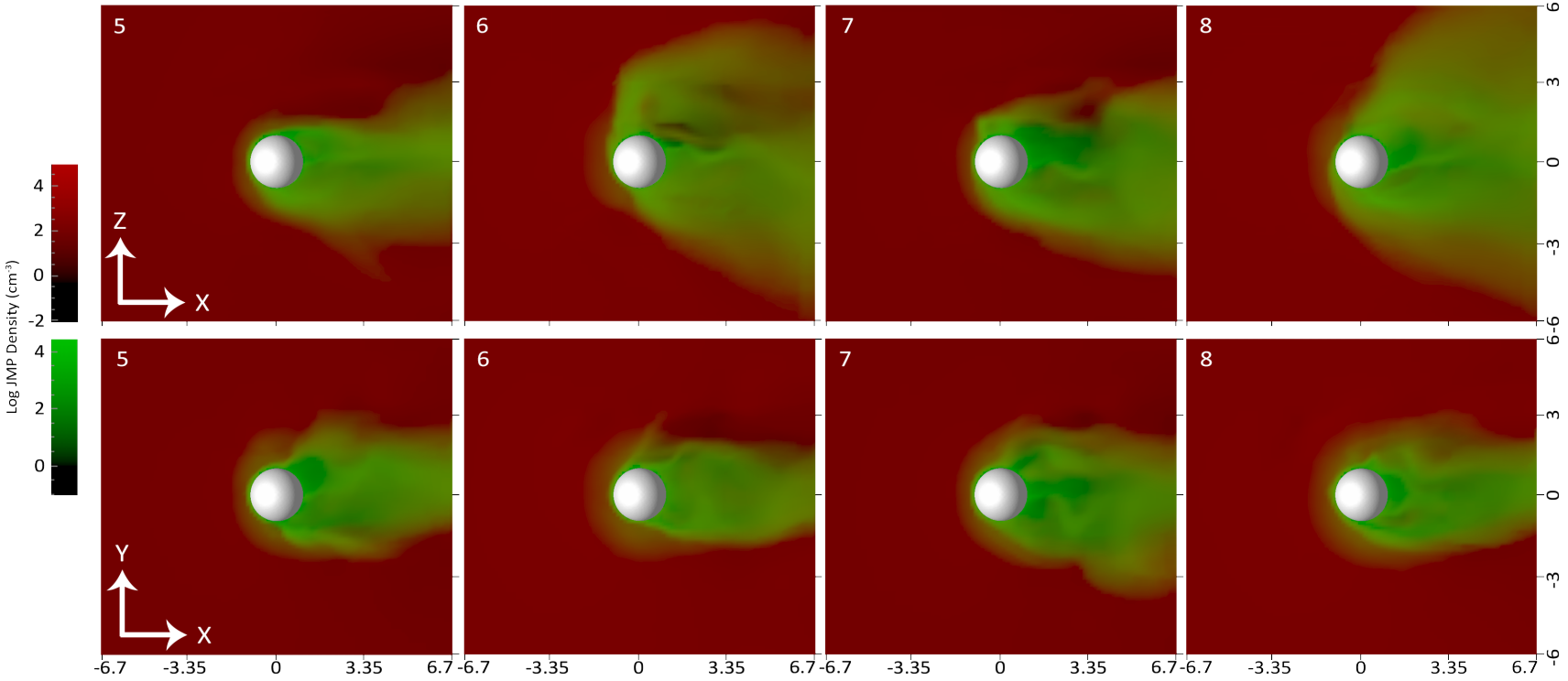

Figure 6.3: Densities for each species are shown in the XY and XZ planes for cases E.1.5 through E.1.8. Colors correspond to different species, with opacity indicating density. Red is JMP and green is O_2^+ from Europa's ionosphere.

Case	$O_2^+ s^{-1}$
E.1.5	4.66×10^{26}
E.1.6	4.15×10^{26}
E.1.7	5.34×10^{26}
E.1.8	6.00×10^{26}

Table 6.1: Integrated ionospheric loss rates for cases E.1.5 through E.1.8. Values were calculated at a distance of 4 R_E downstream from Europa.

6.2 Atmospheric Mass Loss

As plasma is generated through the ionization of neutral particles within the Europan exosphere, this plasma is stripped from the body. This material loss is a result of newly created ions experiencing ion-cyclotron motion. While the electrons that are generated have very small gyroradii because of their extremely high charge to mass ratio and therefore do not experience net motion away from the location in which they were stripped from their parent particles, ions that are created within the ionosphere have relatively large gyroradii and, as a result, can be subjected to meaningful changes in magnetic field strength or direction. This causes ions to be picked up from the location in which they were created and move away from that location. Material is lost from the Europan ionosphere through this mechanism, as can be seen in Figure 6.3.

For each of the cases that we have simulated that included ionization processes within the system, we have calculated the rate at which ionospheric material is leaving the near Europa environment. These values can been seen in Table 6.1, in which the total flux of O_2^+ leaving the system at a distance of 4 R_E in the positive X direction is displayed. Varying the location and EST at which these integrated fluxes were measured did not significantly alter the recorded values. As can be seen, there are variations in the loss rates between

cases which use different system parameters, on the order of 30%

6.3 Ionosphere's Impact

6.3.1 Structural Effects

In the cases in which Europa has an ionosphere (E.1.5 through E1.8), the wake region behind Europa is significantly more depleted of Jovian magnetospheric plasma, as Figure 6.1 demonstrates. This is because of the larger obstacle to the flow of Jovian magnetospheric plasma that Europa presents when it possesses an ionosphere. The upstream facing hemisphere of Europa exhibits a lower peak magnetospheric plasma density and a thicker region of enhanced density in the cases with an ionosphere. The larger region over which the magnetospheric plasma fluid has to slow down and divert around the obstacle when there is an ionosphere explains this phenomenon. The flow of magnetospheric plasma also appears to be somewhat slower in the upstream region as well as less turbulent in these cases (Figure 6.2). The most significant difference between the magnetic field configuration in the cases in which Europa has a volumetrically sourced ionosphere and those in which it does not, is an increase in peak magnetic field strength in the various cases with an ionosphere, which can be seen in Figure 6.4. This effect could be another effect of Europa presenting a larger obstacle to the incident plasma fluid when it has an ionosphere, which causes greater draping of magnetic field lines around the body.

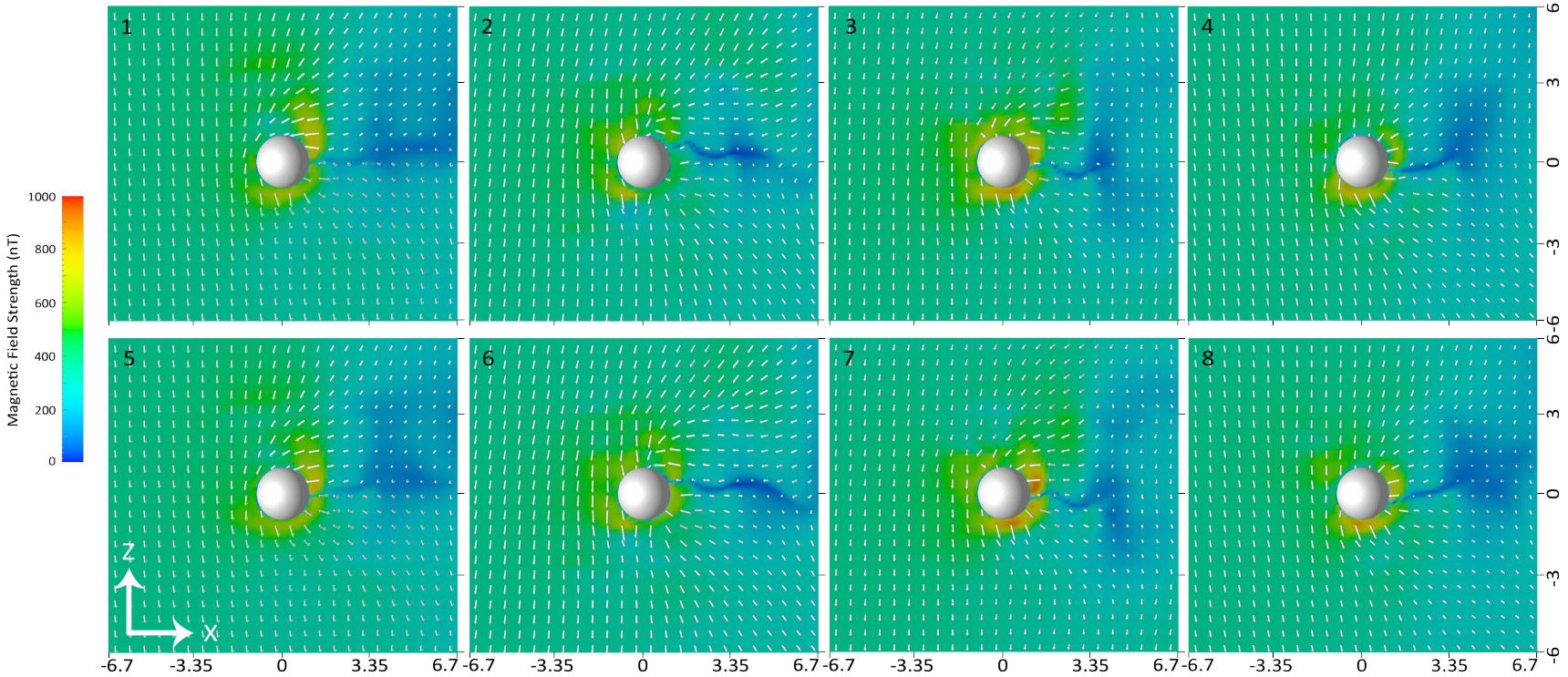

Figure 6.4: Magnetic field strength and direction are shown for each case.

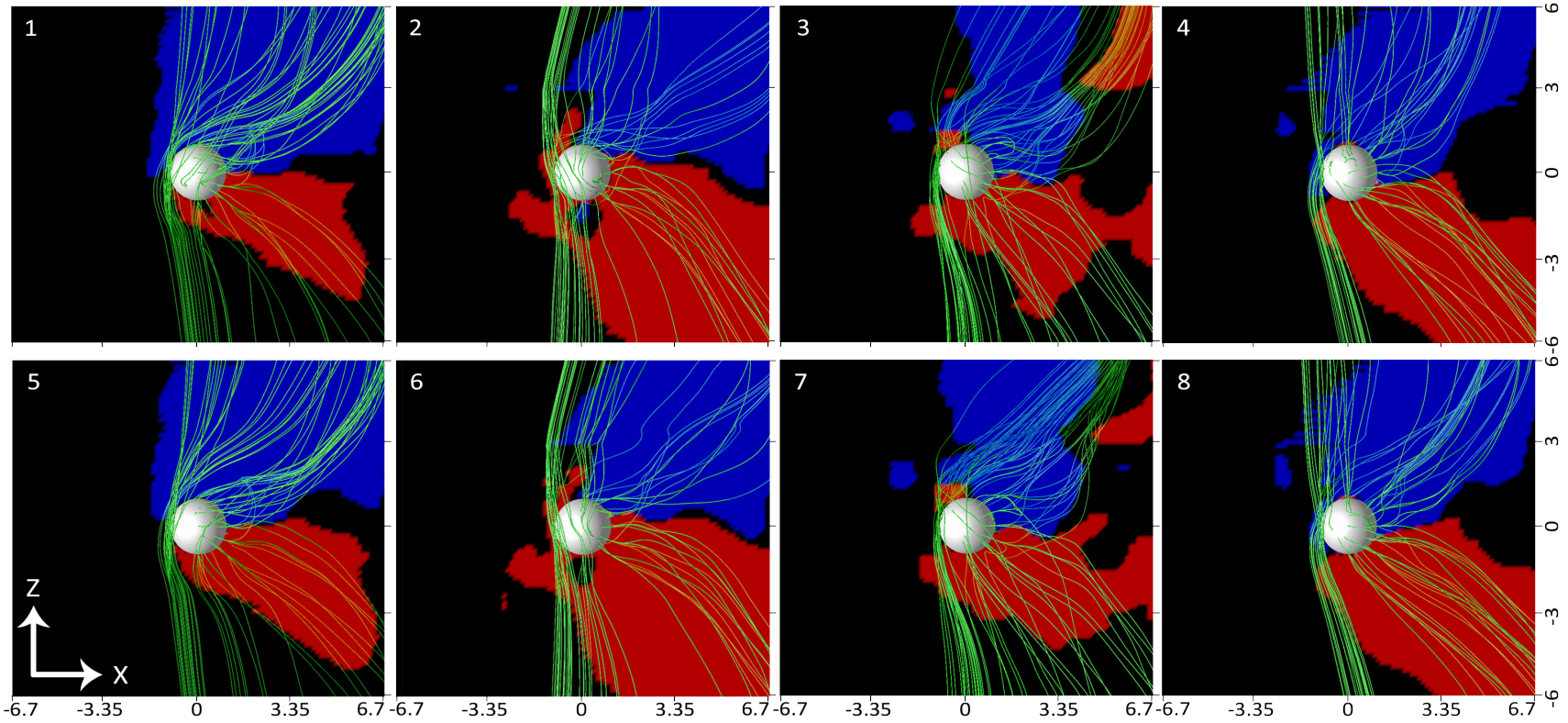

Figure 6.5: B_x color coded by whether it is a positive or negative value (Red is positive, Blue is negative). Background B_x is subtracted and small values are set to black in order to highlight the Alfvén wings.

6.3.2 Alfvén Wings

Alfvén wings are structures which are a result of standing Alfvén waves forming around a conducting obstacle to the flow of magnetized plasma within a system (Neubauer, 1998). They are characterized by regions of decreased flow speed above and below the conducting object along magnetic field lines that pass around the conducting object in question (see Vernisse et al. (2013) for an analysis of how conducting bodies interact with plasma flows in different Alfvén regimes). As magnetic field lines are carried by plasma when the frozen in condition holds, this wave exists farther downstream from the obstacle the farther above or below the obstacle is considered. The angle of the resulting wing structure is given by the following equation: $\theta = atan(\frac{v_{\text{flow}}}{v_{\text{A}}})$ (Pontius, 2002). This gives an angle of 25° for cases E.1.2, E.1.4, E.1.6, and E.1.8 (the cases in which there is not a significant Y-component to the background magnetic field).

Figure 6.5 shows plots of the X component of the magnetic field vector in order to show the presence or absence of Alfvén wings within the planes shown. Alfvén wings can be observed in each of the simulated cases, but due to the large B_y component of the background magnetic field when Europa is at large ϕ (cases A and C), the wing structure does not fall entirely within the planes shown in the figure for those cases. It is somewhat difficult to ascertain an exact angle for the wings, due to the amount of turbulence present, but by looking at the main body of the structures, it is reasonable to conclude that the angle of the Alfvén wings relative to the Z direction is fairly close to the value of 25° that was calculated. Volwerk et al. (2007) report that Alfvén wings are shrunken and shifted in the Y direction (radially in or out from Jupiter) as predicted by Neubauer (1999). Subsequent

work will attempt to reproduce this result.

6.4 Validation of Results

This initial study of the Europan interaction with the Jovian magnetosphere has focused on how the position of Europa affects its interaction with the greater magnetosphere as well as what contributions the ionosphere and the induced dipole make. Comparisons between simulations to understand the potential extent of the exospheric contribution to the plasma dynamic interaction enabled us to place upper limits on these effects, but more work is required to enable detailed and direct comparison for conditions relevant to individual encounters of the Galileo spacecraft with Europa. It is therefore also challenging to compare the results of this work to other modeling efforts, given the different parameter spaces explored. The most obvious comparison that can be made is between the ionospheric loss rates that were reported in Section 6.2 and those that have been calculated by others. The mean of the values for flux that was calculated for cases E.1.5 through E.1.8 was 5.0×10^{26} $O_2^+ s^{-1}$ or 26.6 kg/s. This is compared to values of 3.75 kg/s and 5.14 kg/s reported by Kabin et al. (1999) and Rubin et al. (2015) respectively, which is close enough that much of the discrepancy can reasonably be explained by differences in plasma parameters. Other possible contributors to the differing values include exact methods of calculating ionization rates. Work is currently underway to implement the magnetic boundary condition for non-conducting bodies that has been developed by Duling et al. (2014) within the Icy Bodies Model. This boundary condition treats the interaction between a magnetoplasma and non-conducting, icy bodies in a more physically accurate way than the current implementation and, as a result, we expect that simulations performed once it is fully implemented will

have even greater fidelity (see Subsection 7.2.4 for further details).

CHAPTER 7

CONCLUSIONS AND FUTURE WORK

7.1 Conclusions

7.1.1 Pluto-Charon System

The location of Charon within the system altered the interaction with the solar wind in several ways. In the case in which Charon has an ionosphere and is upstream of Pluto (case P.1.5), the formation of a complete bow shock is prevented and the gross structure of the interaction between the solar wind and Pluto is clearly altered. Side effects of this alteration include changes to the trajectory of heavy pick up ions sourced from Pluto. The impact of Charon being upstream without an ionosphere (case P.1.4) is less than with an ionosphere, but it is still non-negligible. Because Charon is mainly acting as a plasma absorber in this case, it can only have an effect as a result of several factors conspiring together: Charon's uniquely large size relative to the system it is in, its close orbital distance, supersonic, super-Alfvénic upstream flow, and Pluto's bow shock forming close to Pluto as a result of an atmosphere that is more compact than predicted. Both cases P.1.4 and P.1.5 show evidence for Charon shielding Pluto from atmospheric stripping while it is upstream of Pluto's bow shock. When Charon is downstream of Pluto, its impact on the system is more muted. With that said, in both the case of an ionosphere and the case of no ionosphere, Charon increases flow complexity in Pluto's wake and alters the path of the plasma sheet. A geometric wake in the plasma escaping from Pluto was observed in cases P.1.2 and P.1.3, indicating that material is being deposited on Charon, which is consistent with discoloration

observed on Charon's polar regions. Based on these results we expect the Pluto-Charon plasma environment to be highly dynamic, independent of fluctuations in upstream solar wind conditions as a result of Charon's orbital motion.

SWAP measurements taken during the New Horizons encounter with the Pluto-Charon system indicate that solar wind density and, to a lesser extent, velocity were higher than predicted at 0.025 H^+/cm^3 (2.5 times the simulated value) and 403 km/s (1.06 times the simulated value) (Bagenal et al., 2016; McComas et al., 2009). This suggests that the bow shock at the time of the encounter would be more compressed than the results presented in this work indicate, but this is not expected to qualitatively change Charon's effects on the system. Encounter measurements also indicate that the dominant escaping species is not N_2 as was expected, but is rather CH_4 (Gladstone et al., 2016). Follow up work was performed in which solar wind conditions matched those that existed at the time of the encounter, CH_4^+ was the dominant ion species, and ion-neutral interactions were treated, creating dynamic volumetric plasma sources within the simulation domain. These simulations allowed for comparison against conditions for which results could be corroborated with data. The results of these simulations match well against analysis of encounter data, with the bow shock standoff distance matching encounter estimates almost exactly, while also being compatible with the results of the first investigation.

7.1.2 Europa System

Europa's position within the Jovian magnetosphere plays a significant role in the moon's interaction with its surrounding plasma environment. Variations in the strength and direction of the time varying component of the Jovian background magnetic field, as well as the

lower density of Jovian magnetospheric plasma in the regions above and below the plasma sheet cause changes in the velocity structure of Jovian magnetospheric plasma flowing past Europa, alterations to the formation and orientation of Alfvén wings above and below Europa, and changes to the strength and direction of the induced dipole generated within Europa's subsurface saline ocean. Similarly, the presence of an ionosphere around Europa modifies its interaction with the magnetosphere in multiple ways. These include decreased peak magnetospheric plasma densities upstream of Europa as well as wake regions downstream of Europa that are even further depleted than when Europa is without an ionosphere. Additionally, flow around the body is less turbulent when an ionosphere is present. While these results are merely the result of an initial exploratory study into Europa's interaction with its local plasma environment and refinements can be made, they suggest that the topic merits more extensive investigation, particularly in light of the planned Europa Clipper mission.

7.2 Future Work

In addition to the improvements to and applications of the Icy Bodies Model previously described, there are various avenues for future investigations with the model, as well as refinements that could be made to it. Here we describe several that are either already in work or that we plan to pursue in the longer term.

7.2.1 Dynamic Upstream Conditions

All work that has been done with the Icy Bodies Model so far has been exclusively concerned with system behaviors when input parameters are in a steady state. This is a valid

approach due to the extremely short time scales which are relevant to plasma modeling. Many variations to system parameters take place over a large number of plasma transit times, meaning that at any given time, they can be considered to be constant for the purposes of plasma modeling. However, this effective constancy of input parameters does not always hold true for the plasma population flowing into the local system. Rapid variations in upstream plasma conditions are entirely normal, both for objects such as Pluto and Charon, which are directly exposed to the solar wind, and for objects such as Europa, which are embedded within the magnetosphere of a parent body.

For bodies that are within the solar wind, significant changes to upstream flow conditions occur on a timescale of days (Bagenal et al., 2015b). This is far longer that the transit time of plasma through the system of any small body ($\sim$500 seconds in the case of Pluto). It is therefore appropriate to treat these changes to upstream flow conditions as permanent rather than transient for the purposes of plasma modeling once they have occurred. This means that what is of interest is the behavior during and immediately after the change in conditions, rather than the effect that the event has on some theoretical baseline condition. As was discussed in Subsection 2.2.3, the solar wind parameters measured by New Horizons during its encounter with the Pluto-Charon system varied significantly from what was expected based on historical data from Voyager II with solar wind density at 0.025 H^+cm^{-3} and with a speed of over 400 km/s. As was demonstrated by our follow work in cases P.2.1 and P.2.2, this change in upstream conditions likely goes some way in explaining the unexpectedly small interaction region observed during the New Horizons encounter with the system. This could be verified by dynamically changing upstream conditions within the Icy Bodies Model from what are thought to be typical solar wind conditions to those which

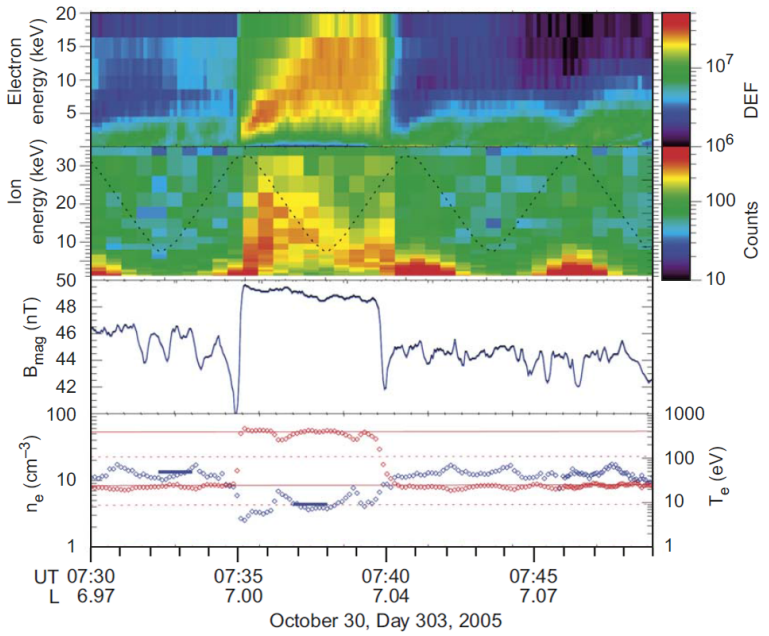

Figure 7.1: Example of a plasma interchange event. Spectrograms of electron and ion energy are shown, as well as magnetic field strength and electron number density. Event occurs between 7:35 and 7:40 on plots. Modified from A. M. Rymer et al. (2009).

were present during the encounter to see the response of the system.

An example of this variation within upstream plasma conditions within the inner magnetosphere of a giant planet is injection and dispersion events that have been observed at Saturn by the Cassini-Huygens spacecraft (Chen and T. Hill, 2008). These events within the Saturnian system have even been successfully modeled by a variant of the Icy Bodies Model, as demonstrated by Rajendar (2015). While it would not be efficient to model the entire Kronian or Jovian system in order to provide dynamically generated upstream plasma parameters for use in smaller scale simulations of icy bodies within these magnetospheres, the Icy Bodies Model is able to vary upstream conditions in such a way that observed and modeled flows in the greater magnetosphere are accurately reproduced. In order to observe the response of the local system to transient changes to upstream plasma conditions, the model will be run until it reaches quasi-steady-state. Once this has occurred, upstream

conditions will be altered to simulate an event such as a plasma injection. Once the event has ended, which would be after ∼300 seconds in the example of an interchange event (see Figure 7.1), upstream plasma parameters will be reverted to initial conditions. This will allow effects of a single event to be studied in isolation. Further investigations could introduce periodic upstream flow variations in an effort to account for hysteresis within the system.

7.2.2 Comparison of Synthetic Spectra

We have in several places within this document used data collected by various instruments to provide input parameters to and validation of the Icy Bodies Model. We have also shown traces of data (such as particle densities and magnetic field values) generated by our model as well as others in order to more clearly show radial structure of the plasma environment near Pluto. We have not, however, performed direct comparisons between the energy distributions of plasma populations within our model and measurements taken by spacecraft instruments. To address this, we are developing processing capabilities which will enable the creation of synthetic spectra based on model outputs. This will be done based on dividing the total particle density at a location in the model between energy bins based on the Maxwell-Boltzmann distribution assumed by MHD theory. These bins will have to be defined based on the design of individual instruments, which are customized as a result of different considerations such as the anticipated environment which is to be studied and constraints such as the mass, power, and budget limitations of the host mission. Furthermore, each plasma spectrometer has different observation directions and coverage. Often, a plasma spectrometer will have multiple anodes, each with a different look direction. It

is also possible that some of these anodes will be partially blocked by the structure of the spacecraft, decreasing their particle detection rate. The process for producing synthetic spectra from model data must therefore compare bulk plasma flow direction against the instrument's ability to observe said flow and adjust the synthetic count rates appropriately. This non-uniformity of instrument design makes it necessary to create data processing capabilities which can take in formatted instrument information and generate appropriate spectra without further user involvement. The challenges of reproducing spacecraft instrument spectra are actually part of the reason that they are worth producing. A model is a cohesive and self-consistent approximation of what is happening within a system. Instrument measurements reflect reality but have imperfect coverage. If synthetic spectra created from the output of a model match instrument measurements well, the model data that have to be discarded in order to obey the limitations of the instrument are likely to correspond to information from the actual system that the instrument simply could not capture. Synthetic spectra can therefore help fill in gaps caused by the realities of instrument design.

Another consideration that must be made when generating synthetic spectrograms is that spacecraft take a relatively long period of time to traverse a system compared to incident plasma. In the case of the New Horizons spacecraft, which was traveling at a speed relative to the Pluto-Charon system of $\sim$14 km/s, this means that the spacecraft took almost 30 plasma transit times to pass through the system. Therefore, it would be very computationally expensive to capture model data along the spacecraft trajectory in real time. A more tractable technique, and the one that we intend to use, is to perform multiple simulations using different parameters in parallel, generate instantaneous spectrograms along the trajectory, then look for similarities within temporal slices of the spectrogram, rather than

the whole spectrogram. In this way, we can test for changes in the system during the New Horizons encounter. In contrast, it might be reasonable to capture data in real time for data near bodies within giant planet magnetospheres due to the smaller region of interest.

7.2.3 Particle Tracking

One limitation of the multifluid MHD approach to plasma modeling is that it is often not possible to incorporate hot subpopulations of particles into the simulation as a separate fluid. One reason for this is that these subpopulations are not dense enough to behave in the fluid limit. As a consequence, phenomena that are caused by trace populations of very energetic particles within a system cannot be self-consistently reproduced in a multifluid MHD simulation. This is unfortunate, as several of these phenomena are in locations for which it is very difficult to send a spacecraft to take in situ measurements, but are remotely observable. An example of such a phenomenon is the asymmetry of auroral strength at Europa's poles, which is coincides with which pole is facing towards or away from the Jovian plasma sheet when Europa is either above or below the sheet. This is consistent with there being a higher concentration of high energy electrons moving along magnetic field lines away from the plasma sheet than towards it (due to losses within Jupiter's atmosphere) (Roth et al., 2016). In order to reproduce this effect, we will inject particles into data cubes generated by the model and track their motion in order to see how significant of a disparity in the density of hot electrons is necessary to reproduce the observed auroral asymmetries.

7.2.4 Implementation of New Physics within the Model

There are several opportunities to enhance the capabilities of the Icy Bodies Model so that it can more accurately simulate magnetoplasma interactions with icy bodies. The first improvement that will be implemented is a version of the inner magnetic boundary conditions described by Duling et al. (2014). The Duling boundary conditions, referred to as the insulating boundary method, were developed in order to accurately treat non-conducting bodies, which due to their lack of surface conductivity, have zero radial electric current penetrating their surfaces and therefore the radial component of the magnetic field curl must also be zero. The insulating boundary method works by transforming the magnetic field just above the surface of the body into poloidal and toroidal components, as the toroidal component must be zero at the surface of the body. The boundary condition for the poloidal components is a radially dependent first-order differential equation, which is easily implemented. The magnetic field is then transformed back to real space afterwards to complete the operation. This method is compatible with the implementation of intrinsic and induced internal magnetic fields within the body, with Duling et al. (2014) demonstrating its utility for modeling the Ganymede environment. This means that the insulating boundary method can be used in any body which has a non-conductive surface, regardless of interior structure, making it suitable for modeling efforts at bodies such as Europa which have internally sourced, but exteriorly driven magnetic fields. Implementation of the insulating boundary method should be beneficial to our efforts to separate Europa's induced dipole's impact on the local plasma interaction from that of the Europan ionosphere.

Another enhancement that could be made to the model that would be useful in certain

situations would be to implement pressure anisotropy within the model. This could be useful in simulating bodies within the the magnetospheres of the outer planets, as plasma pressure anisotropies have been observed within the plasma sheets of both Saturn (Kellett et al., 2010) and Jupiter (Krupp et al., 2001). As a result, even when modeling the plasma environment of icy moons of the giant planets, the ability to accommodate pressure anisotropy within the model could have merit, as incident plasma flowing into the system has pressure anisotropies because it is derived from the plasma sheet of the giant planet's magnetosphere. Furthermore, the ability to implement pressure anisotropy within the framework of the Icy Bodies Model has been demonstrated by Tilley et al. (2015), using a closely related model to investigate pressure anisotropies within the Saturnian magnetosphere. While implementation of pressure anisotropy within the icy bodies model should therefore be possible, it would necessarily be worthwhile to employ in all situations due to the greater computational cost involved in tracking and manipulating the additional terms implied by treatment of the full pressure tensor for multiple ions fluids.

7.2.5 Application to Other Bodies

The Icy Bodies Model is widely applicable to different bodies both within and outside of the solar system, as shown by its use, or the use of its close relatives, at an ever expanding list of objects. An obvious object to study with he model next would be Triton, which is similar to Pluto in size and composition but, due to its location within Neptune's magnetosphere, exists within a vastly different plasma environment. In fact, due to the large tilt (47°) and significant offset from the center of the planet ($\sim$0.55 R_N) of Neptune's magnetic dipole, Triton is being subjected continually to significant magnetic field variations

as well as probable regular changes in incident plasma population. Combined, these facts make Triton a promising subject for the investigations into the effects of dynamic upstream conditions discussed in Subsection 7.2.1.

Another body that might be gainfully investigated with the model is Ceres. As a small, icy body, it's characteristics match well with the design goals of the model. Additionally, recent observations by the Herschel Space Observatory, as reported by Küppers et al. (2014), are indicative of a transient vapor atmosphere. We could therefore compare behavior at the body when it is without an atmosphere to times when it has a transient atmosphere. Not only would this be in keeping with our previous work with the Icy Bodies Model, it would also allow for comparison with recent work by Y.-D. Jia et al. (2017), who have provided constraints on the transient atmosphere's values based on hot electron measurements made by the Dawn spacecraft.

The final example that we will mention of an object that could be studied with the Icy Bodies Model, but not the only body that could be studied with it, is a comet in the inner solar system. In this case, the solid body, consisting of the comet's nucleus, is inconsequential in size (no comet with a nucleus larger than 100 km has been observed in the inner solar system), so the obstacle to the solar wind would be comprised solely of the cometary coma, composed of material outgassing from the nucleus. The addition of neutral interactions to the model allow for treatment of such an obstacle. 67P/Churyumov–Gerasimenko would be the most obvious specimen to model, given the large dataset that has been accumulated about its environment by the Rosetta mission.

Appendices

APPENDIX A

SUPPLEMENTAL FIGURES

A.1 Expanded Plutonian Ionosphere

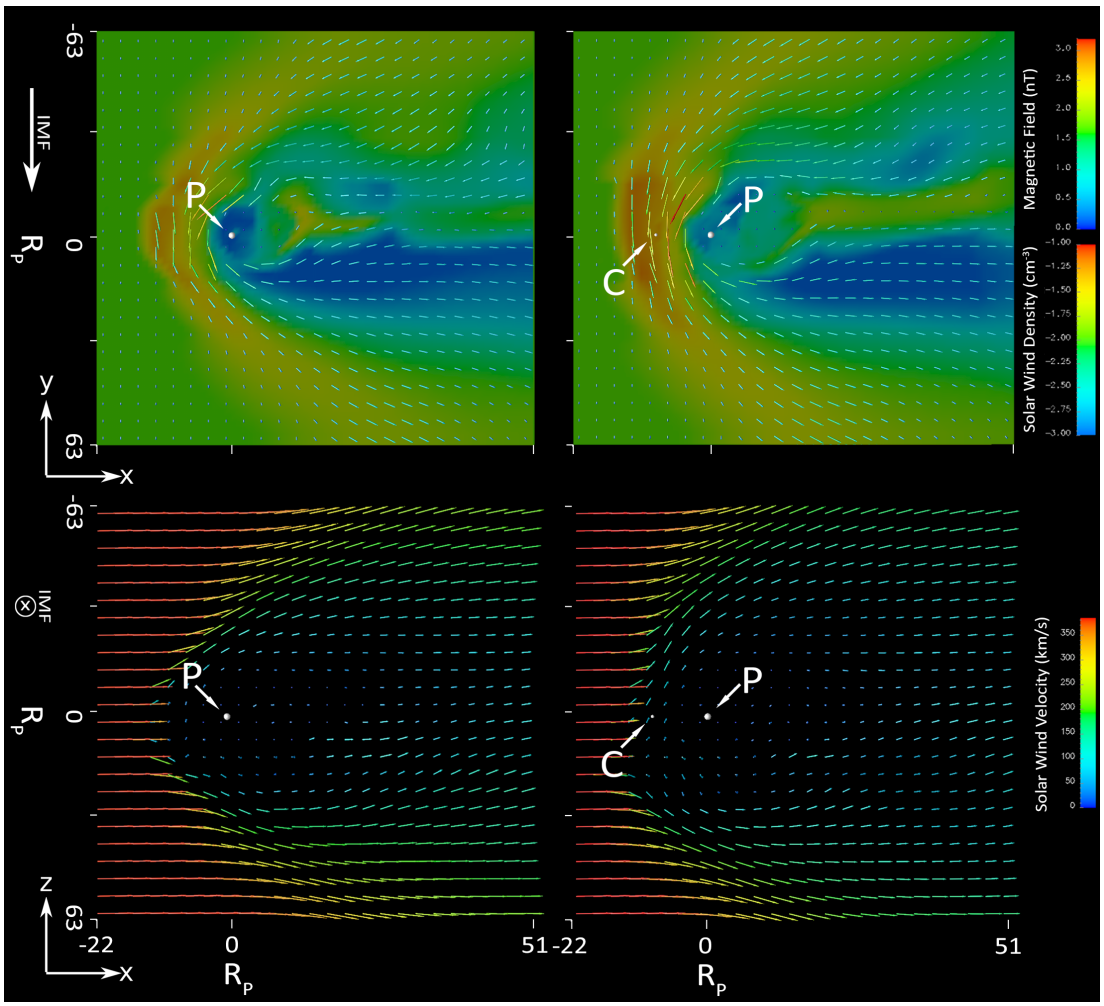

Figure A.1: Figure shows simulations in which Pluto's atmosphere is greatly expanded, as it was predicted to be before the New Horizons encounter. Top two panels are the solar wind density with magnetic field vectors overlaid. Bottom two panels are solar wind velocity. Panels on left are the system without Charon and panels on right have Charon directly upstream, with an ionosphere.

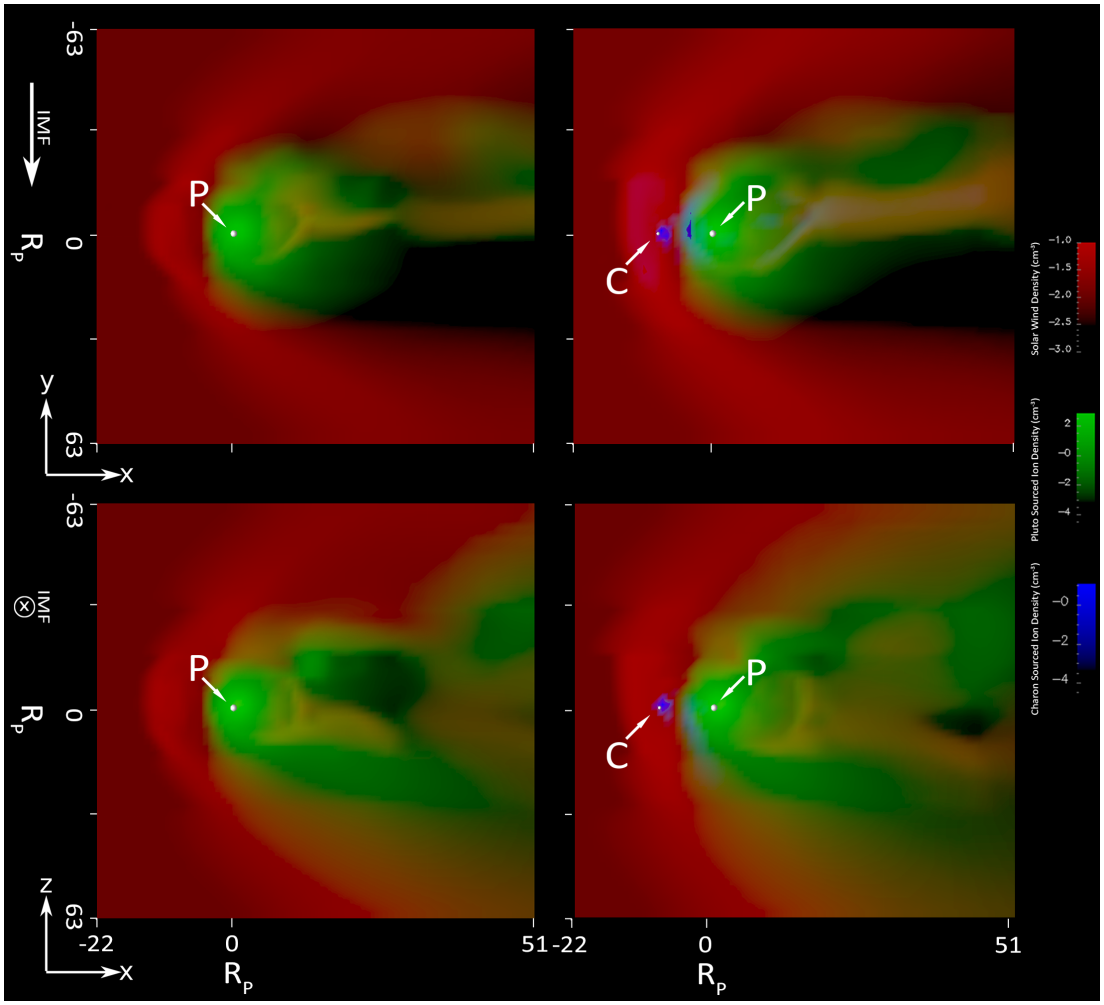

Figure A.2: Multispecies plots of simulations in which Pluto's atmosphere is expanded. Panels are organized as in Figure A.1.

A.2 Spacecraft Instruments

A.2.1 Europa Clipper Instruments

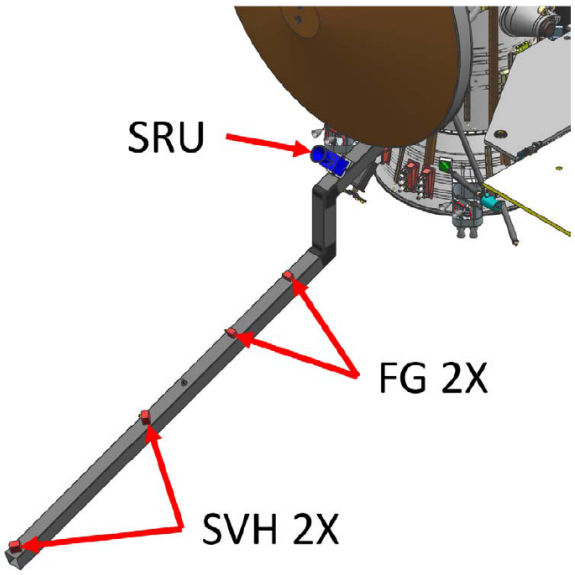

Figure A.3: Rendering of the Interior Characterization of Europa using Magnetometry (ICEMAG) instrument with TFGMs and SVHMs labeled from Horner et al. (2017). Different individual magnetometers are spread along boom in order to allow for detection of magnetic field gradients as well as to help with correction for magnetic noise from spacecraft.

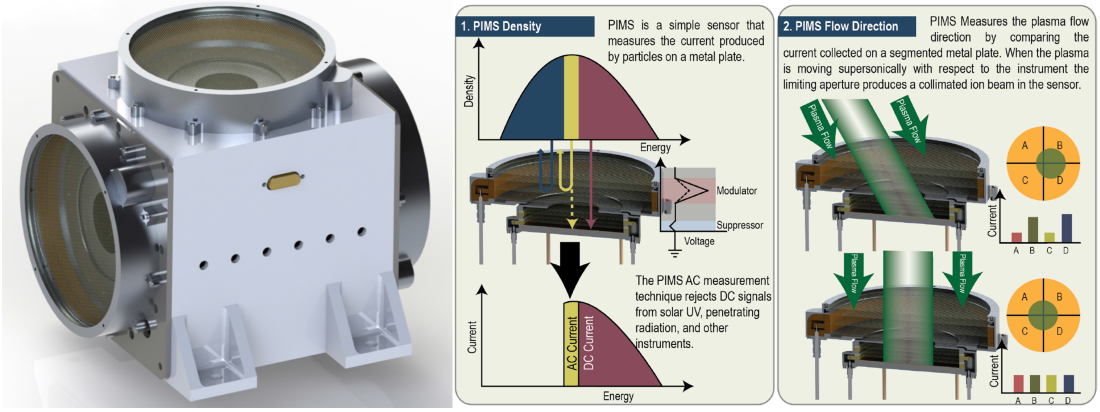

Figure A.4: (Left) Rendering of the Plasma Instrument for Magnetic Sounding (PIMS) instrument. (Right) Demonstration of operating method of instrument and basic capabilities. Modified from Westlake et al. (2016).

A.2.2 Galileo Instruments

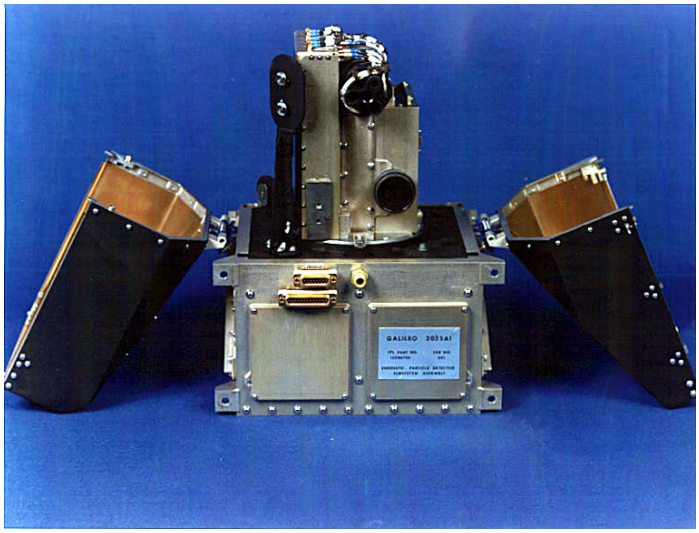

Figure A.5: The Galileo Energetic Particle Detector (EPD) used solid state detectors with a TOF capability in order to measure electrons and ions with energies greater than 20 KeV, from NASA. See Williams et al. (1992) for details of instrument operation.

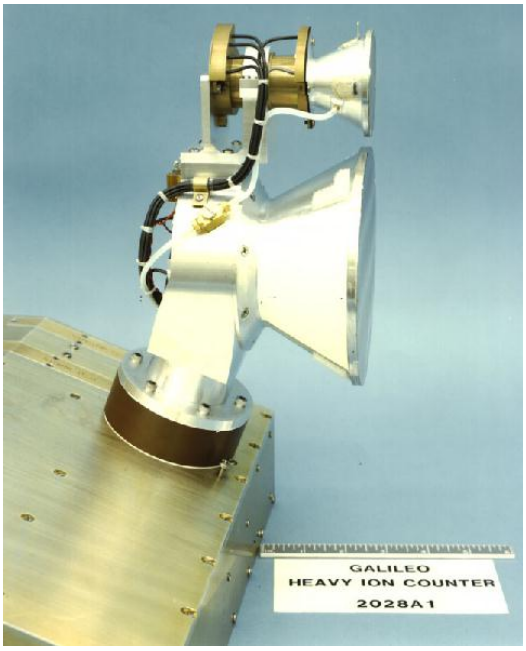

Figure A.6: The Galileo Heavy Ion Counter (HIC) detected very high energy particles using stacked crystal silicon wafers. An evolution of the Voyager Cosmic Ray System. From JPL.

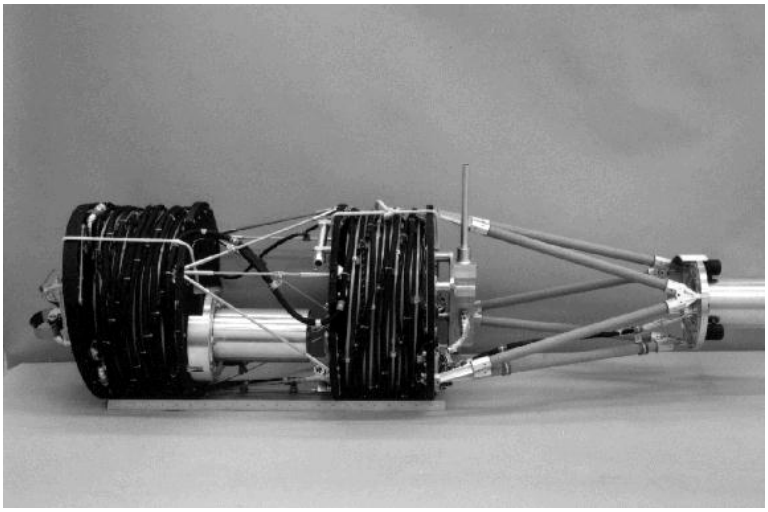

Figure A.7: The Galileo Magnetometer (MAG) used dual TFGMs. Shown with boom collapsed from NASA. For more information on the MAG instrument, see Kivelson et al. (1992).

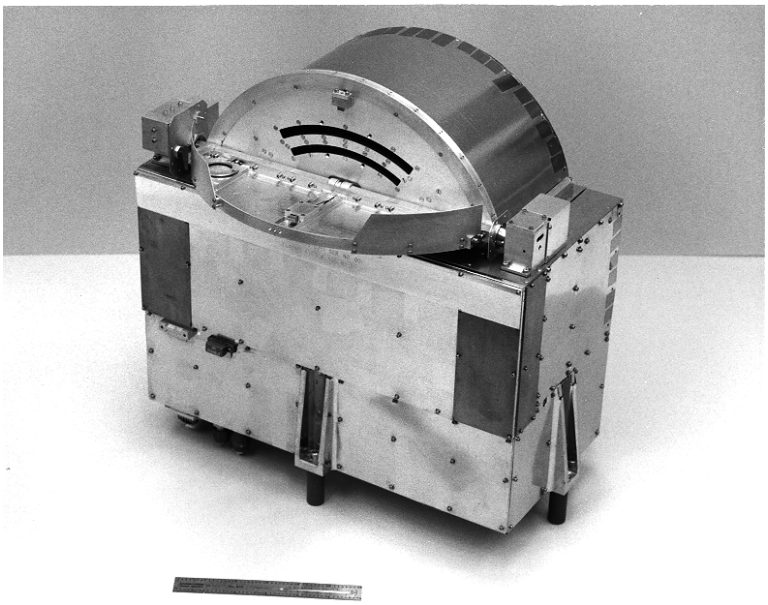

Figure A.8: Galileo Plasma Subsystem (PLS) is shown from LASP. Includes two electron electrostatic analyzers, two positive ion electrostatic analyzers, and three miniature mass spectrometers. Electrostatic analyzers are each composed of seven sensors. See Frank et al. (1992) for details of instrument operation.

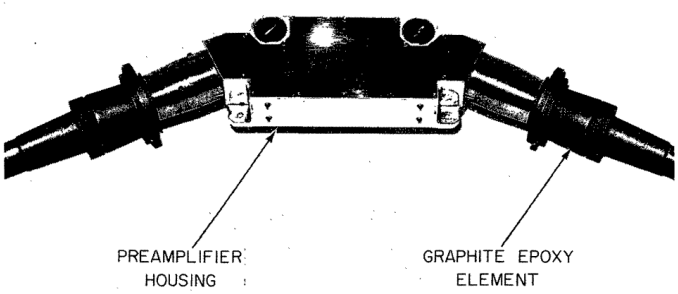

Figure A.9: Galileo Plasma Wave Subsystem (PWS) consists of two search coil magnetic antennas and one electric dipole antenna in order to measure plasma waves. Image from D. A. Gurnett et al. (1992).

A.2.3 New Horizons Instruments

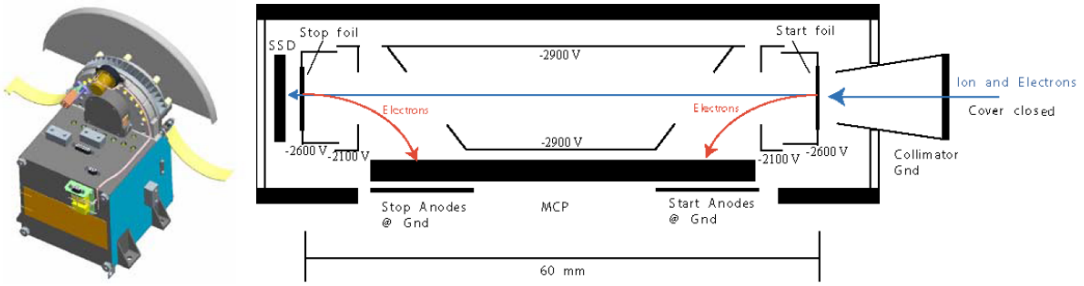

Figure A.10: (Left) Rendering of Pluto Energetic Particle Spectrometer Science Investigation (PEPSSI) (Right) Diagram showing method of operation. Modified from R. L. McNutt et al. (2008).

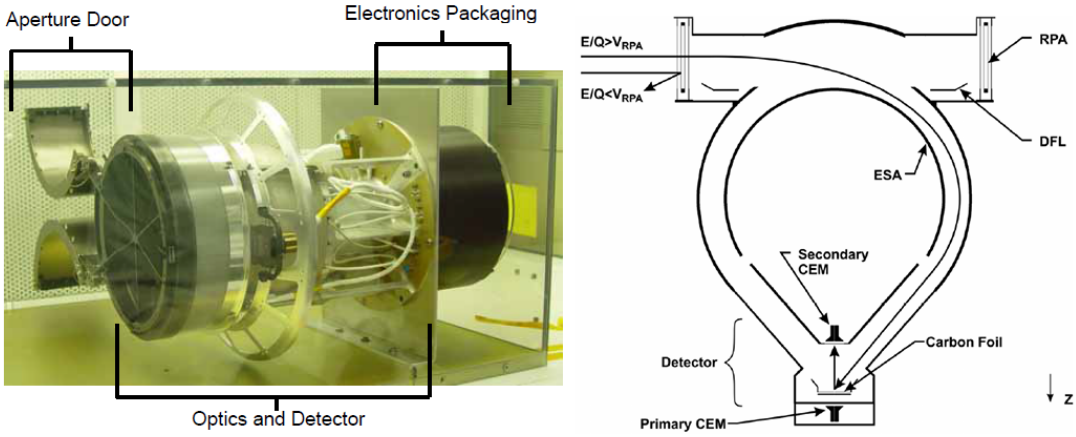

Figure A.11: (Left) Image of Solar Wind Around Pluto (SWAP) instrument (Right) Diagram showing method of operation. Modified from McComas et al. (2009).

A.2.4 Voyager Instruments

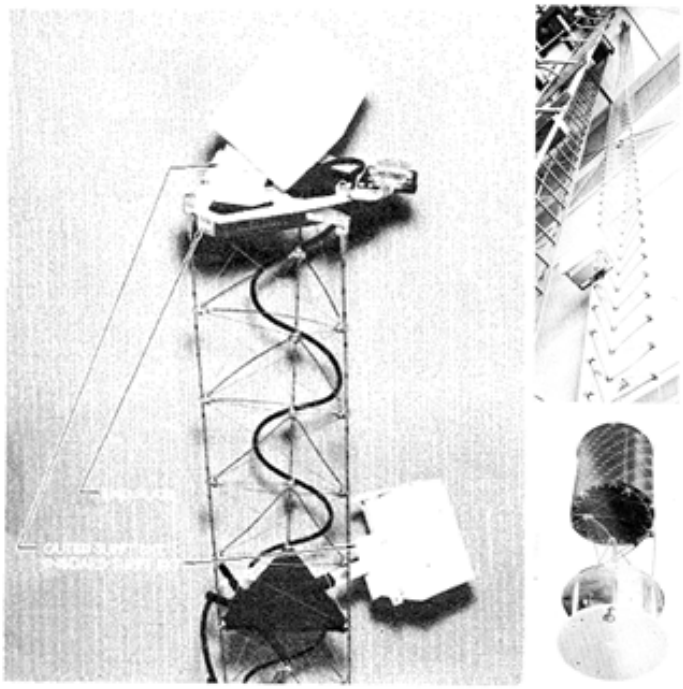

Figure A.12: (Left) Voyager magnetometer instrument mounting location on boom and (Right) the fully extended boom. Modified from Miller (1978).

Figure A.13: Voyager Plasma Spectrometer (PLS), which is composed of several Faraday cups pointing in different directions. Image from ESA. See Bridge et al. (1977) for details of instrument operation.

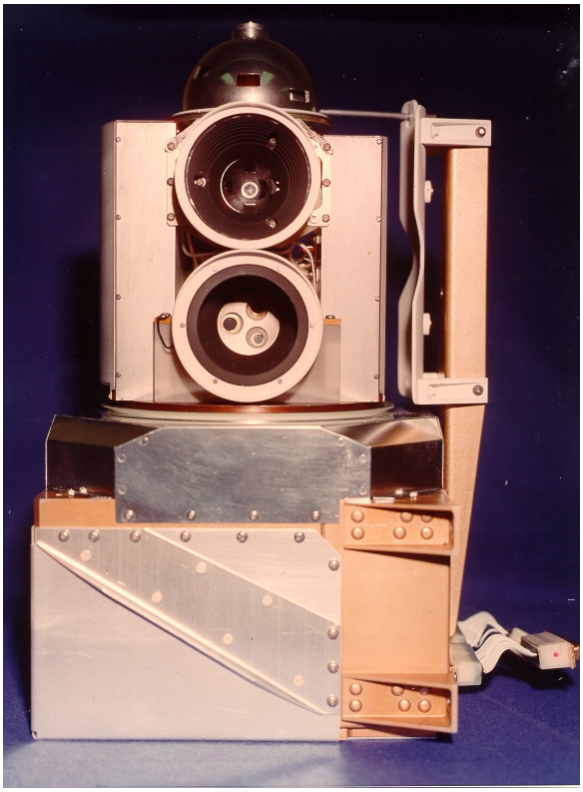

Figure A.14: Voyager Low-Energy Charged Particles Investigation (LECP), which is a series of CCD based charged particle detectors UC-LASP.

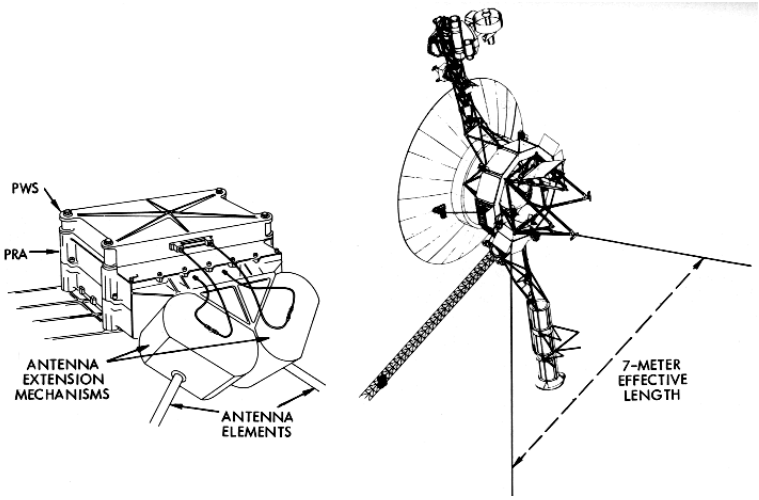

Figure A.15: Voyager Plasma Wave System (PWS), which uses radio receivers to detect plasma waves (Scarf and Donald A. Gurnett, 1977).

APPENDIX B

GUIDELINES FOR MAINTAINABLE CODE DEVELOPMENT

Academic codebases tend to be started and maintained by amateur developers working in an environment which does not clearly reward programming practices that are common in industry. This is because the creation of academic software often requires a high level of knowledge in the subject being studied with the software in question, meaning that those doing the development have been busy accumulating subject matter expertise rather than abstract programming skills. Furthermore, funding within academia is rarely provided with long term tool development in mind, resulting in a preference for rapid, rather than extensible and maintainable, implementation of new features. This incentivization of quick development is coupled with a tendency for research topics to organically evolve over time and causes the accumulation of what is known as technical debt. The natural consequence of this is the generation and extended use of software that is difficult to interpret, difficult to modify, and uneven in quality. While the realities of academic work make these issues impossible to fully eliminate, the following guidelines can help to minimize them without greatly increasing short term workloads, and can significantly reduce development time in the longer term.

B.1 Version Control

The most important change that a developer can make to their programming methods is to begin using version control software. Version control software keeps track of changes that have been made to the codebase at user-defined points in time, called “commits”. This

means that if issues arise in the implementation of new features, it is straightforward to determine when and where they started. This can be done by rolling back the state of the codebase until the problem is not present, then looking at what was done between the last working version of the program and the first non-functional version of the program. Often, the issue can be fixed and then subsequent changes can be automatically reapplied without the need to manually rewrite the code. This process is aided by the ability to write comments briefly describing what changed between commits. Additionally, "branches" can be made to allow for simultaneous work on multiple new features without uncertainty over whether problems are the result of problems within a newly developed feature or interactions between different new features. Once each branch's new feature is complete, the branch can be merged back into the main branch of the codebase. This can be particularly useful if the codebase is being actively developed by several people concurrently. Version control software can also aid in the distribution of updated versions of a codebase if only a subset of users take part in development of the codebase. This is done by having non-developing users create "clones" of the "repository" upon which development is performed. By using clones of the repository, updated versions of the codebase can easily be "pulled" from the repository whenever required. This distribution technique can substantially reduce the likelihood of problems arising from the use of out of date software.

B.2 Comments

Most developers, even the least experienced, know that they should write comments for their code. However, this activity is often put off until after a feature is implemented or not done at all. There are several reasons for this: 1) the developer does not think that comments

are necessary because they do not think that anyone else will ever look at the codebase, 2) the developer is making numerous revisions to the feature as they are implementing it and do not wish to revise the comments repeatedly during development, 3) the developer believes that writing comments during development slows them down and would rather deal with it after the fact. However, none of these arguments are strong because 1) it is difficult to predict who will need to further develop a codebase in the future, and even the original developer may have difficulty remembering what various sections of code do, given a long enough period of active development, 2) comments made during development can be cursory and be further refined or expanded after the fact, and 3) even the amount of time required to write inline comments after every line of code (a level of commenting that is highly unlikely to be necessary) would be minor compared to the amount of time needed to think out and correctly implement the code in the first place. Finally, it can be faster to write comments at the time because details of the code and motivations for design and implementation choices are fresh in the developers mind, meaning that less effort is needed to articulate them.

B.3 Modularity and Unit Testing

Features should be developed in such a way that they are self contained instead of being enmeshed within the rest of the codebase. There are several advantages to this. The most obvious benefit is that sections of code contained within a module, subroutine, or function can be easily referenced many times throughout the program, obviating the need to duplicate sections of code. This also means that if changes need to be made to the section of code, they only have to be performed once. Another merit of code modularity is that

interactions between the newly developed section of code and the rest of the codebase can be much more clearly defined, reducing possible sources of error. Modularity also allows for easier use of unit testing during development. Unit testing is a method for ensuring that newly implemented sections of code function as expected. This is done by providing representative inputs to the section of code and checking the output against expected results. Proper unit testing can reveal and aid in the preemptive elimination of failure modes within new sections of code. This is particularly useful for software development in which the program takes a significant amount of time to run (and therefore to fail).

B.4 Tool Choice

As has been previously mentioned, academic users and developers of software have little time to invest in learning new software. Therefore, it is important to consider different factors when choosing development and research tools. Necessarily, the first is how well suited the software is to the task required. If multiple options meet this first criterion satisfactorily, the next consideration should be ease of use. Given the choice between a tool that operates in a counterintuitive way or, worse, is unusually labor intensive to use, an alternative should be sought. The need for selecting tools based on these first two metrics is plain, but another that is less apparent is the current and long term viability of a tool. If an academic user is going to use a new tool, it is highly desirable that the software is either widely used, is contractually supported, or has a stable userbase. This is because there is a time investment involved in learning new software tools. However, this is not the only reason that new tools should have a reasonable chance of at least moderately long term viability. The other major reason is that academic users of software are prone to becoming

entrapped within an ecosystem of interconnected software applications that depend on each other to some extent. This can either be numerous pieces of third party software that are interoperable, or software that the academic user has created themselves that relies upon the tool that is chosen. Once this has occurred, the cost of transitioning away from the tool grows appreciably. Tools should therefore only be chosen when there is a some assurance that they will remain viable for a reasonable amount of time. It is also advisable that the user of a tool remains vigilant for signs that it is heading towards obsolescence so that there is enough time to find and transition to a new tool or tools before continued use of the current tool becomes untenable.

B.5 Naming

Choice of variable, subroutine, and function names can have a major impact on the readability of code and accordingly should be selected with care. Variable names should be at least somewhat indicative of what its contents are, meaning that arbitrary letters should never be used, unless the variable is within a function or subroutine that is inherently generic such as one that takes a cross product. Conversely, variable names should not be so verbose that they become ungainly to write within a line of code. If necessary, write a comment after the variable's declaration indicating its use. If numerous variables are related within the codebase, it might be useful to have a common element shared between them, so that it is immediately clear that a variable belongs to its group. Again, try to choose something that in some way describes the group. Similarly, subroutines and functions should be named so that it is obvious what is being done when they are called.

B.6 Magic Numbers

Magic numbers are arbitrary constants placed within a section of code that make the section of code function properly. They should be avoided whenever possible for the following reasons: the reason that they are the value that they are is rarely explained (is the number intrinsic to the operation of the program, or is it merely linked to the original use case?), they are often used in multiple locations which makes it possible that they are not the same in all locations, and their use makes updating the codebase more difficult. It is therefore better, almost without exception, to place the value within a named variable with an explanation of the value used.

REFERENCES

Anzai, K. et al. (2012). "Cross section data sets for electron collisions with H 2, O 2, CO, CO 2, N 2 O and H 2 O". In: *The European Physical Journal D-Atomic, Molecular, Optical and Plasma Physics* 66.2, pp. 1–8.

Bagenal, F. (1994). "Empirical model of the Io plasma torus: Voyager measurements". In: *Journal of Geophysical Research: Space Physics* 99.A6, pp. 11043–11062.

Bagenal, F., T. E. Cravens, J. G. Luhmann, R. L. McNutt, and A. F. Cheng (1997). "Pluto's interaction with the solar wind". In: *Pluto and Charon* 1, p. 523.

Bagenal, F. and Ralph L. McNutt (1989). "Pluto's interaction with the solar wind". In: *Geophysical Research Letters* 16.11, pp. 1229–1232.

Bagenal, F. et al. (2015a). "Plasma conditions at Europa's orbit". In: *Icarus* 261, pp. 1–13.

Bagenal, F. et al. (2015b). "Solar wind at 33 AU: Setting bounds on the Pluto interaction for New Horizons". In: *Journal of Geophysical Research: Planets* 120.9. 2015JE004880, pp. 1497–1511.

Bagenal, F. et al. (2016). "Pluto's interaction with its space environment: Solar wind, energetic particles, and dust". In: *Science* 351.6279. Ed. by G. R. Gladstone et al. eprint: http://science.sciencemag.org/content/351/6279/aad9045.full.pdf.

Banks, P. M. and G. Kockarts (1973). "Aeronomy (Part A), 430 pp". In: *Academic, New York*.

Bertucci, C., D.C. Hamilton, W.S. Kurth, G. Hospodarsky, D. Mitchell, N. Sergis, N. J. T. Edberg, and M. K. Dougherty (2015). "Titan's interaction with the supersonic solar wind". In: *Geophys. Res. Lett.* 42.2, pp. 193–200.

Blanc, M, R Kallenbach, and NV Erkaev (2005). "Solar system magnetospheres". In: *Space science reviews* 116.1-2, pp. 227–298.

Blöcker, Aljona, Joachim Saur, and Lorenz Roth (2016). "Europa's plasma interaction with an inhomogeneous atmosphere: Development of Alfvén winglets within the Alfvén wings". In: *Journal of Geophysical Research: Space Physics* 121.10, pp. 9794–9828.

Bridge, H. S., J. W. Belcher, R. J. Butler, A. J. Lazarus, A. M. Mavretic, J. D. Sullivan, G. L. Siscoe, and V. M. Vasyliunas (1977). "The plasma experiment on the 1977 Voyager mission". In: *Space Science Reviews* 21.3, pp. 259–287.

Brown, Michael E. (2001). "Potassium in Europa's atmosphere". In: *Icarus* 151.2, pp. 190–195.

Brown, Michael E. and Richard E. Hill (1996). "Discovery of an extended sodium atmosphere around Europa". In: *Nature* 380.6571, p. 229.

Buie, M. W., W. M. Grundy, E. F. Young, L. A. Young, and S. A. Stern (2006). "Orbits and photometry of Pluto's satellites: Charon, S/2005 P1, and S/2005 P2". In: *The Astronomical Journal* 132.1, p. 290.

Cassidy, T. A., P. Coll, F. Raulin, R. W. Carlson, R. E. Johnson, M. J. Loeffler, K. P. Hand, and R. A. Baragiola (2010). "Radiolysis and photolysis of icy satellite surfaces: experiments and theory". In: *Space science reviews* 153.1, pp. 299–315.

Cassidy, T. A., R. E. Johnson, P. E. Geissler, and François Leblanc (2008). "Simulation of Na D emission near Europa during eclipse". In: *Journal of Geophysical Research: Planets* 113.E2.

Cassidy, T. A., R. E. Johnson, M. A. McGrath, M. C. Wong, and J. F. Cooper (2007). "The spatial morphology of Europa's near-surface O 2 atmosphere". In: *Icarus* 191.2, pp. 755–764.

Cassidy, T. A., R. E. Johnson, and O. J. Tucker (2009). "Trace constituents of Europa's atmosphere". In: *Icarus* 201.1, pp. 182–190.

Cassidy, T. A., C. P. Paranicas, J. H. Shirley, J. B. Dalton III, B. D. Teolis, R. E. Johnson, L. Kamp, and A. R. Hendrix (2013). "Magnetospheric ion sputtering and water ice grain size at Europa". In: *Planetary and Space Science* 77, pp. 64–73.

Chashei, Igor V and Hans J. Fahr (2014). "On solar-wind electron heating at large solar distances". In: *Solar Physics* 289.4, pp. 1359–1370.

Chen, Y and TW Hill (2008). "Statistical analysis of injection/dispersion events in Saturn's inner magnetosphere". In: *Journal of Geophysical Research: Space Physics* 113.A7.

Cook, J. C., Steven J. Desch, T. L. Roush, C. A. Trujillo, and T. R. Geballe (2007). "Near-Infrared Spectroscopy of Charon: Possible Evidence for Cryovolcanism on Kuiper Belt Objects". In: *ApJ* 663.2, pp. 1406–1419.

Cooper, John F., Robert E. Johnson, Barry H. Mauk, Henry B. Garrett, and Neil Gehrels (2001). "Energetic ion and electron irradiation of the icy Galilean satellites". In: *Icarus* 149.1, pp. 133–159.

Cravens, T.E. and D.F. Strobel (2015). "Pluto's solar wind interaction: Collisional effects". In: *Icarus* 246, pp. 303–309.

Delamere, P. A. (2009). "Hybrid code simulations of the solar wind interaction with Pluto". In: *J. Geophys. Res.* 114.A3.

Delamere, P. A. and F. Bagenal (2004). “Pluto’s kinetic interaction with the solar wind”. In: *Geophysical research letters* 31.4.

Delamere, P. A., F. Bagenal, and A. Steffl (2005). “Radial variations in the Io plasma torus during the Cassini era”. In: *Journal of Geophysical Research: Space Physics* 110.A12.

Desch, S. J. and M. Neveu (2017). “Differentiation and cryovolcanism on Charon: A view before and after New Horizons”. In: *Icarus* 287, pp. 175–186.

Duling, Stefan, Joachim Saur, and Johannes Wicht (2014). “Consistent boundary conditions at nonconducting surfaces of planetary bodies: Applications in a new Ganymede MHD model”. In: *Journal of Geophysical Research: Space Physics* 119.6, pp. 4412–4440.

Earle, Alissa M., Richard P. Binzel, Leslie A. Young, S. A. Stern, K. Ennico, W. Grundy, C. B. Olkin, H. A. Weaver, et al. (2017). “Long-term surface temperature modeling of Pluto”. In: *Icarus* 287, pp. 37–46.

Elliot, J. L., E. W. Dunham, A. S. Bosh, S. M. Slivan, L. H Young L. A. and. Wasserman, and R. L. Millis (1989). “Pluto’s atmosphere”. In: *Icarus* 77.1, pp. 148–170.

Elliot, J. L. et al. (2003). “The recent expansion of Pluto’s atmosphere”. In: *Nature* 424.6945, pp. 165–168.

Erwin, Justin, O. J. Tucker, and Robert E. Johnson (2013). “Hybrid fluid/kinetic modeling of Pluto’s escaping atmosphere”. In: *Icarus* 226.1, pp. 375–384.

ESA. *Comet Interaction with Solar Wind*. http://m.esa.int/spaceinimages/Images/2002/12/Structure_of_a_comet.

ESA. *Voyager Plasma Spectrometer*. http://m.esa.int/spaceinimages/Images/2002/12/Structure_of_a_comet.

Europa Study Team (2012). “Europa Study 2012 Report”. In: *National Aeronautics and Space Administration*.

Famá, M., J. Shi, and R. A. Baragiola (2008). “Sputtering of ice by low-energy ions”. In: *Surface Science* 602.1, pp. 156–161.

Frank, L. A., K. L. Ackerson, J. A. Lee, M. R. English, and G. L. Pickett (1992). “The plasma instrumentation for the Galileo mission”. In: *Space Science Reviews* 60.1, pp. 283–304.

Gladstone, G. R. et al. (2016). “The atmosphere of Pluto as observed by New Horizons”. In: *Science* 351.6279. Ed. by F. Bagenal et al. eprint: http://science.sciencemag.org/content/351/6279/aad8866.full.pdf.

Grundy, W. M. et al. (2016). “Surface compositions across Pluto and Charon”. In: *Science* 351.6279, aad9189.

Guo, Yanping and Robert W. Farquhar (2008). “New Horizons mission design”. In: *Space science reviews* 140.1, pp. 49–74.

Gurnett, D. A., W. S. Kurth, R. R. Shaw, A. Roux, R. Gendrin, C. F. Kennel, F. L. Scarf, and S. D. Shawhan (1992). “The Galileo plasma wave investigation”. In: *The Galileo Mission*. Springer, pp. 341–355.

Haberman, William L and James EA John (1980). *Engineering thermodynamics*. Allyn and Bacon.

Hall, D. T., P. D. Feldman, M. A. McGrath, and D. F. Strobel (1998). “The far-ultraviolet oxygen airglow of Europa and Ganymede”. In: *The Astrophysical Journal* 499.1, p. 475.

Hall, D. T., D. F. Strobel, P. D. Feldman, M. A. McGrath, and H. A. Weaver (1995). “Detection of an oxygen atmosphere on Jupiter’s moon Europa”. In: *Nature* 373.6516, p. 677.

Hand, Kevin P. and Christopher F. Chyba (2007). “Empirical constraints on the salinity of the europan ocean and implications for a thin ice shell”. In: *Icarus* 189.2, pp. 424–438.

Hansen, Candice J., Donald E. Shemansky, and A. R. Hendrix (2005). “Cassini UVIS observations of Europa’s oxygen atmosphere and torus”. In: *Icarus* 176.2, pp. 305–315.

Harnett, E. M., R. M. Winglee, and P. A. Delamere (2005). “Three-dimensional multi-fluid simulations of Pluto’s magnetosphere: A comparison to 3D hybrid simulations”. In: *Geophysical research letters* 32.19, pp. L19104–1.

Hendrix, Amanda R., Timothy A. Cassidy, Robert E. Johnson, Chris Paranicas, and Robert W. Carlson (2011). “Europa’s disk-resolved ultraviolet spectra: Relationships with plasma flux and surface terrains”. In: *Icarus* 212.2, pp. 736–743.

Hoey, William A., Seng Keat Yeoh, Laurence M. Trafton, David B. Goldstein, and Philip L. Varghese (2017). “Rarefied gas dynamic simulation of transfer and escape in the Pluto–Charon system”. In: *Icarus* 287, pp. 87–102.

Horner, Matthew, Alexander Eremenko, and Matthew Gentile (2017). “Europa mission configuration update to accommodate maturing instrument designs”. In: *Aerospace Conference, 2017 IEEE*. IEEE, pp. 1–14.

Huebner, Walter F., John Joseph Keady, and S. P. Lyon (1992). "Solar photo rates for planetary atmospheres and atmospheric pollutants". In: *Solar Photo Rates for Planetary Atmospheres and Atmospheric Pollutants*. Springer, pp. 1–289.

Ip, W.-H. (1996). "Europa's oxygen exosphere and its magnetospheric interaction". In: *Icarus* 120.2, pp. 317–325.

Itikawa, Y. (2009). "Cross sections for electron collisions with oxygen molecules". In: *Journal of Physical and Chemical Reference Data* 38.1, pp. 1–20.

Itikawa, Y. and A. Ichimura (1990). "Cross sections for collisions of electrons and photons with atomic oxygen". In: *Journal of Physical and Chemical Reference Data* 19.3, pp. 637–651.

Jia, Y.-D., M. N. Villarreal, and C. T. Russell (2017). "Possible Ceres bow shock surfaces based on fluid models". In: *Journal of Geophysical Research: Space Physics*.

Johnson, R. E., M. H. Burger, T. A. Cassidy, F. Leblanc, M. Marconi, and W. H. Smyth (2009). "Composition and detection of Europa's sputter-induced atmosphere". In: *Europa, University of Arizona Press, Tucson*, pp. 507–527.

Johnson, R. E., R. M. Killen, J. H. Waite, and W. S. Lewis (1998). "Europa's surface composition and sputter-produced ionosphere". In: *Geophysical research letters* 25.17, pp. 3257–3260.

JPL. *Galileo Heavy Ion Counter*. http://www.srl.caltech.edu/galileo/galHIC.html.

Kabin, K., M. R. Combi, T. I. Gombosi, A. F. Nagy, D. L. DeZeeuw, and K. G. Powell (1999). "On Europa's magnetospheric interaction: A MHD simulation of the E4 flyby". In: *Journal of Geophysical Research: Space Physics* 104.A9, pp. 19983–19992.

Kameta, Kosei, Noriyuki Kouchi, Masatoshi Ukai, and Yoshihiko Hatano (2002). "Photoabsorption, photoionization, and neutral-dissociation cross sections of simple hydrocarbons in the vacuum ultraviolet range". In: *Journal of Electron Spectroscopy and Related Phenomena* 123.2, pp. 225–238.

Keane, James T., Isamu Matsuyama, Shunichi Kamata, and Jordan K. Steckloff (2016). "Reorientation and faulting of Pluto due to volatile loading within Sputnik Planitia". In: *Nature* 540.7631, pp. 90–93.

Kellett, S., Chris S. Arridge, E. J. Bunce, Andrew J. Coates, S. W. H. Cowley, M. K. Dougherty, A. M. Persoon, N. Sergis, and R. J. Wilson (2010). "Nature of the ring current in Saturn's dayside magnetosphere". In: *Journal of Geophysical Research: Space Physics* 115.A8.

Khurana, M. G. Kivelson, Kevin P. Hand, and Christopher T. Russell (2009). "Electromagnetic induction from Europa's ocean and the deep interior". In: *Robert. T. Pappalardo, William. B. McKinnon, and K. Khurana, Editors. Europa, University of Arizona Press, Tucson*, pp. 572–586.

Khurana, M. G. Kivelson, D. J. Stevenson, G. Schubert, et al. (1998). "Induced magnetic fields as evidence for subsurface oceans in Europa and Callisto". In: *Nature* 395.6704, p. 777.

Kivelson, M. G., K. K. Khurana, S. Joy, C. T. Russell, D. J. Southwood, R. J. Walker, and C. Polanskey (1997). "Europa's magnetic signature: Report from Galileo's pass on 19 December 1996". In: *Science* 276.5316, pp. 1239–1241.

Kivelson, M. G., K. K. Khurana, J. D. Means, C. T. Russell, and R. C. Snare (1992). "The Galileo magnetic field investigation". In: *Space Science Reviews* 60.1-4, pp. 357–383.

Kivelson, M. G., K. K. Khurana, D. J. Stevenson, L. Bennett, S. Joy, C. T. Russell, R. J. Walker, C. Zimmer, and C. Polanskey (1999). "Europa and Callisto: Induced or intrinsic fields in a periodically varying plasma environment". In: *Journal of Geophysical Research: Space Physics* 104.A3, pp. 4609–4625.

Kivelson, M. G., Krishan K. Khurana, Christopher T. Russell, Martin Volwerk, Raymond J. Walker, and Christophe Zimmer (2000). "Galileo magnetometer measurements: A stronger case for a subsurface ocean at Europa". In: *Science* 289.5483, pp. 1340–1343.

Kivelson, M. G., Krishan K. Khurana, and Martin Volwerk (2009). "Europa's interaction with the Jovian magnetosphere". In: *Europa, The Univ. of Arizona Space Sci. Ser*, p. 545.

Kliore, Arvydas J., David P. Hinson, F. Michael Flasar, Andrew F. Nagy, and Thomas E. Cravens (1997). "The ionosphere of Europa from Galileo radio occultations". In: *Science* 277.5324, pp. 355–358.

Koopman, David W. (1968). "Charge Exchange in CH4 and NH3". In: *The Journal of Chemical Physics* 49.11, pp. 5203–5205.

Koskinen, T. T., J. T. Erwin, and R. V. Yelle (2015). "On the escape of CH4 from Pluto's atmosphere". In: *Geophysical Research Letters* 42.17, pp. 7200–7205.

Krasnopolsky, V.A. and D.P. Cruikshank (1999). "Photochemistry of Pluto's atmosphere and ionosphere near perihelion". In: *J. Geophys. Res.* 104.E9, pp. 21979–21996.

Krupp, Norbert, A. Lagg, S. Livi, B. Wilken, J. Woch, E. C. Roelof, and D. J. Williams (2001). "Global flows of energetic ions in Jupiter's equatorial plane: First-order approx-

imation". In: *Journal of Geophysical Research: Space Physics* 106.A11, pp. 26017–26032.

Küppers, Michael et al. (2014). "Localized sources of water vapour on the dwarf planet (1) Ceres". In: *Nature* 505.7484, p. 525.

Lane, Arthur L., Robert M. Nelson, and Dennis L. Matson (1981). "Evidence for sulphur implantation in Europa's UV absorption band". In: *Nature* 292.5818, pp. 38–39.

LASP. *Galileo Plasma Subsystem*. http://www-pi.physics.uiowa.edu/pls/pls_description/pls_toc.htmlx.

UC-LASP. *Voyager Low-Energy Charged Particles Investigation*. http://lasp.colorado.edu/home/mop/missions/voyager/plasma-science/.

Lellouch, E., B. Sicardy, C. de Bergh, H.-U. Käufl, S. Kassi, and A. Campargue (2009). "Pluto's lower atmosphere structure and methane abundance from high-resolution spectroscopy and stellar occultations". In: *Astronomy and Astrophysics* 495.3, pp. L17–L21.

Lindsay, B. G. and R. F. Stebbings (2005). "Charge transfer cross sections for energetic neutral atom data analysis". In: *Journal of Geophysical Research: Space Physics* 110.A12.

Lipatov, A. S., J. F. Cooper, W. R. Paterson, E. C. Sittler Jr, R. E. Hartle, and David G. Simpson (2013). "Jovian plasma torus interaction with Europa. Plasma wake structure and effect of inductive magnetic field: 3D hybrid kinetic simulation". In: *Planetary and Space Science* 77, pp. 12–24.

Lipatov, A. S., J. F. Cooper, W. R. Paterson, E. C. Sittler, R. E. Hartle, and D. G. Simpson (2010). "Jovian plasma torus interaction with Europa: 3D hybrid kinetic simulation. First results". In: *Planetary and Space Science* 58.13, pp. 1681–1691.

Liu, Yifan, Andrew F. Nagy, Konstantin Kabin, Michael R. Combi, Darren L. DeZeeuw, Tamas I. Gombosi, and Kenneth G. Powell (2000). "Two-species, 3D, MHD simulation of Europa's interaction with Jupiter's magnetosphere". In: *Geophysical research letters* 27.12, pp. 1791–1794.

Luna, H., C. McGrath, M. B. Shah, R. E. Johnson, M. Liu, C. J. Latimer, and E. C. Montenegro (2005). "Dissociative charge exchange and ionization of O2 by fast H+ and O+ ions: Energetic ion interactions in Europa's oxygen atmosphere and neutral torus". In: *The Astrophysical Journal* 628.2, p. 1086.

McComas, D. J. et al. (2009). "The Solar Wind Around Pluto (SWAP) Instrument Aboard New Horizons". In: *New Horizons*. Springer Science Business Media, pp. 261–313.

McComas, D. J. et al. (2016). “Pluto’s interaction with the solar wind”. In: *Journal of Geophysical Research: Space Physics* 121.5. 2016JA022599, pp. 4232–4246.

McGrath, Melissa A., Emmanuel Lellouch, Darrell F. Strobel, Paul D. Feldman, and Robert E. Johnson (2004). “Satellite atmospheres”. In: *Jupiter: The Planet, Satellites and Magnetosphere*, pp. 457–483.

McNutt, R. L. et al. (2008). “The Pluto energetic particle spectrometer science investigation (PEPSSI) on the New Horizons mission”. In: *Space Science Reviews* 140.1-4, pp. 315–385.

Miller, David C. (1978). “THE VOYAGER MAGNETOMETER BOC”. In: *12th Aerospace Mechanisms Symposium NASA, Cal-Tech, Lockheed*. Vol. 100, p. 51.

Moore, Jeffrey M. et al. (2016). “The geology of Pluto and Charon through the eyes of New Horizons”. In: *Science* 351.6279. Ed. by F. Bagenal et al., pp. 1284–1293. eprint: http://science.sciencemag.org/content/351/6279/1284.full.pdf.

NASA. *Earth Magnetosphere*. https://www.nasa.gov/sites/default/files/images/517890main_Earth-Magnetosphere.jpg.

NASA. *Galileo Energetic Particles Detector*. https://nssdc.gsfc.nasa.gov/nmc/experimentDisplay.do?id=1989-084B-06.

NASA. *Galileo Magnetometer*. http://web.archive.org/web/20070213211452/http://www2.jpl.nasa.gov:80/galileo/instruments/mag1.jpg.

Ness, Norman F., Mario H. Acuña, Leonard F. Burlaga, John E. P. Connerney, Ronald P. Lepping, and Fritz M. Neubauer (1989). “Magnetic fields at Neptune”. In: *Science*, pp. 1473–1478.

Neubauer, Fritz M. (1998). “The sub-Alfvénic interaction of the Galilean satellites with the Jovian magnetosphere”. In: *Journal of Geophysical Research: Planets* 103.E9, pp. 19843–19866.

Neubauer, Fritz M. (1999). “Alfvén wings and electromagnetic induction in the interiors: Europa and Callisto”. In: *Journal of Geophysical Research: Space Physics* 104.A12, pp. 28671–28684.

Nimmo, F. et al. (2017). “Mean radius and shape of Pluto and Charon from New Horizons images”. In: *Icarus* 287, pp. 12–29.

Nishino, Masaki N. et al. (2011). “Anomalous deformation of the Earth’s bow shock in the lunar wake: Joint measurement by Chang’E-1 and SELENE”. In: *Planetary and Space Science* 59.5, pp. 378–386.

Noll, Keith S., H. A. Weaver, and A M. Gonnella (1995). "The albedo spectrum of Europa from 2200 Å to 3300 Å". In: *Journal of Geophysical Research: Planets* 100.E9, pp. 19057–19059.

Olkin, C. B. et al. (2015). "Evidence that Pluto's atmosphere does not collapse from occultations including the 2013 May 04 event". In: *Icarus* 246, pp. 220–225.

Paranicas, C., R. W. Carlson, and R. E. Johnson (2001). "Electron bombardment of Europa". In: *Geophysical research letters* 28.4, pp. 673–676.

Paranicas, C., A. F. Cheng, and D. J. Williams (1998). "Inference of Europa's conductance from the Galileo energetic particles detector". In: *Journal of Geophysical Research: Space Physics* 103.A7, pp. 15001–15007.

Paranicas, C., J. F. Cooper, H. B. Garrett, R. E. Johnson, and S. J. Sturner (2009). "Europa's radiation environment and its effects on the surface". In: *Europa. University of Arizona Press, Tucson* 529.

Paranicas, C., J. M. Ratliff, B. H. Mauk, C. Cohen, and R. E. Johnson (2002). "The ion environment near Europa and its role in surface energetics". In: *Geophysical Research Letters* 29.5.

Paterson, W. R., L. A. Frank, and K. L. Ackerson (1999). "Galileo plasma observations at Europa: Ion energy spectra and moments". In: *Journal of Geophysical Research: Space Physics* 104.A10, pp. 22779–22791.

Paty, C., W. Paterson, and R. Winglee (2008). "Ion energization in Ganymede's magnetosphere: Using multifluid simulations to interpret ion energy spectrograms". In: *Journal of Geophysical Research: Space Physics* 113.A6.

Paty, C. and R. Winglee (2004). "Multi-fluid simulations of Ganymede's magnetosphere". In: *Geophysical research letters* 31.24.

Paty, C. and R. Winglee (2006). "The role of ion cyclotron motion at Ganymede: Magnetic field morphology and magnetospheric dynamics". In: *Geophys. Res. Lett.* 33.10, n/a–n/a.

Plainaki, C., A. Milillo, A. Mura, S. Orsini, and T. Cassidy (2010). "Neutral particle release from Europa's surface". In: *Icarus* 210.1, pp. 385–395.

Plainaki, C., A. Milillo, A. Mura, S. Orsini, S. Massetti, and T. Cassidy (2012). "The role of sputtering and radiolysis in the generation of Europa exosphere". In: *Icarus* 218.2, pp. 956–966.

Pontius, Duane H. (2002). “The Io current wing”. In: *Journal of Geophysical Research: Space Physics* 107.A8.

Rajendar, Ashok (2015). “Multifluid Magnetohydrodynamic Investigation of the Global Dynamics of Saturn’s Magnetosphere”. PhD thesis. Georgia Institute of Technology.

Raymond, C. A., X. Jia, S. P. Joy, K. K. Khurana, N. Murphy, C. T. Russell, R. J. Strangeway, and B. P. Weiss (2015). “Interior Characterization of Europa using Magnetometry (ICEMAG): Probing the Europan Ocean and Exosphere”. In: *AGU Fall Meeting Abstracts*.

Richards, Philip G., Thomas N. Woods, and William K. Peterson (2006). “HEUVAC: A new high resolution solar EUV proxy model”. In: *Advances in space research* 37.2, pp. 315–322.

Richardson, J. D. and C. W. Smith (2003). “The radial temperature profile of the solar wind”. In: *Geophys. Res. Lett.* 30.5, n/a–n/a.

Roth, L., Kurt D. Retherford, Nickolay Ivchenko, Nicola Schlatter, Darrell F. Strobel, Tracy M. Becker, and Cesare Grava (2017). “Detection of a hydrogen corona in HST Lyα images of Europa in transit of Jupiter”. In: *The Astronomical Journal* 153.2, p. 67.

Roth, L., J. Saur, K. D. Retherford, D. F. Strobel, P. D. Feldman, M. A. McGrath, and F. Nimmo (2014). “Transient water vapor at Europa’s south pole”. In: *Science* 343.6167, pp. 171–174.

Roth, L., J. Saur, K. D. Retherford, D. F. Strobel, P. D. Feldman, M. A. McGrath, J. R. Spencer, A. Blöcker, and N. Ivchenko (2016). “Europa’s far ultraviolet oxygen aurora from a comprehensive set of HST observations”. In: *Journal of Geophysical Research: Space Physics* 121.3, pp. 2143–2170.

Rubin, M. et al. (2014). “Plasma environment of a weak comet–Predictions for Comet 67P/Churyumov–Gerasimenko from multifluid-MHD and Hybrid models”. In: *Icarus* 242, pp. 38–49.

Rubin, M. et al. (2015). “Self-consistent multifluid MHD simulations of Europa’s exospheric interaction with Jupiter’s magnetosphere”. In: *Journal of Geophysical Research: Space Physics* 120.5, pp. 3503–3524.

Rymer, A. M. et al. (2009). “Cassini evidence for rapid interchange transport at Saturn”. In: *Planetary and Space Science* 57.14, pp. 1779–1784.

Samson, James A. R., G. N. Haddad, T. Masuoka, P. N. Pareek, and D. A. L. Kilcoyne (1989). “Ionization yields, total absorption, and dissociative photoionization cross sec-

tions of CH4 from 110 to 950 Å". In: *The Journal of Chemical Physics* 90.12, pp. 6925–6932.

Sauer, K., A. Lipatov, K. Baumgärtel, and E. Dubinin (1997). "Solar wind-Pluto interaction revised". In: *Advances in Space Research* 20.2, pp. 295–299.

Saur, J., D. F. Strobel, and F. M. Neubauer (1998). "Interaction of the Jovian magnetosphere with Europa: Constraints on the neutral atmosphere". In: *Journal of Geophysical Research: Planets* 103.E9, pp. 19947–19962.

Saur, J. et al. (2011). "Hubble space telescope/advanced camera for surveys observations of Europa's atmospheric ultraviolet emission at eastern elongation". In: *The Astrophysical Journal* 738.2, p. 153.

Scarf, Frederick L. and Donald A. Gurnett (1977). "A plasma wave investigation for the Voyager mission". In: *Space Science Reviews* 21.3, pp. 289–308.

Schilling, N., F. M. Neubauer, and J. Saur (2008). "Influence of the internally induced magnetic field on the plasma interaction of Europa". In: *Journal of Geophysical Research: Space Physics* 113.A3.

Schilling, N., Fritz M. Neubauer, and Joachim Saur (2007). "Time-varying interaction of Europa with the jovian magnetosphere: Constraints on the conductivity of Europa's subsurface ocean". In: *Icarus* 192.1, pp. 41–55.

Schmidt, B. E., D. D. Blankenship, G. W. Patterson, and P. M. Schenk (2011). "Active formation of 'chaos terrain' over shallow subsurface water on Europa". In: *Nature* 479.7374, p. 502.

Schreier, Ron, Aharon Eviatar, Vytenis M. Vasyliūnas, and John D. Richardson (1993). "Modeling the Europa plasma torus". In: *Journal of Geophysical Research: Space Physics* 98.A12, pp. 21231–21243.

Shematovich, V. I., R. E. Johnson, J. F. Cooper, and M. C. Wong (2005). "Surface-bounded atmosphere of Europa". In: *Icarus* 173.2, pp. 480–498.

Shi, M., R. A. Baragiola, D. E. Grosjean, R. E. Johnson, S. Jurac, and Jørgen Schou (1995). "Sputtering of water ice surfaces and the production of extended neutral atmospheres". In: *Journal of Geophysical Research: Planets* 100.E12, pp. 26387–26395.

Sicardy, B. et al. (2003). "Large changes in Pluto's atmosphere as revealed by recent stellar occultations". In: *Nature* 424.6945, pp. 168–171.

Smyth, William H. and Max L. Marconi (2006). "Europa's atmosphere, gas tori, and magnetospheric implications". In: *Icarus* 181.2, pp. 510–526.

Snowden, D., R. Winglee, and A. Kidder (2011). “Titan at the edge: 1. Titan’s interaction with Saturn’s magnetosphere in the prenoon sector”. In: *J. Geophys. Res.* 116.A8.

Song, Mi-Young, Jung-Sik Yoon, Hyuck Cho, Yukikazu Itikawa, Grzegorz P Karwasz, Viatcheslav Kokoouline, Yoshiharu Nakamura, and Jonathan Tennyson (2015). “Cross sections for electron collisions with methane”. In: *Journal of Physical and Chemical Reference Data* 44.2, p. 023101.

Sparks, W. B., K. P. Hand, M. A. McGrath, E. Bergeron, M. Cracraft, and S. E. Deustua (2016). “Probing for evidence of plumes on Europa with HST/STIS”. In: *The Astrophysical Journal* 829.2, p. 121.

Sparks, W. B., B. E. Schmidt, M. A. McGrath, K. P. Hand, J. R. Spencer, M. Cracraft, and S. E. Deustua (2017). “Active Cryovolcanism on Europa?” In: *The Astrophysical Journal Letters* 839.2, p. L18.

Spencer, J. R., L. K. Tamppari, T. Z. Martin, and Larry D. Travis (1999). “Temperatures on Europa from Galileo photopolarimeter-radiometer: nighttime thermal anomalies”. In: *Science* 284.5419, pp. 1514–1516.

Spencer, John (1999). “The Jovian Magnetosphere”. In: *Beatty, J. K. and Petersen, C. C. and Chaikin, A. and Authors. The New Solar System*.

Stern, S. A., R. Gladstone, A. Zangari, T. Fleming, and D. Goldstein (2015a). “Transient atmospheres on Charon and water-ice covered KBOs resulting from comet impacts”. In: *Icarus* 246, pp. 298–302.

Stern, S. A. et al. (2015b). “The Pluto system: Initial results from its exploration by New Horizons”. In: *Science* 350.6258.

Stern, S. A. et al. (2017a). “New Horizons constraints on Charon’s present day atmosphere”. In: *Icarus* 287, pp. 124–130.

Stern, S. A. et al. (2017b). “Past epochs of significantly higher pressure atmospheres on Pluto”. In: *Icarus* 287, pp. 47–53.

Strobel, Darrell F. and Xun Zhu (2017). “Comparative planetary nitrogen atmospheres: Density and thermal structures of Pluto and Triton”. In: *Icarus* 291, pp. 55–64.

Teolis, B. D., D. Y. Wyrick, A. Bouquet, B. A. Magee, and J. H. Waite (2017). “Plume and surface feature structure and compositional effects on Europa’s global exosphere: Preliminary Europa mission predictions”. In: *Icarus* 284, pp. 18–29.

Tholen, D. J., V. G. Tejfel, and A. N. Cox (2002). “Planets and satellites”. In: *Allen’s Astrophysical Quantities*. Springer, pp. 293–313.

Tilley, Matt, Erika Harnett, and Robert Winglee (2015). "Modeling the effects of plasma pressure anisotropy on Saturn's global magnetosphere". Magnetospheres of Outer Planets, Atlanta, GA.

Truscott, Pete, Daniel Heynderickx, Angélica Sicard-Piet, and Sébastien Bourdarie (2011). "Simulation of the radiation environment near Europa using the geant4-based PLAN ETOCOSMICS-J model". In: *IEEE Transactions on Nuclear Science* 58.6, pp. 2776–2784.

Tucker, O.J., R.E. Johnson, and L.A. Young (2015). "Gas transfer in the Pluto-Charon system: A Charon atmosphere". In: *Icarus* 246, pp. 291–297.

Tyler, G. L., I. R. Linscott, M. K. Bird, D. P. Hinson, D. F. Strobel, M. Pńtzold, M. E. Summers, and K. Sivaramakrishnan (2009). "The New Horizons radio science experiment (REX)". In: *New Horizons*. Springer, pp. 217–259.

Vernisse, Y., H Kriegel, S Wiehle, U Motschmann, and K-H Glassmeier (2013). "Stellar winds and planetary bodies simulations: Lunar type interaction in super-Alfvénic and sub-Alfvénic flows". In: *Planetary and Space Science* 84, pp. 37–47.

Volwerk, M., K. Khurana, and M. Kivelson (2007). "Europa's Alfvén wing: Shrinkage and displacement influenced by an induced magnetic field". In: *Annales Geophysicae*. Vol. 25. 4, pp. 905–914.

Volwerk, M., M. G. Kivelson, and K. K. Khurana (2001). "Wave activity in Europa's wake: Implications for ion pickup". In: *Journal of Geophysical Research: Space Physics* 106.A11, pp. 26033–26048.

Waite Jr, JH et al. (2015). "Maspex Europa". In: *AGU Fall Meeting Abstracts*.

Westlake, Joseph H et al. (2016). "The Plasma Instrument for Magnetic Sounding (PIMS) on The Europa Clipper Mission". In: *AAS/Division for Planetary Sciences Meeting Abstracts*. Vol. 48.

Williams, D. J., R. W. McEntire, S. Jaskulek, and B. Wilken (1992). "The Galileo energetic particles detector". In: *Space Science Reviews* 60.1, pp. 385–412.

Winglee, R. M. (1998). "Multi-fluid simulations of the magnetosphere: The identification of the geopause and its variation with IMF". In: *Geophysical research letters* 25.24, pp. 4441–4444.

Wolff, R. S. and D. A. Mendis (1983). "On the nature of the interaction of the Jovian magnetosphere with the icy Galilean satellites". In: *Journal of Geophysical Research: Space Physics* 88.A6, pp. 4749–4769.

Yoon, Peter H., Luiz F. Ziebell, Rudi Gaelzer, Linghua Wang, and Robert P. Lin (2013). "Solar Wind Electron Acceleration via Langmuir Turbulence." In: *Terrestrial, Atmospheric & Oceanic Sciences* 24.2.

Young, Leslie A., J. L. Elliot, Alan Tokunaga, Catherine de Bergh, and Tobias Owen (1997). "Detection of gaseous methane on Pluto". In: *Icarus* 127.1, pp. 258–262.

Zheng, Weijun, David Jewitt, and Ralf I. Kaiser (2009). "On the state of water ice on Saturn's moon Titan and implications to icy bodies in the outer solar system". In: *The Journal of Physical Chemistry A* 113.42, pp. 11174–11181.

Zhu, Xun, Darrell F. Strobel, and Justin T. Erwin (2014). "The density and thermal structure of Pluto's atmosphere and associated escape processes and rates". In: *Icarus* 228, pp. 301–314.

Zimmer, C., K. K. Khurana, and M. G. Kivelson (2000). "Subsurface oceans on Europa and Callisto: Constraints from Galileo magnetometer observations". In: *Icarus* 147.2, pp. 329–347.

Zirnstein, E. J. et al. (2016). "Interplanetary Magnetic Field Sector from Solar Wind around Pluto (SWAP) Measurements of Heavy Ion Pickup near Pluto". In: *The Astrophysical Journal Letters* 823.2, p. L30.

VITA

John Marshall Hale,

Through many a travail,

Completed his doctoral degree,

And went to study space in Washington, DC.